RELAXATION, RATTLING AND DECOUPLING

Dynamic Processes in Glassy Matter

Dissertation zur Erlangung des Doktorgrades
(Dr. rer. nat.)
der Mathematisch-Naturwissenschaftlichen Fakultät
der Universität Augsburg

vorgelegt von
Melanie Köhler

Institut für Physik
Elektronische Korrelationen und Magnetismus
Lehrstuhl für Experimentalphysik V

Augsburg, Mai 2010

1. Gutachter: Prof. Dr. A. Loidl
2. Gutachter: Prof. Dr. A. Reller

Tag der Einreichung: 21. Mai 2010
Tag der mündlichen Prüfung: 15. Juli 2010

Wer so tut, als bringe er die Menschen zum Nachdenken, den lieben sie.
Wer sie wirklich zum Nachdenken bringt, den hassen sie.

Aldous Huxley

List of abbreviations:

BP	boson peak
BWO	backward wave oscillator
BZP	benzophenone
CC	Cole-Cole
CD	Cole-Davidson
CM	coupling model
(D)LS	(dynamic) light scattering
DOS	density of states
DPG	dipropylene glycol
EW	excess wing
FIR	far infrared
FTIR	Fourier transform infrared
HN	Havriliak-Negami
JG	Johari-Goldstein
KWW	Kohlrausch-Williams-Watts
MCT	mode coupling theory
MM	minimal model
NCL	nearly constant loss
NRKM	nonmonotonic relaxation kinetic model
NS	neutron scattering
OCA	ortho-carborane
OKE	optical Kerr effect
o-Ps	ortho-positronium
PG	propylene glycol
PPG	polypropylene glycol
TPG	tripropylene glycol
UDR	universal dielectric response
VFT	Vogel-Fulcher-Tamman

1 Introduction

Mankind has enjoyed a very special relationship to glass from the very beginning. Our ancestors figured out, how to manipulate natural glasses like obsidian, how to manufacture arrow tips and knives. The earliest man-made glass objects, Egyptian beads, are thought to date back to around 3000 BC. A major breakthrough was the discovery of glass blowing around the end of the 1st century BC along the Eastern Mediterranean coast. In the same century, the Romans conquest Egypt and the art of glass making is spread throughout the Roman Empire. After a quiet period in the dark ages, Venetian glass making becomes famous around the 10th century AD. In the 17th century, this amazing material was for the first time used scientifically for microscopes and telescopes and over the years substantial progress in the production techniques took place.

Nowadays glass is a material of paramount importance. It is ubiquitous in everyday life and used in classical fields like architecture, packaging or household. However, it is also known as functional material in more recent areas of application like optical fibres in communication techniques, lenses in high-resolution microscopes or as bioactive implants in medicine. And glass continues to benefit the quality of human life.[1–4]

Despite its importance, the physics of glasses is still poorly understood and the transition from the liquid into the glassy state is commonly considered as one of the great unsolved problems of solid state physics.[4–7] During recent years experimental advances and significant theoretical progress led to an increasing interest to gain a deeper understanding in these challenging problems.

In this context a more basic question arises: What is the exact definition of a glass? Or is there an adequate definition anyway? There are many attempts of giving a definition. The most extensive may be that a glass is considered as a solid without lattice symmetry or as a "frozen" liquid. This scenario is shown on the left part of figure 1.1. Sufficiently fast cooling prevents the phase transition to a crystal and leads to a subsequent slowing down of the translational and reorientational degrees of freedom. This state is called supercooled liquid. Further cooling leads to a glass, where all degrees of freedom are frozen. Aside of the structural glasses, sometimes a plastic crystal can emerge from the liquid state under certain cooling conditions. Here, shown on the right side of figure 1.1, the centres of mass of the molecules form a regular crystalline lattice, but the molecules are still dynamically disordered with respect to their orientational degrees of freedom.[8]

The scientific focus of modern physics of glasses is mainly put on the dynamic behaviour going from the liquid to the glassy state. During the past years various models and theories have been developed. Some of them, e.g., the Adam-Gibbs[9] and the Free-Volume-Theory[10] assume a low-temperature phase transition underlying the glass transition. In contrast, mode coupling theory, currently one of the most prominent and most controversially discussed theories of glass physics, explains the glass transition in terms of a dynamic phase transition.[1,11–14]

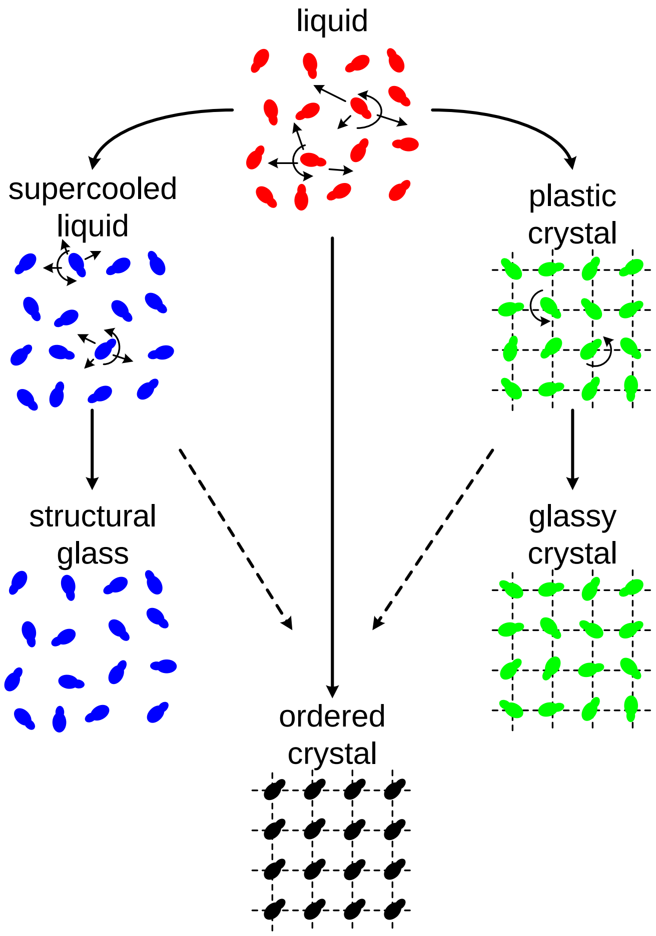

Figure 1.1: Schematic drawing[8] of the possible transitions of dipolar glass formers from the liquid state into a structural glass, an ordered crystal, or a glassy crystal.

Going from the liquid to the glassy state, the viscosity increases tremendously. Glassy matter exhibits at least three universal features, the so-called three non's.[15–17] The first *non* is the non-exponential time dependence of the relaxation processes. The second *non* refers to the non-Arrhenius behaviour of the α-relaxation times and the third *non* is related to the aging behaviour of glassy matter when it is out of its equilibrium state.

Dielectric spectroscopy has proven to be a very powerful tool for the investigation of the dynamic behaviour of glassy matter. With its broad frequency range the main dynamical processes, only to mention the structural α-relaxation, the slow and the fast β-relaxation or the microscopic peak, are accessible. Prerequisite for the investigation with this method is the presence of dipolar or electrically charged particles. The electrical field directly couples to the orientational and translational degrees of freedom, respectively.

In the main focus of the present work are two different systematic studies. The first one is about a series of propylene glycols, the second one about the binary mixture glycerol - LiCl.

The investigation of the propylene glycols concentrates on the high frequency response up to THz frequencies and the effects caused by the variation of the molecular size. In addition, results from dielectric spectroscopy, positron annihilation lifetime spectroscopy and neutron scattering experiments are compared and discussed in detail.

The binary system glycerol - LiCl is characterized by dielectric spectroscopy over a very broad frequency range. Adding ions strongly influences the structural α-relaxation, which shows an extreme slowing down with increasing ion content. This behaviour should lead to a more pronounced secondary process and additionally influences the high-frequency response in the minimum region. In contrast to dielectric spectroscopy, where translational motions of the ions and reorientational motions of the dipoles play an important role, neutron scattering exclusively couples to density fluctuations. Differences between both methods, especially when tuning from orientational- to translational response by adding ions, are discussed phenomenologically and in the framework of mode coupling theory.

2 Phenomenological and theoretical predictions

2.1 Principles of dielectric spectroscopy

Dielectric spectroscopy is able to detect dynamic processes that involve the reorientation of dipoles or the displacement of charged particles. If an electric field is applied to such entities, relaxation or hopping processes occur. With electrically active processes, often structural rearrangement processes are connected, e.g., the reorientation of a dipolar molecule can lead to a translational shift of its neighbours and vice versa. Along this route, the dielectric response yields information about a variety of dynamic processes in glassy matter.

Usually the results of dielectric measurements are presented as spectra of the real and imaginary part of the complex dielectric permittivity $\varepsilon^* = \varepsilon' - i\varepsilon''$. It is defined via the dielectric displacement $D^*(\nu) = \varepsilon^* \varepsilon_0 E^*(\nu)$, with ε^* the permittivity of vacuum and E^* the time-dependent electrical field.[I] The real part ε' denotes the dielectric constant, which is a misleading denotation as ε' is frequency dependent. The imaginary part ε'' is proportional to the part of D' that is out of phase with the E-field with a phase difference of $\pi/2$. ε'' is called the dielectric loss as it is proportional to the "loss of energy" (energy dissipated to heat) from the applied E-field into the sample.[18] These quantities are connected via $P^* = \varepsilon_0 \chi^* E^*$ to the polarisation P, and via $\varepsilon^* = 1 + \chi^*$ to the dielectric susceptibility.

2.1.1 Relaxation in dielectric matter

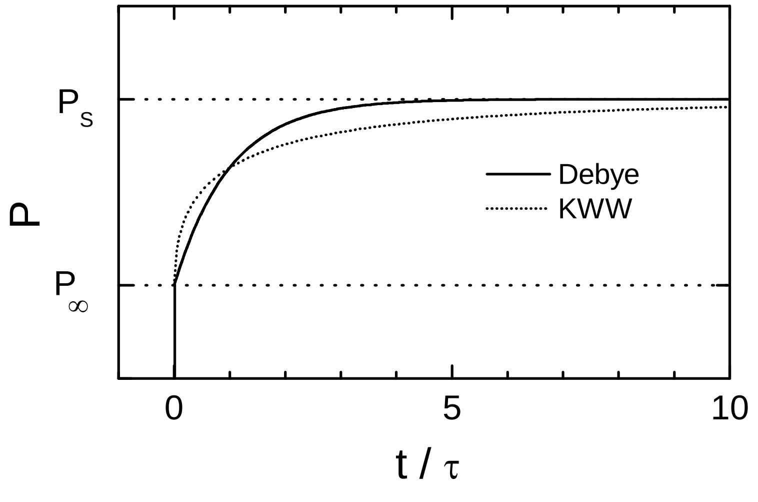

Figure 2.1: Time dependent relaxation of the polarization after application of an electric field at *t=0*. The theoretical exponential response of non-interacting dipoles with one common relaxation time (Debye relaxation) is shown by the solid line. The dashed line is a stretched exponential or KWW function (β_{KWW} = 0.5), often used to describe real systems.[3] For more details on the KWW function, see chapter 2.2.

[I] The star superscripts denote complex quantities

Now the reaction of non-interacting permanent dipoles with a common relaxation time τ to the application of an electric field E is considered. This causes an almost instantaneous polarisation P, as shown in figure 2.1. It is reasonable to assume that all dipoles will relax with a rate, proportional to the distance from their equilibrium orientation. For the polarisation the differential equation[19]

$$P_s - P(t) = \tau \cdot \frac{\partial P(t)}{\partial t} \tag{2.1}$$

with the solution

$$P(t) = P_s + (P_\infty - P_s) \cdot \exp\left(-\frac{t}{\tau}\right) \tag{2.2}$$

results. P_∞ denotes the contribution of ionic and electronic polarisation, which is achieved nearly instantaneously with applying the electrical field. P_s is the "static" polarisation, which may change if further slower processes are present. τ denotes the relaxation time, the exponential part describes the so-called Debye-relaxation. The application of a Fourier transform on equation (2.2) leads to the following expression for the dielectric permittivity, the frequency dependent Debye equation:[20]

$$\varepsilon^* = \varepsilon_\infty + \frac{\varepsilon_s - \varepsilon_\infty}{1 + i\omega\tau} \tag{2.3}$$

Here, ω denotes the angular frequency, ε_s the static dielectric constant and ε_∞ the high frequency limit of the dielectric constant. The difference $\Delta\varepsilon = \varepsilon_s - \varepsilon_\infty$ is defined as dielectric strength. The behaviour of the frequency dependent dielectric permittivity of the Debye function is shown in a three-dimensional plot in figure 2.2. Projections on the lower and on the right plane display real and imaginary part, $\varepsilon'(\nu)$ and $\varepsilon''(\nu)$, while the projection on the left plane shows the so-called Cole-Cole plot. This kind of data representation is time-honoured and often used in older publications as it allows for a graphical analysis. The Debye relaxation then results in a semi-circle with radius $r = \Delta\varepsilon/2$. The real part ε' shows a step of height $\Delta\varepsilon$ at the normalized frequency $2\pi\nu\tau = 1$. The imaginary part appears as a bell-shaped curve at $2\pi\nu\tau = 1$ with a half width of W_D = 1.14 decades and a height of $\Delta\varepsilon/2$.

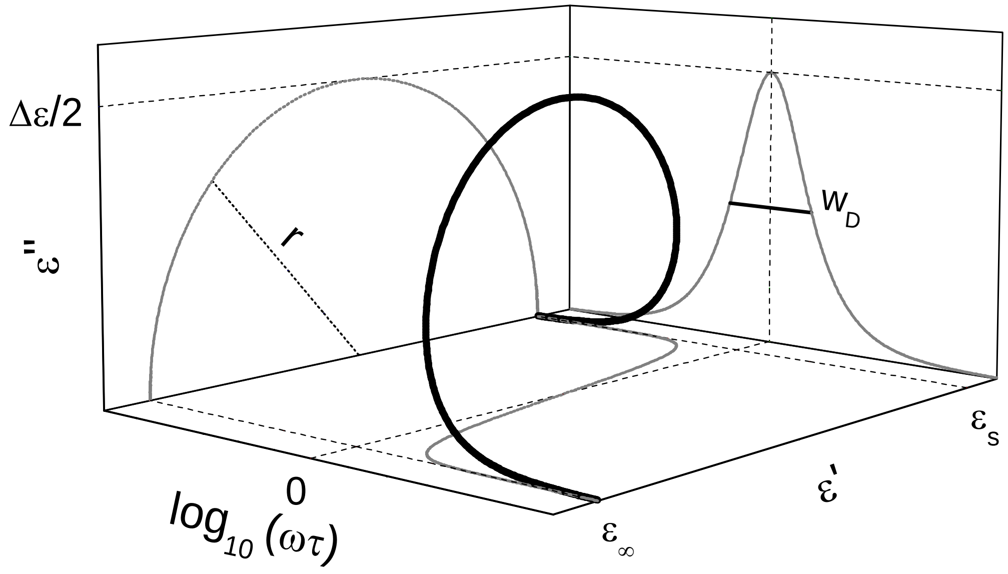

Figure 2.2: Three-dimensional representation of the complex permittivity of a Debye relaxation, according to Ref. 21. Parameters are explained in the text.

2.2 Dielectric response of glass-forming liquids

Figure 2.3 illustrates the typical broadband dielectric loss of non-conducting glass-forming materials.[3,22] In the low frequency range, the structural α-relaxation peak (yellow) shows up. At frequencies beyond this primary process a second peak or shoulder, due to the slow β-relaxation, is observed in many glass-forming materials (Type B glass-formers).[23] Instead of this peak, a second power law at the high-frequency flank of the α-peak shows up (Type A glass-formers).[23] This feature is the so-called excess wing (EW). The microscopic origin of both processes still is highly debated.[4,24–31] The excess wing is assumed to be the high frequency flank of the slow β-process, which sometimes is hidden under the dominating α-process.[32–34] In the GHz-THz range, additional fast processes contribute and give rise to excess intensity in the minimum region. At some THz a further loss-peak, the so-called boson peak (BP) is observed. At frequencies beyond THz, infrared bands show up which are decoupled from glass formation. In the following section, all processes are discussed in more detail.[3,35]

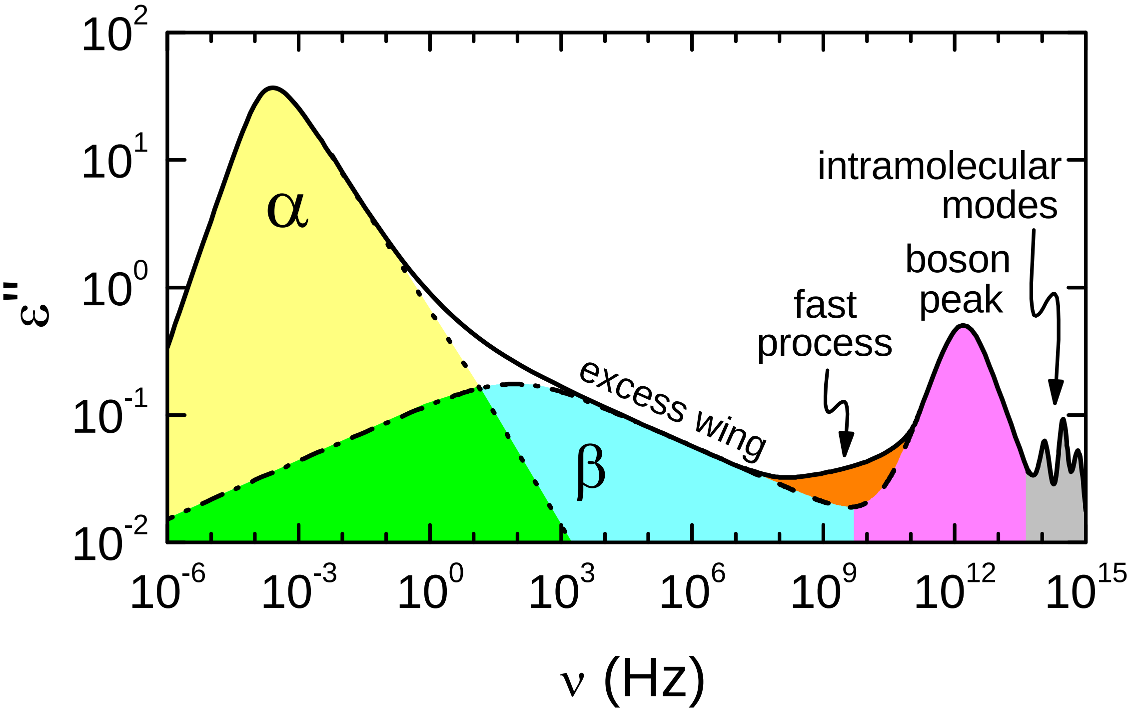

Figure 2.3: Schematic illustration[17] of the frequency-dependent dielectric loss $\varepsilon''(\nu)$ in glass-forming materials.[3,35] Various characteristic features are seen: The structural α-relaxation, the excess wing (Type A), the fast (β-) process, the boson peak and infrared bands (intramolecular modes) at the highest frequencies.

2.2.1 *The α-relaxation*

In the dielectric loss $\varepsilon''(\nu)$ the α-process shows up as a well-pronounced, asymmetrically shaped peak at a frequency ν_α with an average relaxation time $\langle\tau_\alpha\rangle = (2\pi\nu_\alpha)^{-1}$.[3,22] The dielectric constant $\varepsilon'(\nu)$ displays a step-like decrease (not shown) and the α-peak position corresponds to the inflexion point in $\varepsilon'(\nu)$. Assuming an exponential time dependence of the dipole-orientations and a single relaxation time for all molecules, in frequency domain Debye response (cf. equation (2.3)) is expected. This approach usually is not sufficient to describe the experimental results. In general, the loss peaks show a clear broadening. This is assumed to be due to a distribution of relaxation times $g(\tau)$. To take account of the observed experimental deviations, various modifications of equation (2.3) were proposed. The most general one is the phenomenological Havriliak-Negami (HN) equation:[36]

$$\varepsilon^* = \varepsilon_\infty + \frac{\varepsilon_s - \varepsilon_\infty}{[(1 + i\omega\tau)^{1-\alpha}]^\beta} \tag{2.4}$$

Broadening and asymmetry are determined by the exponents α and β ($0 \leq \alpha < 1$; $0 < \beta \leq 1$). For $\alpha \neq 1$ and $\beta = 1$ the symmetrically broadened Cole-Cole[37] (CC) function with slopes 1 -

α_{CC} and α_{CC} - 1 for the low and high frequency flank results in a double logarithmic representation of $\varepsilon''(\nu)$. The asymmetrically shaped Cole-Davidson[38,39] (CD) function results for $\alpha = 0$ and $\beta \neq 1$. However, the Kohlrausch Williams Watts (KWW) function,[40,41] the Fourier transform of a stretched exponential function Φ is often used for data parameterization:

$$\Phi = \Phi_0 exp\left[-\left(\frac{t}{\tau_{KWW}}\right)\right]^{\beta_{KWW}} \tag{2.5}$$

Φ denotes an amplitude function, e.g., the polarization.[40,41] Frequently the KWW function is assumed to be identical or very similar to the CD function. A comparison of the dielectric loss calculated by Debye, CC, CD and KWW relation is shown in figure 2.4.

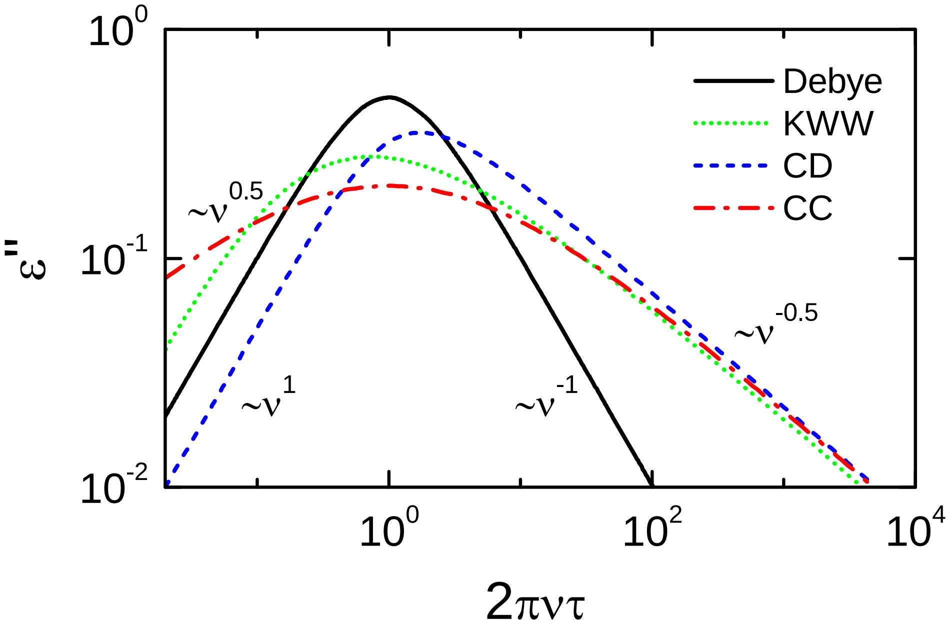

Figure 2.4: Dielectric loss calculated from the Debye, CC and CD expressions, according to Ref. 1. Parameters are chosen as $\beta_{CD} = 0.5$ and $\alpha_{CD} = 0.5$. In addition, the KWW function is shown ($\beta_{KWW} = 0.5$).

Using the same β-parameters for the CD and the KWW function, the latter shows deviations in the peak region. The peak position is shifted to lower frequencies while its shape, compared to the shape of the CD-peak, is broadened.

For the asymmetrically shaped CD function, the average relaxation time is assumed as $\langle\tau_{CD}\rangle = \tau_\alpha \beta_{CD}$. The average relaxation time $\langle\tau_{CC}\rangle$ of the CC function corresponds to the relaxation time of the peak position as the CC peak is symmetrically shaped. For the HN function, no average relaxation time can be determined.

2.2.2 Excess wing and slow β-process

At frequencies beyond the α-relaxation often a secondary process, the so-called slow β-relaxation, is observed. This process shows up as an additional peak or shoulder in $\varepsilon''(\nu)$. Depending on temperature, this feature is typically located in the kHz-MHz range.[23,24,28,42,43] By thorough investigations of rigid molecules, Johari and Goldstein[28] (JG) demonstrated that this process seems to be inherent to glass-forming materials, even if an intramolecular origin can be excluded. Instead of a secondary peak or shoulder due to a JG relaxation, in some glass-formers an excess wing shows up at the high-frequency flank of the α-process. It can usually be well described by a second, weaker power law decrease. Both processes have in common that they are rather universal. It seems that each glass forming material has at least either a β-relaxation or an excess wing. By performing dielectric aging experiments below T_g, strong hints have been found, that the β-process and the excess wing are due to the same microscopic phenomenon differing simply by a different temperature evolution.[44] This finding is also corroborated by various other experiments.[43,45–47] Thus the excess wing may be assumed as the high frequency flank of the slow β-peak which is hidden under the stronger α-relaxation. However, there are also other explanations of the excess wing and the slow β-relaxation, and it still remains unsolved, if the excess wing is of JG-type[44,48] or if it is a further, separate phenomenon.[49,23]

2.2.3 The fast β-process

Another typical feature of glassy matter is the fast β-relaxation, showing up as a shallow minimum in the GHz-THz range. Additional contributions, caused by a fast process, (shown as orange area in figure 2.3) give rise to intensity arising in excess to a simple superposition from the additive crossover from α- to boson peak. This region found much interest during recent years as the fast glassy dynamics may be the key to a better understanding of the glass transition and the glassy state of matter in general. By dielectric spectroscopy this high frequency region is only accessible under great effort and the measurements are extremely challenging and time consuming. For this reason, in the high frequency regime only sparse data is found in literature.[3,35,50–54] The fast β-relaxation is predicted by mode coupling theory (MCT) and ascribed to the "rattling" motion (cf. figure 2.12) of a particle in the transient cage formed by its neighbouring molecules.[14] But there are also other approaches to explain the excess intensity observed in this high-frequency region. A prominent one is the extended coupling model,[55] which involves an explanation in terms of a nearly constant loss, a phenomenon which has been known for long.[56–58]

2.2.4 The boson peak

The term boson peak (BP) originates from Raman experiments on disordered matter and characterizes the intensity arising in excess to the Debye vibrational density of states (DOS) at low frequencies, revealing a temperature dependence in accord with the Bose-Einstein statistics.[59] To account for the excess contribution over the Debye vibrational DOS, the DOS divided by the squared frequency $g(\omega)/\omega^2$, is taken into account.[60] A good approximation of this quantity is $\varepsilon''T/\omega$, which later is considered in the data analysis (cf. sections 4.2.5 and 4.3.3.2).

The boson peak is observed likewise in neutron and light scattering data as well as in dielectric measurements, where it dominates the dielectric loss spectra at THz frequencies. As an example, neutron- and light scattering data of glycerol[61] are shown in figure 2.5. The light scattering spectra $I_{VH}(\omega)$ in figure 2.5 (a) are dominated by a quasielastic signal increasing tremendously with increasing temperatures.

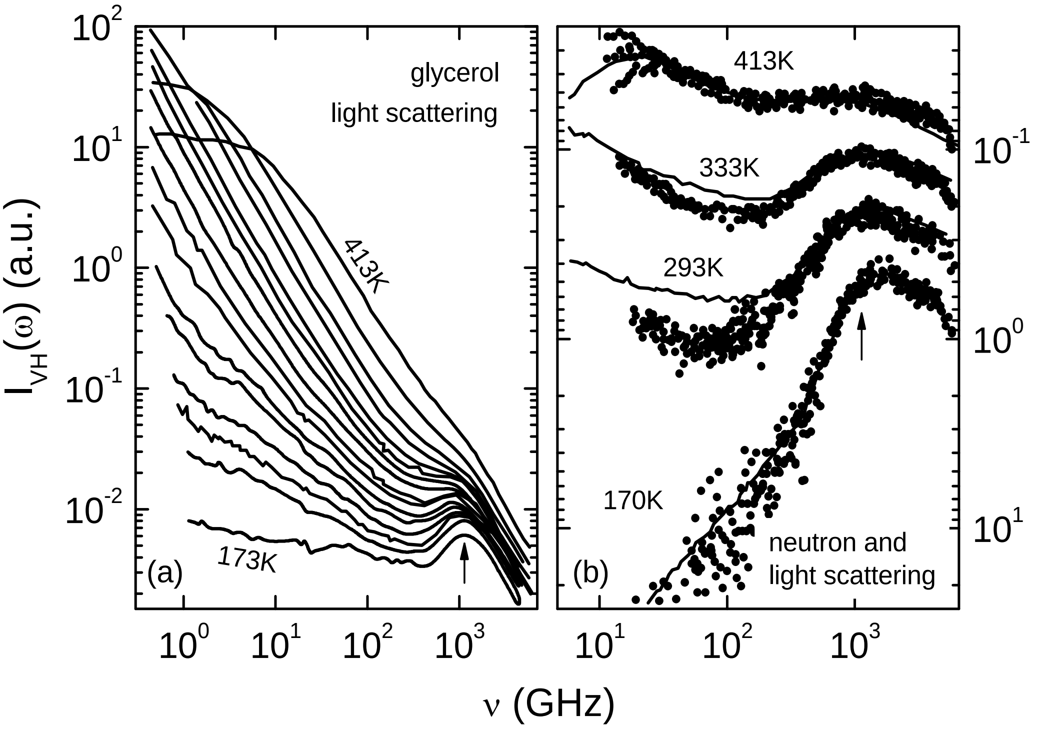

Figure 2.5: (a) Depolarized light scattering spectra $I_{VH}(\omega)$ for T= 413, 363, 333, 313 to 193 K in steps of 10 K, and 173 K. In the THz region the boson peak shows up at low temperatures. In (b) susceptibility spectra from light scattering (lines) compared to spectra from neutron (symbols) scattering, for q values from 0.8 - 3.2 Å^{-1}, are shown. Figures adopted from Ref. 61.

For the calculation of the susceptibility, the multiplication of the spectra with the frequency is necessary. Light scattering spectra of figure 2.5 (b) were calculated from the data shown in (a). For a better visualisation, the frequency corresponding to the peak position of the 170 K curve is indicated by an arrow in (b). The peak position of the boson peak shifts to higher frequencies when calculating $\chi''(\nu)$.

Lunkenheimer and Loidl[60,62] compared the shape of the boson peak of the canonical glass-former glycerol and the orientationally disordered ('plastic') crystal ortho-carborane. Within this comparison, they suggested to interpret the boson peak as lattice vibrations (phonons) which are smeared out in the canonical glass because of lacking long-range order. The broadened maximum represents the whole vibrational density of states. However, in the plastic crystalline phase the molecules are arranged on a regular crystalline lattice and, corresponding to the Debye model, the density of states drops above the so-called cut-off frequency. This leads to a strong asymmetry in the peak of ortho-carborane.

Several models try to explain the boson peak, just to mention the soft potential model,[63–65] phonon localization models,[66,67] an harmonic-oscillator model with a distribution of force constants[68] and the mode coupling theory.[69] Nevertheless, the boson peak can be considered as unexplained and no consensus on its microscopic origin has been found. In fact, its origin still is controversially debated.[68,70–78]

2.3 Hallmark features of glass-forming liquids

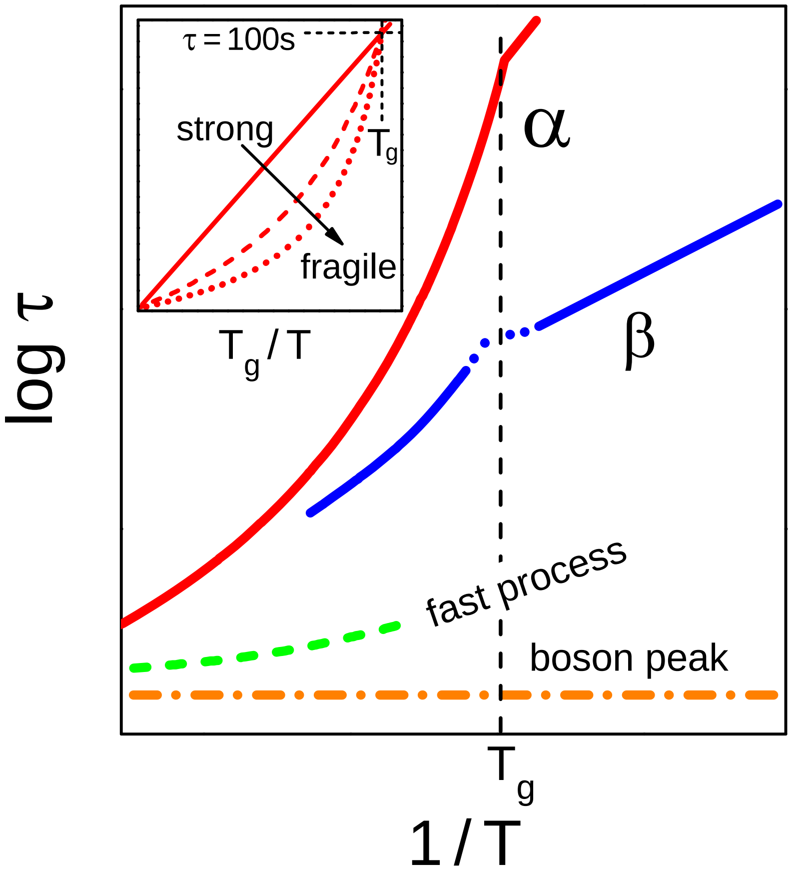

Figure 2.6: Schematic relaxation map of the most commonly observed relaxation phenomena in glass-forming matter.[17] α- and β-relaxation times often deviate from the thermally activated Arrhenius behaviour above T_g. In the glassy state, $T < T_g$, both relaxations are known to show Arrhenius behaviour. However, the behaviour of the β-relaxation times close to T_g is still not clarified. The boson peak is rather temperature independent. For the fast process, the minimum-frequency was taken to assign a relaxation time to this process. The inset shows an Angell plot[79,80] (x-axis scaled on T_g), so that all curves intersect at $\tau = 100s$. The typical behaviour of strong and fragile glass formers is displayed.

Figure 2.6 shows a schematic relaxation map of the most common processes in glass-forming materials in Arrhenius representation (log τ *vs.* $1/T$). At temperatures above the glass transition temperature T_g, α- and β-relaxation times (solid lines) show a stronger temperature dependence than thermally activated. In the glassy state, the β-relaxation times often show Arrhenius behaviour and out of equilibrium, the α-relaxation times seem to act the same way. However, the behaviour of the β-relaxation close to T_g is still not clarified. Sometimes a kind of minimum seems to show up in the relaxation times (dotted blue line).[81,82] A possible explanation for this behaviour is given by the so-called minimal model,[82] which is explained in section 2.4.2. The boson peak behaves rather temperature independent (dash dotted line). To assign a relaxation time to the fast process (dashed line), the minimum frequency ν_{min} was taken.

In the following, three hallmark features which are often said to be universal features of glass-forming liquids are shortly explained. They are also known as the three non's,[16,17] namely the non-exponential relaxation functions, the non-Arrhenius behaviour and the non-ergodicity.

2.3.1 Non-Arrhenius behaviour

The first *non* is the non-Arrhenius temperature dependence of the α-relaxation time τ or the viscosity $\eta \sim \tau$. The inset in figure 2.6 shows the so-called "Angell-plot".[83,84] In this kind of representation the abscissa is normalized to unity at T_g, defined as the temperature when the relaxation time τ equals 100s. In the naive picture of a double-well potential, where the particles try to overcome the energy barrier E_B with the attempt frequency $\nu_0 = 1/(2\pi\tau_0)$, thermally activated (Arrhenius) behaviour for the relaxation times is expected:

$$\tau = \tau_0 exp\left(\frac{E_B}{k_B T}\right) \tag{2.6}$$

The prefactor ν_0 is in the order of a typical phonon frequency. The Arrhenius law, however, only applies for very few liquids like e.g. SiO_2 or GeO_2. Most glass-formers show significant deviations from the thermally activated Arrhenius behaviour. Then the Vogel-Fulcher-Tamman expression[85,86] often provides a better description:

$$\tau = \tau_0 exp\left(\frac{DT_{VF}}{T - T_{VF}}\right) \tag{2.7}$$

Here, D denotes the strength parameter.[87] Small values of D characterize fragile, higher values strong glass formers. An alternative measure of the fragility is the fragility index m, defined as the slope at T_g in the Angell plot.[83,84]

Equation (2.7) implies a divergence of the relaxation times at the Vogel-Fulcher temperature T_{VF}. Real systems usually show deviations from the VFT-behaviour at high and low temperatures.[88,89] Up to now no divergence was observed as the system already falls out of equilibrium at the glass transition temperature $T_g > T_{VF}$. Originally, the VFT equation was purely phenomenological, but subsequently various models as, e.g., the Adam-Gibbs-Model[9] or the Free-Volume-Theory[10] give theoretical explanations.

2.3.2 *Non-exponential relaxation functions*

The second hallmark feature of supercooled liquids is the non-exponential nature of the response of the liquid to external perturbations. This is observed, e.g., if dipoles are temporarily subjected to an electrical field. It is well-known, that in nature hardly any exponential relaxation behaviour is found and after the perturbation, the dipoles will return to their equilibrium positions in a non-exponential way.[90] As shown in figure 2.7, this can be explained in two different ways.[91–93]

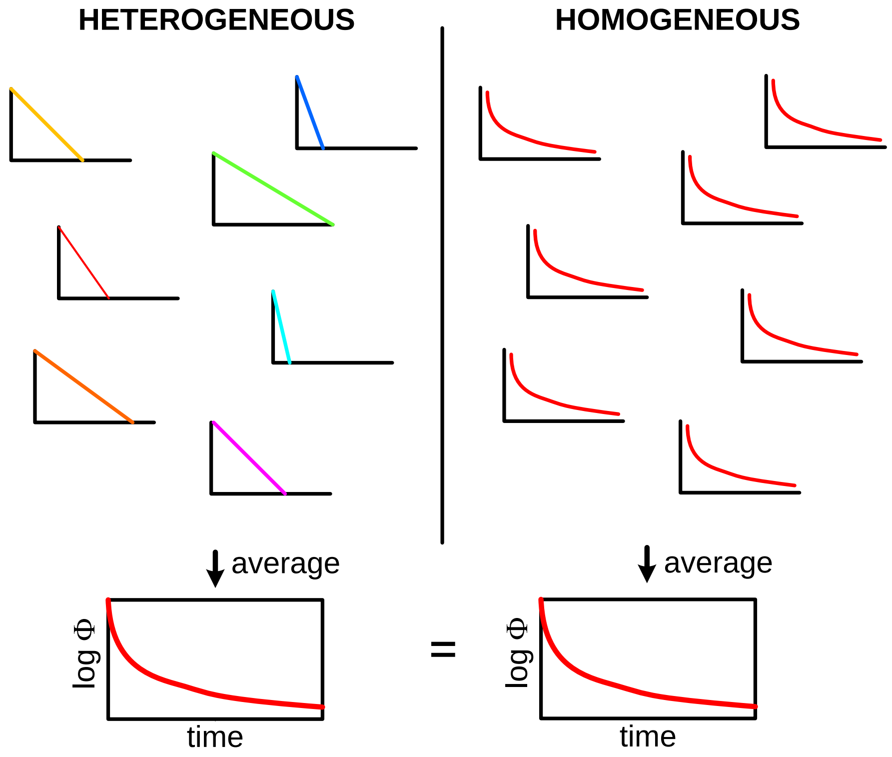

Figure 2.7: Heterogeneous and homogeneous nature of the non-exponentiality regarding an arbitrary relaxing quantity Φ. Different positions in the figure correspond to different positions in the sample.[94]

The heterogeneous scenario assumes that every molecule experiences a different environment by its surrounding neighbours. The relaxation in a given environment is nearly exponential but the relaxation times depend significantly on the particular surrounding. In the homogeneous scenario each molecule relaxes in a nearly identical but intrinsically nonexponential manner.[91]

Experimentally both scenarios are difficult to distinguish. However, 4-dimensional NMR, dielectric hole burning or solvation dynamics experiments verified the heterogeneous scenario and did not confirm the homogeneous one.[92,93,95,96]

2.3.3 Non-ergodicity

While the first two *nons* are usually observed at temperatures above the glass transition temperature T_g, ergodicity breaking arises under cooling when the sample falls out of thermodynamic equilibrium. This occurs for typical cooling rates close to T_g. The sample then remains in a structural state corresponding to equilibrium at higher temperature. This leads to the observation of quite challenging phenomena like aging, rejuvenation and memory effects.[24] Figures 2.8 (a) and (b) show the development of the frequency-dependent dielectric loss of the molecular glass-formers xylitol and propylene glycol during aging experiments.[25] As mentioned before, aging experiments gave strong hints, that the slow β-relaxation and the excess wing are due to the same microscopic origin. In Figures 2.8 (a) and (b) different spectra measured during aging at 157 K and at 243 K in the region of the secondary process are provided. For type-A and type-B glass formers, α- and β-peak clearly develop and separate during aging as both processes differently depend on temperature.

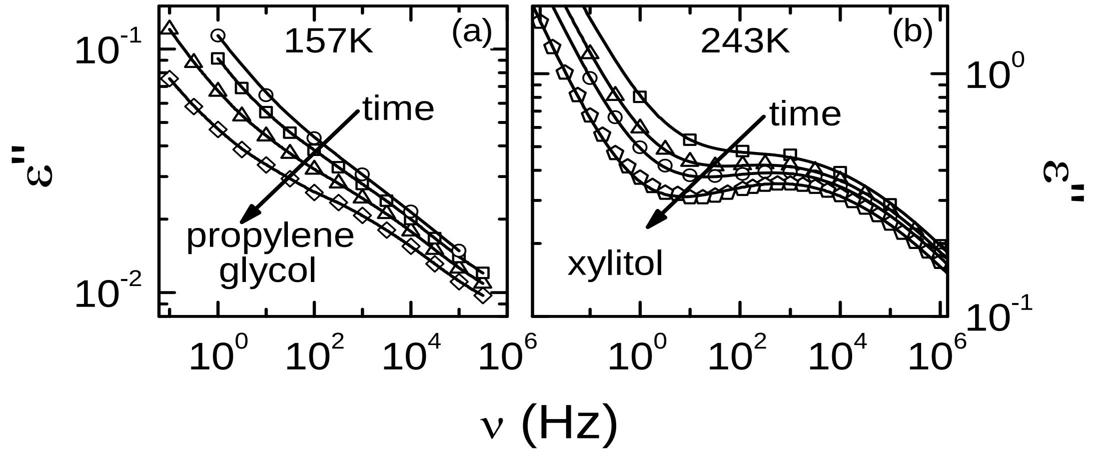

Figure 2.8: Spectra of the dielectric loss $\varepsilon''(\nu)$ of propylene glycol and xylitol measured at 157 K and 243 K respectively.[25] Spectra for various aging times up to 3 weeks are shown. For details, see Ref. 25.

Immediately after reaching 243 K, the dielectric loss in figure 2.8 (b) shows an overall decrease with increasing frequency and a distinct shoulder (uppermost curve). With increasing time the equilibrium is continuously recovered and the shoulder develops into a well-pronounced peak. The downward shift of the $\varepsilon''(\nu)$ curves seems to be the main effect of aging.[25]

2.4 Models and theories

Although there have been many attempts to understand the nature of the glass transition, no overall theory has been proposed that captures all features of glassy dynamics. However, a variety of different models and theories coexist.[15,91,97] Some assign a phase transition to a certain temperature ($< T_g$), where viscosity and relaxation times diverge. Others concentrate on a temperature region far above T_g and try to explain the slowing down of the liquid-like behaviour by means of a critical point at a temperature $T > T_g$. Also theories that do not find any temperature of unique importance are known from literature. Models and theories used for parameterization of experimental data in this work are briefly discussed in the following section.

2.4.1 Explanations of the Johari-Goldstein (JG) β-relaxation

In the 1970ies Johari and Goldstein[28,29] demonstrated that secondary relaxation processes also show up in relatively simple and rigid molecules. In this case, intramolecular motions, often held responsible for the slow β-relaxation can be excluded. This led to the conclusion that the occurrence of these so-called Johari-Goldstein (JG) β-relaxations may be inherent to glass forming materials in general.[28,29] However, the microscopic origin behind this process is still unclear and controversially debated.[98] In literature mainly two different explanations for the JG-process appear. One is due to so-called islands of mobility,[28–30] the other to small angle reorientations.[99–101] To get a general idea, both are briefly outlined in the following.

- ***Islands of mobility***

Johari and Goldstein have been the first who associated the β-process with "islands of mobility".[28–30] They argued, that statistically distributed regions of lower density should exist in the glass. In these loosely packed regions, some molecules have more space and therefore more degrees of freedom to orientate. They are encaged by denser packed, more immobile neighbouring molecules. From this point of view, the JG-relaxation is an inhomogeneous process involving only few molecules, which are sufficiently mobile in their local environment.[26]

- ***Energy landscape and small-angle reorientations***

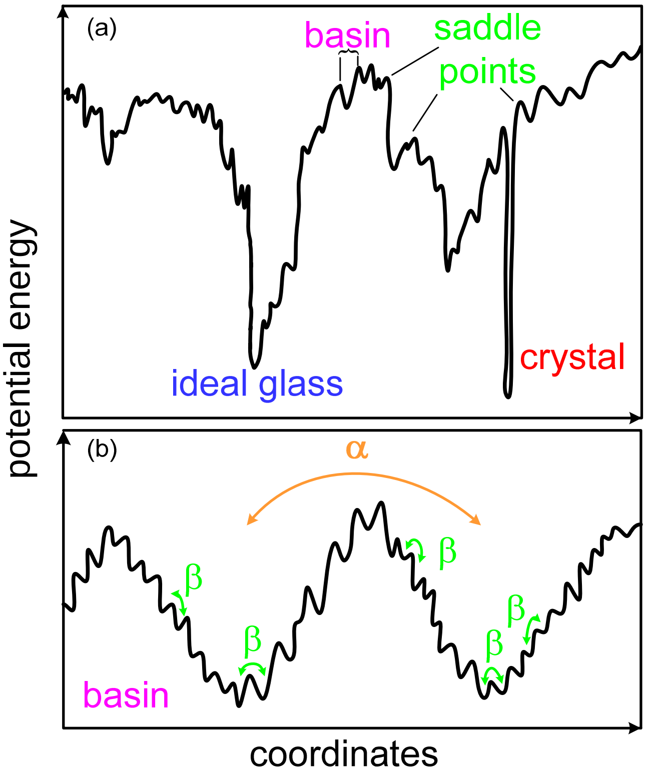

Figure 2.9 (a): Schematic illustration of the potential energy landscape for a many-particle system in the multidimensional configuration space.[27] In (b) α- and β-relaxations are visualized for one particle.[27] The α-relaxation is associated with large distance transitions between two metabasins, the β-relaxation with small interbasin transitions (small angle reorientations).[4,27,102]

The energy landscape picture is a convenient framework for the description of the relation between α- and β-relaxation dynamics.[4,26,27,102] For the potential energy function of a N-body system $\Phi(\overrightarrow{r_1}, \dots, \overrightarrow{r_n})$, with $\vec{r_i}$ providing the spatial location for each particle, a topographical view is adopted to gain a better understanding of the basic phenomena in glass-forming liquids. This is schematically displayed in figure 2.9. Such a simplified illustration can be misleading but also can explain some key points. The number of potential energy minima of a given depth and the type of the saddle-points separating neighbouring minima are of special interest. The sharpest and lowest lying minima correspond to stable configurations in thermal equilibrium and are related to a virtually perfect crystal. The ideal glass is characterised by a deep but broader minimum. Higher lying minima are assigned to metastable amorphous particle packings. As shown in figure 2.9 (b), the structural α-relaxation corresponds to large distance transitions between metabasins. These basins exhibit some kind of "fine structure". Transitions in this interbasin structure are associated with the slow β-relaxation.

The other point of view assumes that the β-process may be attributed to faster, small-angle motions. After undergoing one or more small-angle reorientations, the same molecule can cooperatively undergo a large angle reorientation, which characterizes the structural α-relaxation. In contrast to the prior picture of islands of mobility, not only a few but all molecules give rise to the β-relaxation. One and two-dimensional ^{2}H-NMR studies provide strong indications that the secondary relaxation can be related to small angle jumps.[4,99–103]

2.4.2 Minimal model

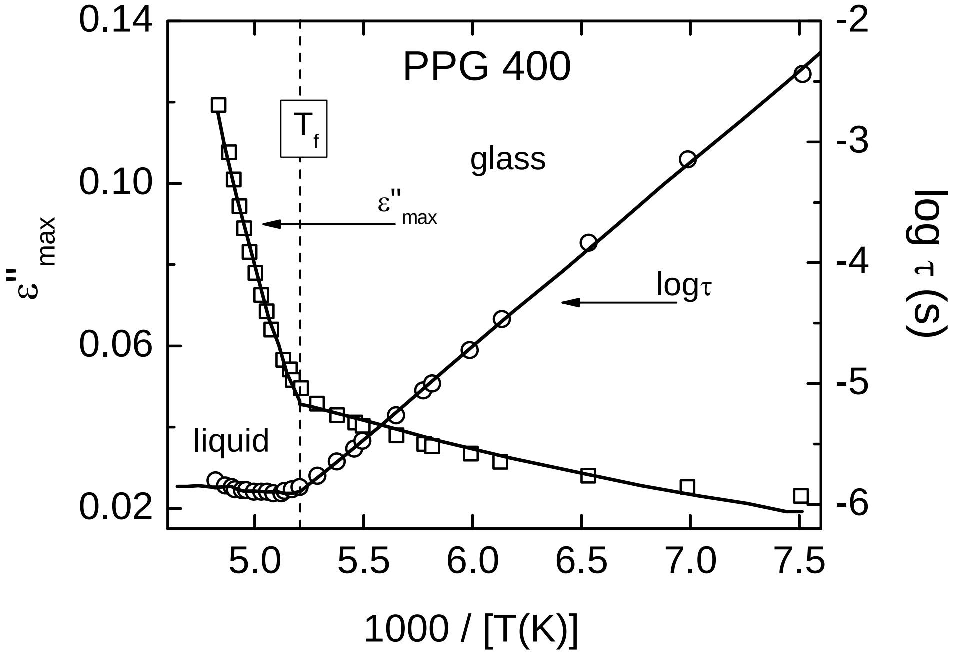

Figure 2.10: Temperature dependence of the relaxation time τ and the maximum dielectric loss ε''_{max} for the polymer polypropylene glycol 400 (PPG400).[104] Solid lines show fits obtained from equations (2.8) and (2.9).

Dyre and Olsen[82] developed the so-called minimal model for β-relaxations (MM). For the liquid phase, the minimal model predicts a strong increase of the β-relaxation strength with temperature,[105] while the peak frequency in the liquid phase is considered as temperature independent or at least as only weakly temperature dependent.[106] In the glassy phase, the loss peak frequency is strongly temperature dependent, while the maximum loss varies only slightly. A characteristic feature is the minimum that appears in $\log_{10}\tau\ (T^{-1})$ around the fictive temperature T_f, as shown in figure 2.10 for PPG 400.

This characteristic behaviour is exemplarily displayed in figure 2.10. Here, data for the polymer polypropylene glycol 400 (PPG 400) from Paluch *et al.*[104] is shown. The transition from the liquid to the glassy state is characterized by a clear change in the behaviour of ε''_{max} and τ. The corresponding temperature, where this transition takes place is called fictive temperature, T_f. The concept of the fictive temperature goes back to A.Q. Tool,[108] and characterizes the equilibrium temperature of the sample having the same properties as the non-equilibrium sample at a temperature below the glass transition.

According to Dyre and Olsen,[82] the strong increase of the maximum loss ε''_{max} with increasing temperature at $T > T_f$, indicates a pronounced asymmetry of the relaxing entity. For this reason, a standard asymmetric double-well potential is adopted for the model. This potential, as shown in figure 2.11, is characterized by two free energies, U and Δ, which vary with temperature in the equilibrium phase, but freeze in the glassy state. The loss peak frequency f_{max} and the maximum dielectric loss, ε''_{max} are given by the following equations:[82,107]

$$f_{max} = f_0 \exp\left(\frac{-2U + \Delta}{2k_BT}\right) \cosh\left(\frac{\Delta}{2k_BT}\right) \tag{2.8}$$

$$\varepsilon''_{max} = \varepsilon_0(T) \cosh^{-2}\left(\frac{\Delta}{2k_BT}\right) \tag{2.9}$$

Here, f_0 is assumed to be structure and temperature independent, while $\varepsilon_0 = T_0/T$ is structure dependent. The free energy differences U and Δ (cf. figure 2.11) change with temperature, but freeze at the glass transition. In terms of the fictive temperature T_f, the minimal model is based on two equations for the liquid and the glassy state. For the glassy state, the temperature independent equations

$$U = U_0 + ak_BT_f \tag{2.10}$$

and

$$\Delta = \Delta_0 - bk_BT_f \tag{2.11}$$

are given. In the liquid state, T_f has to be replaced by T in equations (2.10) and (2.11), leading to temperature dependent equations.

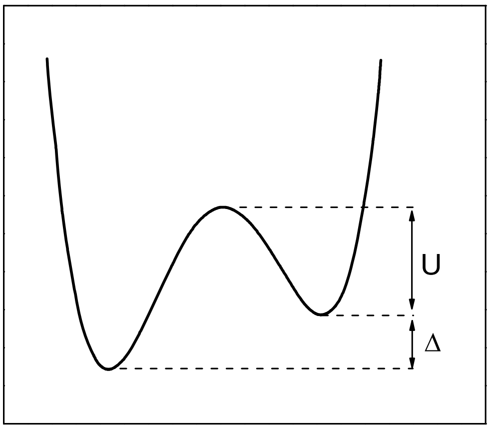

Figure 2.11: Asymmetric double well potential with two free energy differences U and Δ. These vary as structure changes with temperature in the liquid phase but freeze at the glass transiton. From Ref. 82.

However, one has to keep in mind, that the minimal model is a clearly oversimplified model as it is based on very simple assumptions. Nevertheless, it is a useful tool for data parameterization and quantifies the contrasts between β-relaxation in the liquid and the glassy state.[82]

2.4.3 Coupling model

The main assumption of the coupling model (CM)[109–111] is the existence of a temperature independent crossover time t_c where a change in the relaxation behaviour takes place. For short times, $t < t_c$, the molecules are assumed to relax independently and therefore exponentially:

$$\phi(t) = \exp\left(-\frac{t}{\tau_0}\right) \tag{2.12}$$

$\phi(t)$ denotes the relaxation function and τ_0 is the so-called primitive relaxation time for the α-process. Because of intermolecular interactions, cooperativity arises for $t > t_c$. This leads to a distribution of relaxation times and to a non-exponential function for the relaxation times:

$$\phi(t) = \exp\left[-\left(\frac{t}{\tau_\alpha}\right)^{1-n}\right] \tag{2.13}$$

n is called coupling parameter, and directly connected to the exponent $\beta^{*}=(1-n)$ of the stretched exponential KWW function. Continuity of both relaxation functions at $t = t_c$ implies:

$$\tau_\alpha = \left[t_c^{-n}\tau_0\right]^{\frac{1}{1-n}} \tag{2.14}$$

Based on experimental results, t_c is assumed to have approximately the value of 2 ps for small molecular glass-formers.[110,111] The primitive relaxation time τ_0, calculated from equation (2.14) is assumed to be comparable to the β-relaxation time τ_β. As the primitive relaxation is of Debye type while the JG β-relaxation strongly deviates from this behaviour and in most cases is characterized quite well by the much broader Cole-Cole function, it becomes clear that both processes cannot be identical. However, due to Ngai[32] the slow β-process and the primitive α-relaxation are not the same, but they are merely related as "close cousins". Nonetheless, the coupling model often is believed to give a criterion for the genuine JG β-relaxation.

2.4.4 Extended coupling model

In contrast to the coupling model, which is focussed on the long time dynamics, the extended version[55] pays attention to the short time dynamics, when all relaxing units are caged by its neighbouring molecules, and to intermediate time scales when an increasing number of molecules is no longer caged. A schematic illustration of a particle motion in the transient cage, formed by its neighbours is provided in figure 2.12. The shallowness of the minimum is ascribed to a nearly-constant-loss (NCL) contribution. This behaviour is schematically illustrated in figure 2.13 (a). However, no JG process or excess wing is included as the situation at high temperatures is shown, where these features have merged with the α-relaxation.[17]

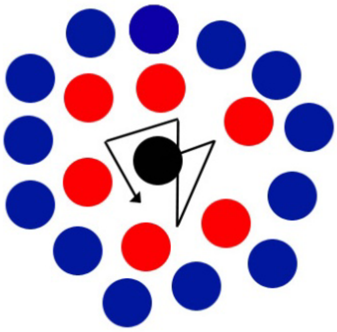

Figure 2.12: Schematic illustration of particle motion in the transient cage formed by its neighbours.

One possibility for the description of $\chi''(\nu)$ or $\varepsilon''(\nu)$ spectra is the additive superposition of different contributions to the susceptibility. In this description a sublinear power law $c_b\nu^{-b}$ $(b < 1)$ accounts for the high-frequency wing of the α-peak and an increase $c_n\nu^n$, steeper than linear $(n \geq 1)$, is commonly assumed[112] for the low frequency wing of the boson peak. To take account of the rather shallow minima in $\chi''(\nu)$ or $\varepsilon''(\nu)$ the addition of a constant loss ε_c turned out to be necessary.[54,112,113] Such a constant-loss contribution was early proposed by Angell and co-workers.[114–116] Mainly in ionically conducting glass-formers many indications for an approach of a constant loss were found at high frequencies and low temperatures. The explanation of the NCL[55] in the framework of the extended coupling model is that most molecules are still 'caged'. This means that they have not made themselves to get out of the cages, formed by its neighbours by an independent reorientation. Despite a couple of explanations for the constant loss,[56–58,117–119] the microscopic origin of this phenomenon still remains unclear.
In addition to the constant loss, in some glass-formers a power law with an exponent near 0.3 was found.[54,113,116,120] Ngai *et al.*[116] claimed this power law to be ubiquitous, at least in glassy ionic conductors. To achieve a smooth transition to the α-peak a power law, $c_\beta\nu^{-\beta}$, is included, and $0 < b < \beta < 1$ should hold. Then, one arrives at:

$$\varepsilon'' = c_\beta\nu^{-\beta} + c_b\nu^{-b} + \varepsilon_c + c_3\nu^{0.3} + c_n\nu^n. \tag{2.15}$$

This[121] should enable a phenomenological description of the spectra from the α-peak up to the boson peak. However, one should keep in mind, that also other ways of combining different contributions have been proposed.[122–124]

2.4.5 Mode coupling theory (MCT)

In the high frequency region a minimum is expected. The low frequency flank of the minimum is caused by the right flank of the α-process, the excess wing, the JG β-peak or any other secondary relaxation. The high frequency flank should correspond to the increase towards the boson peak. Experimentally, indeed a minimum is observed, but it is too shallow to be explained by a simple superposition of low and high frequency peaks.[3,51–54] This gives evidence for excess intensity in the minimum region (indicated in orange in figure 2.3) due to one (or more) fast processes.

Mode coupling theory (MCT), one of the most prominent theories of the glass transition,[11–14,125] predicts the existence of additional excess intensity at high frequencies (about 100 MHz – 1 THz), due to a fast process, called fast β-relaxation. In the framework of MCT, a dynamic phase transition at a critical temperature T_c is assumed for the explanation of the glass transition. A two step relaxation for $\Phi_\mathrm{q}(\mathrm{t})$ is predicted for temperatures $T > T_c$. The initial relaxation step is ascribed to the fast β-relaxation and explained by the 'rattling' movement of a particle in the transient cage, formed by its neighbouring molecules, as schematically drawn in figure 2.12. The second relaxation step accounts for the α-relaxation and is associated with the decay and the formation of the cage. In the framework of this theory, distinct predictions are maid about the power law exponents a and b, and the temperature development of minimum frequency and amplitude. The behaviour of the minimum manifests itself in the so-called critical laws. This is the "classical" scenario of MCT, sketched in figure 2.13 (b).

In recent works[126,127] it was pointed out, that the fast β-process in fact can lead to a symmetrically broadened peak, well approximated by a CC function. In figure 2.13 (b), this peak is located at very high frequencies and only its left wing influences the minimum. For the explanation of OKE data of benzophenone,[128,129] Götze and Sperl accounted for reorientational-translational coupling in an schematic model. This explanation is based on an earlier theoretical work[130] and as a result, they pointed out, that the fast β-relaxation indeed can lead to a CC-peak that can be located at lower frequencies. This is schematically shown in figure 2.13 (c),[131] and it is clearly seen that the CC peak causes a second, shallower power law ν^{-a} at the high-frequency flank of the α-relaxation peak. Of course, also intermediate situations are possible, leading to a shoulder or a secondary peak.

MCT is based on regular equations of motion for a set of autocorrelation functions (cf. appendix 6.2). These so-called mode-coupling equations are integro-differential equations, consisting of a memory kernel, introducing non-linearity. Starting from the original work[11–13] different schematic models, mainly assuming different simplified polynomials in the memory kernel, have been developed during the recent years. In the following, a short overview on MCT and its predictions is given. For details on the theoretical basis see ,e.g., references 14, 133 and 134.

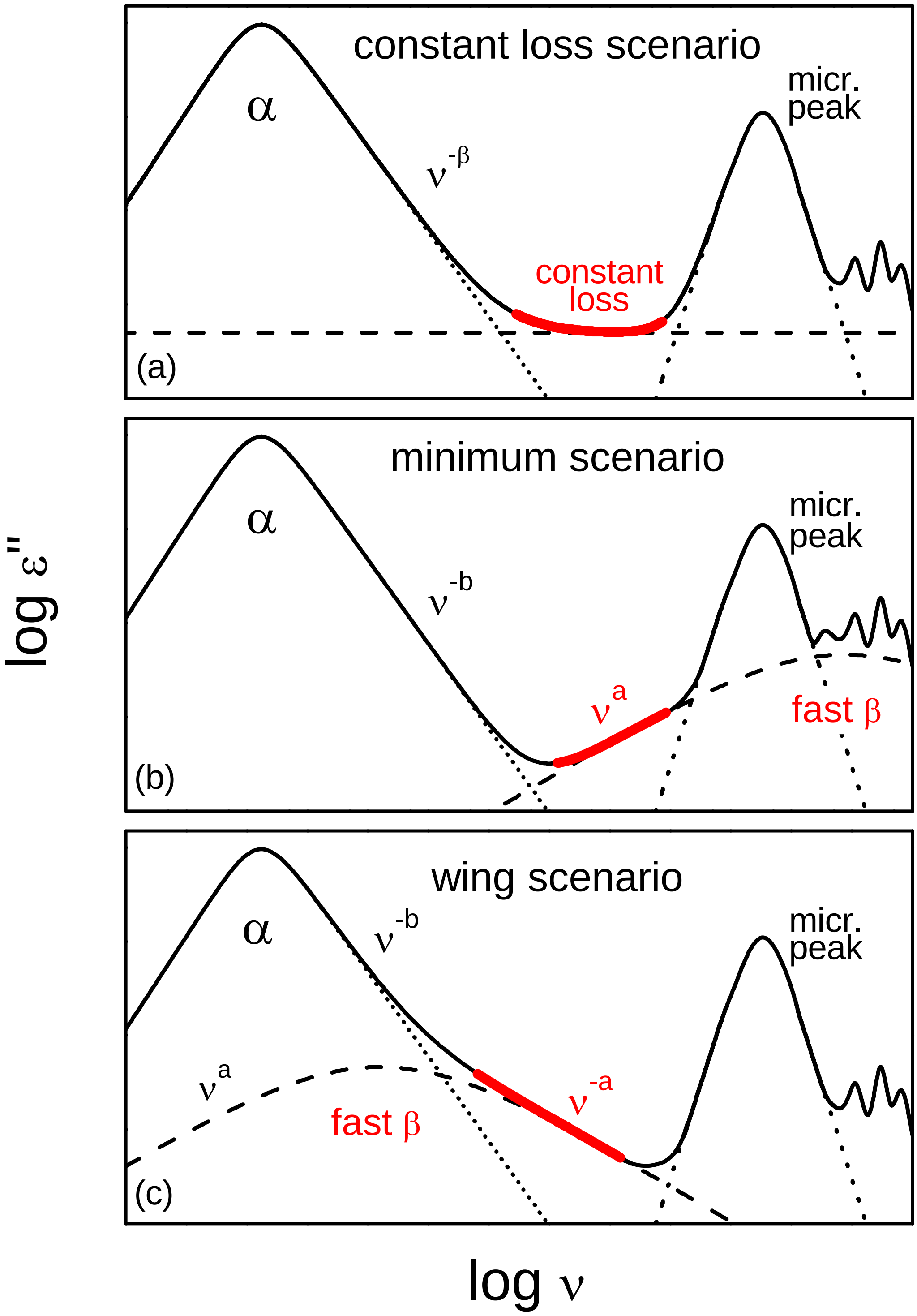

Figure 2.13: Schematic illustration of different scenarios explaining the excess intensity due to a fast process in the minimum region. In frame (a) a constant loss contribution is assumed.[1,55–58,114,115,132] In the other two frames two different scenarios of MCT are shown. Here, the fast process gives rise to a CC peak. The conventional case of a minimum or a wing at the high-frequency flank of the α-peak can arise, depending on the position of the CC peak in the frequency spectra. Red lines indicate the excess intensity that arises from each of the three scenarios.

- ***Background and basic equations***

MCT is formulated as function of the wave vector q and time $t,$ and based on a generalized oscillator equation of motion for the density autocorrelation function $\Phi_q(t)$, which is directly connected with the static structure factor $S(q)$. Equation (2.16) has to be solved for $t > 0$:[134,135]

$$0 = \ddot{\Phi}_q(t) + \gamma_q \, \Omega_q^2 \dot{\Phi}_q(t) + \Omega_q^2 \Phi_q(t) + \Omega_q^2 \int_0^t \mathrm{d}t' m_q(t - t') \dot{\Phi}_q(t') \tag{2.16}$$

Ω_q denotes the characteristic frequency of the liquid dynamics. It is defined as $\Omega_q = \left(q^2 v^2 / S_q\right)^{0.5}$ where v is the thermal velocity, and S_q the static structure factor. For microscopic wave vectors q, Ω_q is in the order of a typical phonon frequency (10^{-12} - 10^{-14} s^{-1}).[14] $\gamma_q \, \dot{\Phi}_q(t)$ is the a friction term in the equation of motion.

The heart of equation (2.16) is the memory kernel, $m_q(t)$ and since this kernel has not been specified yet, equation (2.16) is formally exact. $m_q(t)$ is now expanded in polynomials of density fluctuations, then all terms are factorized into pair correlations. In lowest order, the bilinear functional

$$m_q\{\Phi(t)\} = \sum_{p+k=q} V_{qpk} \Phi_p(t) \Phi_k(t) \tag{2.17}$$

with coupling coefficients V_{qpk}, is obtained. They can be derived by neutron scattering experiments from the static structure factor $S(q)$.

Equations (2.16) and (2.17) assume a liquid, containing identical, spherical particles. However, real-life liquids include orientational and intramolecular degrees of freedom, which lead to extreme calculational difficulties. Nevertheless, different schematic models for dumbbell molecules in a simple liquid[136] or for linear molecules,[137] e.g., have been developed.

One so-called schematic model is the minimal F_{12} model.[138] Here, one correlator $\Phi(t)$ and two coupling coefficients, v_1 and v_2, are sufficient to obtain relaxational stretching and the ideal glass transition. In this case the quadratic mode coupling polynomial reads as:

$$m(t) = v_1 \Phi(t) + v_2 [\Phi(t)]^2. \tag{2.18}$$

With one more correlator, $\Phi_s(t)$, spectra with arbitrary α-relaxation strengths can be created. Then the memory kernel[11,139]

$$m_s(t) = v_s \Phi(t) \Phi_s(t) \tag{2.19}$$

couples $\Phi_s(t)$ to $\Phi(t)$, which is independent on $\Phi_s(t)$.

- ***Main predictions of idealized MCT***

One of the main outcomes of MCT is the prediction of non-trivial additional intensity in the minimum region of $\varepsilon''(\nu)$ or $\chi''(\nu)$. As mentioned before, the glass transition is explained in terms of a dynamical phase transition at a critical temperature T_c. This temperature often was found to be considerably higher then the glass transition temperature T_g. Within idealized MCT, the low and high frequency wings close to the minimum region between the α-relaxation and the microscopic peak, are expressed by power laws for T above but near T_c[II]:

$$\varepsilon'' = \frac{\varepsilon_{min}}{a+b}\left[a\left(\frac{\nu}{\nu_{min}}\right)^{-b} + b\left(\frac{\nu}{\nu_{min}}\right)^{a}\right] \tag{2.20}$$

The power laws ν^a and ν^{-b} are often referred to as the von Schweidler (ν^{-b}) and the critical (ν^a) law. ε_{min} and ν_{min} denote minimum amplitude and position. The real part ε', directly accessible by dielectric spectroscopy, is predicted as[3]

$$\varepsilon' = f_e + \frac{\varepsilon_{min}}{a+b}\left[a\cot\left(b\frac{\pi}{2}\right)\left(\frac{\nu}{\nu_{min}}\right)^{-b} - b\cot\left(a\frac{\pi}{2}\right)\left(\frac{\nu}{\nu_{min}}\right)^{a}\right], \tag{2.21}$$

where f_e denotes a constant. The exponent parameters a and b are temperature independent and connected with each other by the so-called exponent parameter λ, where Γ denotes the Gamma function:

$$\lambda = \frac{\Gamma^2(1-a)}{\Gamma(1-2a)} = \frac{\Gamma^2(1+b)}{\Gamma(1+2b)} \tag{2.22}$$

This relation restricts the exponent a to values below 0.4. Within idealized MCT, three critical laws are predicted, connecting the α-relaxation time $\tau_\alpha = 1/(2\pi\nu_\alpha)$, the minimum position ν_{min} and the minimum amplitude ε_{min} with the critical temperature T_c. The critical behaviour for $T > T_c$ for the α-relaxation timescale reads as:

$$\nu_\tau \propto (T - T_c)^\gamma, \tag{2.23}$$

[II] Equation (2.21) represents an interpolation and is used instead of the full series expansion of g_λ.[140] For the interpretation of dielectric data the small numeric difference between the two expressions has no importance.[141]

with the critical exponent γ:

$$\gamma = \frac{1}{2a} + \frac{1}{2b} \tag{2.24}$$

For minimum amplitude and position, following relations hold:

$$\varepsilon_{min} \propto (T - T_c)^{1/2} \tag{2.25}$$

$$\nu_{min} \propto (T - T_c)^{1/2a} \tag{2.26}$$

At T_c, a significant change in the behaviour of $\varepsilon''(\nu)$ is predicted: Ergodicity is broken at the critical temperature, the α-peak should vanish and a "pure" critical law, $\varepsilon'' \propto \nu^a$ should be observed. At lower temperatures a so-called "knee" should show up in $\varepsilon''(\nu)$ at a frequency ν_k. It should be possible to observe this phenomenon as a change of power law from $\varepsilon'' \propto \nu^a$ at $\nu > \nu_k$ to $\varepsilon'' \propto \nu$ at $\nu < \nu_k$.

A schematic loss spectrum for the minimum scenario of MCT is shown in figure 2.13 (b). The combination of two asymptotic power laws, namely the critical law and the von Schweidler law is indicated. They form a shallow minimum in the frequency dependent loss, followed by the so-called microscopic peak located in the THz regime. The high frequency flank of the α-relaxation peak directly crosses over into the von Schweidler law. An excess wing or a JG-β relaxation seems not to be covered by MCT.

- ***Main predictions of extended MCT***

In idealized MCT, a transition to a non-ergodic state of the system is predicted and equation (2.23) implies a divergence of the α-relaxation time at T_c. This is inconsistent with experimental results, as neither the minimum nor the α-relaxation peak vanishes below T_c.

Within extended MCT[14] the complete structural arrest for $T < T_c$ is restored by the assumption of thermally activated hopping processes. They permit a diffusive motion of the particle out of the cage (cf. figure 2.12) to restore the α-relaxation process and ergodicity. T_c represents a crossover-temperature between the dominating cage effect in the liquid phase and the activated hopping processes at lower temperatures.

2.4.6 Ionic conductivity: phenomenological approaches and models

The complex conductivity $\sigma^* = \sigma' + i\sigma''$ is directly connected with the complex dielectric constant ε^* via the equation $\sigma^*(\omega) = i\omega\varepsilon_0\varepsilon^*(\omega)$. Real and imaginary part can be written as:

$$\sigma'(\omega) = \omega\varepsilon_0\varepsilon''(\omega) \quad \text{and} \quad \sigma''(\omega) = \omega\varepsilon_0\varepsilon'(\omega) \tag{2.27}$$

From this, it is obvious, that the conductivity can give rise to a contribution in ε^*.
If ions with charge q are subjected to an electrical field, the dc-conductivity results to be proportional to the ion charge, the number of mobile ions and how easily ions are moved through the solid. This is expressed in

$$\sigma_{dc} = qn_m\mu, \tag{2.28}$$

where the ion mobility μ is defined by $\mu = v/E$, with v the velocity and E the electrical field. The number of mobile ions per volume is n_m and the current density $J = qn_mv$. The dc-conductivity σ_{dc} is connected to this quanitiy via the electric field: $\sigma_{dc} \equiv J/E$.[142]
Ion conduction in glasses, polymers and other disordered materials plays an increasingly important role in technology. However, the transport mechanisms of ions in a disordered matrix are still only poorly understood[142] and no unique and commonly accepted model but a variety of different models exist.

2.4.6.1 Universal dielectric response and superlinear power law

The so-called universal dielectric response (UDR) is a phenomenological approach to account for the frequency dependence of hopping conduction and was developed by Jonscher in the 1970ies.[143,144] After extensive investigations of the dielectric response of different materials, Jonscher discovered a universality in form of a sublinear power law in the frequency dependent conductivity $\sigma'(\omega) \sim \omega^s$. To low frequencies, $\sigma'(\omega)$ tends to a constant dc-conductivity. Via the Kramers-Kronig relation, the imaginary part $\sigma''(\omega)$, also showing up as a power law with the same exponent s, is obtained. In summary this reads as:

$$\sigma' = \sigma_{dc} + \sigma_0\omega^s \tag{2.29}$$

$$\sigma'' = \tan\left(\frac{s\pi}{2}\right) \cdot \sigma_0\omega^s \text{ with } 0 < s \leq 1 \tag{2.30}$$

The exponent s, which mostly is between $0.5 < s < 1$, can give evidence about the hopping mechanism and the kind of charge carriers when comparing its temperature dependence with the predictions of explicit models.[145,146]

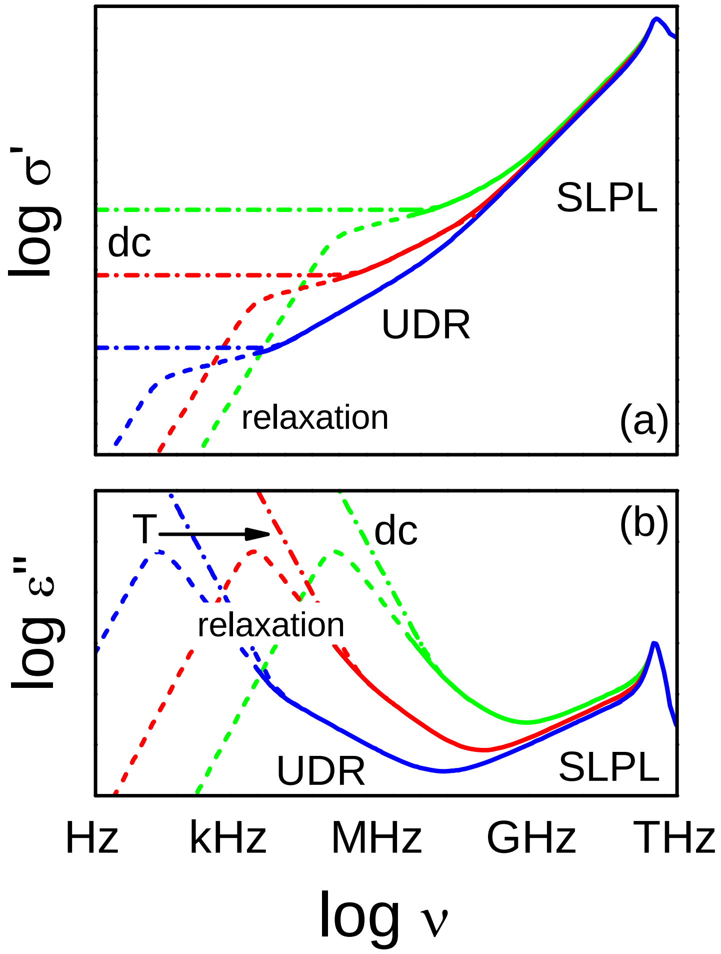

Figure 2.14: Schematic illustration of the frequency-dependent response of disordered matter for three temperatures.[147] For non-conducting dipolar systems, relaxational behaviour is observed at low frequencies (dashed lines). For conducting systems this is covered by dc-conductivity (dash-dotted lines). Solid lines indicate the regions of universality. In the far-infrared region, the boson peak shows up. A rough indication of the frequency ranges is given at the abscissa.

By measuring the extreme broadband dielectric response of different disordered materials, a further astonishing universality, the so-called superliner power law (SLPL),[147] was found. This power law with an exponent significantly smaller than 2 follows the UDR-behaviour at higher frequencies. The interplay between UDR, SLPL and dc-conductivity is schematically shown for σ' and ε'' in figures 2.14 (a) and (b) for a system with excess wing for three temperatures. The dashed lines show relaxation behaviour for non-conducting systems, while the dash-dotted lines ascribe for conducting ones. Solid lines indicate the regions of universality. In the THz region the boson peak shows up.

3 Measurement techniques

3.1 Dielectric measurements

To obtain dielectric spectra in a broad frequency range, a variety of different measurement principles has to be applied. Figure 3.1 gives an overview of the different devices and techniques, available in the dielectric laboratory at the University of Augsburg.[3,148] In principle a range of up to 21 decades in frequency can be covered.

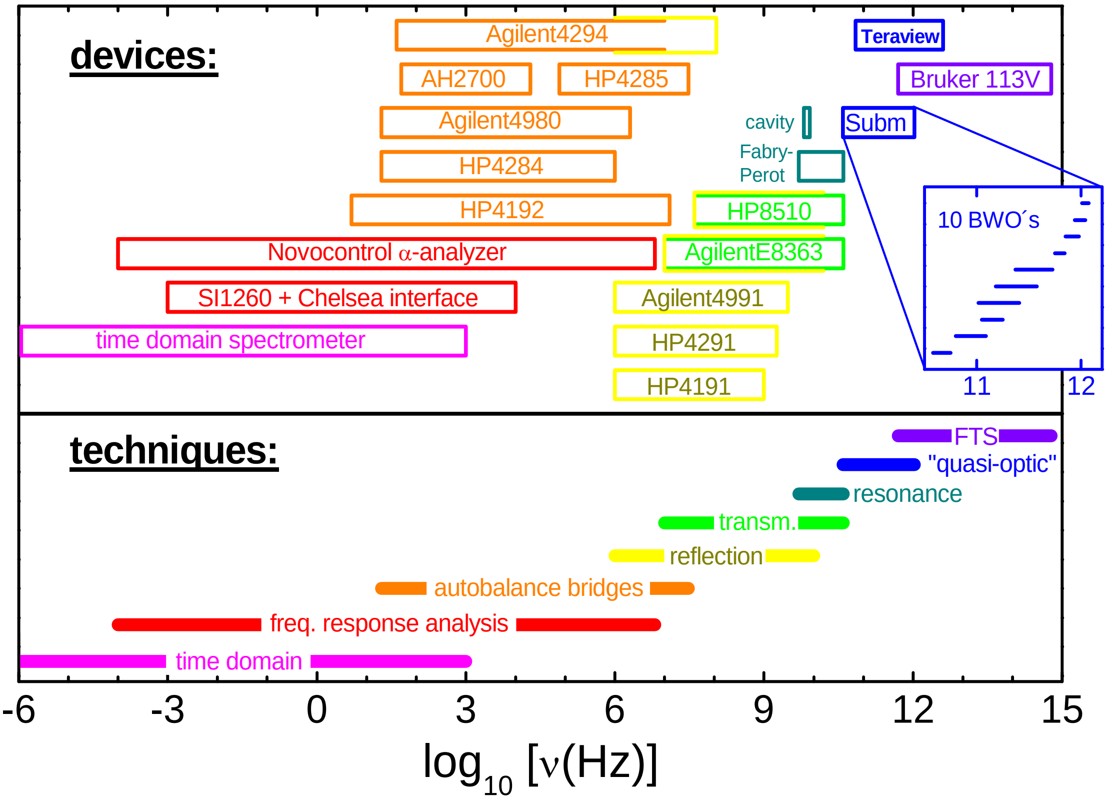

Figure 3.1: Overview of different devices and techniques related to their frequency ranges.[17] For details see Refs. 1 and 148.

Depending on the technique, different sample geometries are necessary. These are schematically shown in figure 3.2. At low frequencies, up to several MHz, a parallel-plate capacitor geometry is used (figure 3.2 (a)). The samples that have been measured for this work are liquid at room temperature and filled in specially designed parallel-plate capacitors. Small plate distances, guaranteed by the use of glass-fibre spacers, and large areas of the capacitor plates are necessary for the detection of low dielectric losses, which, e.g., can arise at low temperatures. The capacitance C' and the conductance G' of the sample capacitor are measured in dependence of frequency. The dielectric permittivity is then easily calculated via the relations $\varepsilon' = C'/C_0$ (C_0 the empty capacitance) and $\varepsilon'' = G'/(2\pi\nu C_0)$.

In the frequency region from about 1 MHz to some 10 GHz coaxial reflection and transmission techniques are employed. For former, the investigated material is mounted at the end of a coaxial line, bridging inner and outer conductor (figure 3.2 (b)).[148,149] Small parallel-plate capacitors are used for liquid samples. The geometry used for coaxial transmission measurements is shown in figure 3.2 (c). In this case the liquid sample is filled into a coaxial line or wave guide.[3,148,150] After proper calibration the transmission of the line is measured by a network analyser. To determine the dielectric materials properties, multiple reflections within the line have to be taken into account.

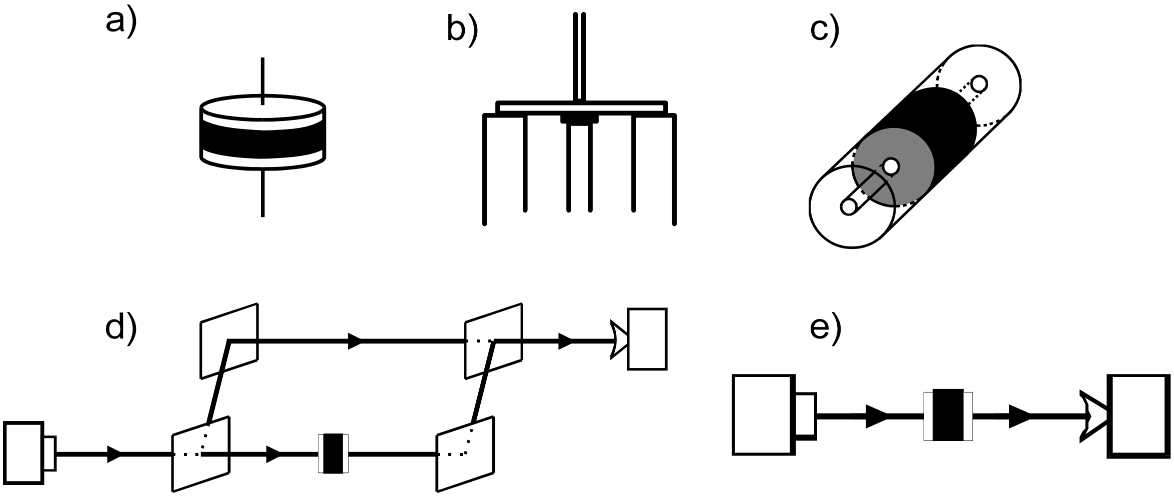

Figure 3.2: Schematic overview[17] of the typical sample geometries used for the different measurement techniques: (a) parallel plate capacitor for autobalance bridges and frequency-response analysis,[148] (b) setup for coaxial reflection measurements,[148,149] (c) coaxial transmission line,[148,150] (d) scheme of the Mach-Zehnder spectrometer used for measurements in the submillimeter wavelength range,[151,152] (e) sample geometry as used in the Fourier-transform-infrared (FTIR) spectrometer for transmission measurements. Black filled regions indicate the sample material.[17]

For measurements up to THz (60 GHz – 1.2 THz) a spectrometer based on the principle of a Mach-Zehnder interferometer, where both, transmission and phase shift of unguided electromagnetic waves through the sample are detected, is used[153] (figure 3.2 (d)).

At the highest frequencies, from far-infrared to the optical range a commercial Fourier-transform spectrometer is employed (figure 3.2 (e)).[148,149] In contrast to submillimeter wave spectroscopy, it is not possible to measure transmission and phase shift during an infrared measurement. It is necessary to use the Kramers-Kronig relation to calculate the phase from the measured transmission. All these techniques are explained in more detail in the following sections.

For cooling and heating different cryostats and ovens are employed. For frequency response analysis, autobalance bridges and reflection technique, in the frequency range from 10^{-3} Hz to 10^{9} Hz, a nitrogen-gas cryostat is best suited for temperatures between 140 and 600 K. For lower temperatures a closed cycle helium refrigerator system is used. For the transmission and "quasi-optic" technique special self-made ovens were used, while for IR measurements a commercially available Oxford cryostat was employed. For details see, e.g., Refs. 1, 17, 148 and 154.

3.1.1 Low frequency techniques

In the low frequency regime (10 μHz ≤ ν ≤ 10 MHz) basically two different devices have been used: (a) the alpha-A high performance frequency analyser from Novocontrol, covering a frequency window from 10 μHz ≤ ν ≤ 10 MHz and (b) the high precision LCR-meter HP 4284A from Hewlett Packard in the range from 20 Hz – 1MHz. Both devices use a different measurement technique.

- ***Frequency response analysis (Novocontrol α-analyser)***

Figure 3.3 shows the schematic circuit diagram of the frequency response analysis (Novocontrol α-analyser).

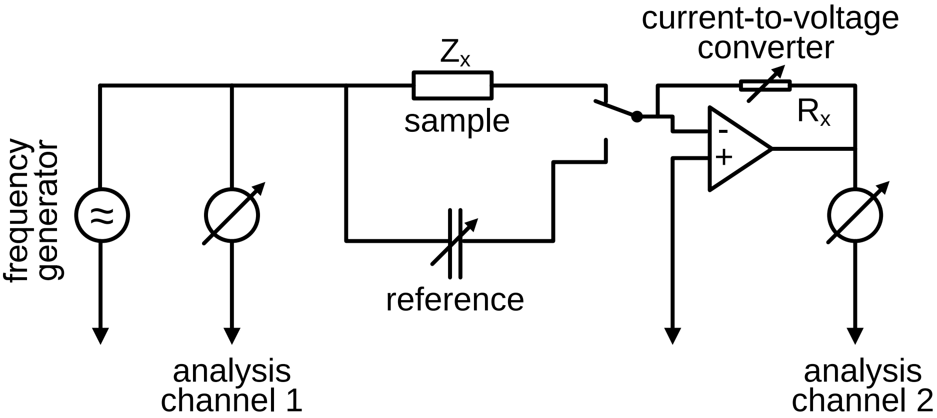

Figure 3.3: Schematic circuit diagram of the frequency response analysis (Novocontrol α-analyser).[155]

The basic operation is to create a sine wave $U(t) = U_0 \cos(\omega\tau)$ at a certain frequency, apply it to the sample and measure the resulting response in two analysis channels. The first one measures the resulting voltage, the other one detects via a current-to-voltage converter the current drop. Via the impedance

$$Z^* = Z' + iZ'' = \frac{U_0}{I^*(\omega)}, \tag{3.1}$$

the complex permittivity is obtained, as U_0 and the complex current I^* are known. For a better resolution an additional reference measurement with a reference capacitor is performed, leading to a higher measurement time $(t = 6/\nu)$. To record, e.g., one spectrum from 10^{-4} Hz to 10^{6} Hz 41 hours are needed if four frequencies per decade are measured on a logarithmic time scale. Considering ideal measurement conditions the lower limit for the loss angle δ, with $\tan(\delta) = \varepsilon''/\varepsilon'$ is 10^{-5}.[155]

- ***Autobalance bridge (HP 4284A)***

Between several Hz and 10 MHz autobalance bridges are often used. Figure 3.4 shows a schematic circuit diagram of an autobalance bridge. The sample and a reference impedance are connected in series. The signal from the generator is applied to the sample, a counter voltage is applied to the reference impedance. The counter voltage is generated from the generator signal after passing a modulator that allows an adjustment of voltage and phase. Amplitude and phase of the counter voltage are adjusted until the current through the sample and through the reference impedance are equal but contrariwise. This is done by a zero voltage detector measuring the voltage at the connection point L of both impedances.[1,156] The complex impedance is obtained as

$$Z^* = Z' + iZ'' = U^*_{sample}\frac{R}{U^*_{ref}}\,. \qquad (3.2)$$

R denotes the reference impedance, U^*_{sample} and U^*_{ref} the voltage at the sample and the reference impedance, respectively.

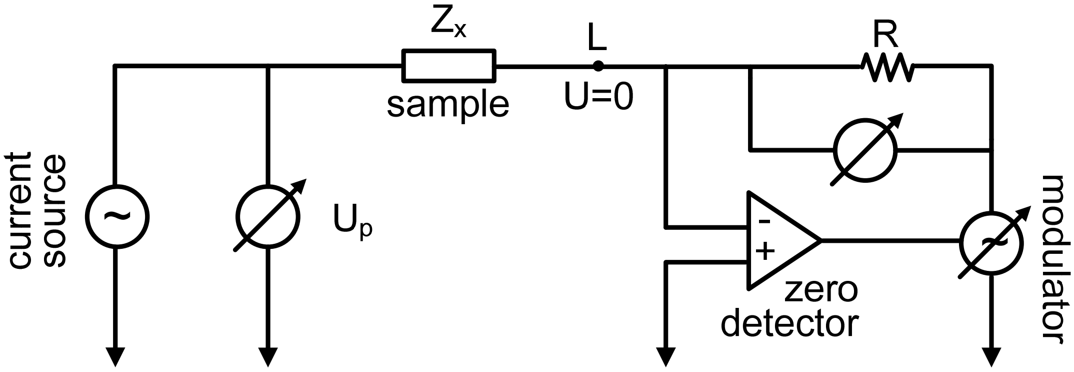

Figure 3.4: Schematic circuit diagram of an autobalance bridge (HP 4284).[156]

3.1.2 Coaxial line techniques

- ***Reflection technique***

The coaxial reflection technique is used in the MHz – 10 GHz range. As shown in figure 3.5, the sample is filled into a brass capacitor bridging the inner and outer conductor at the end of a coaxial line. The design of the sample holder and the coaxial line is crucial for reaching high frequencies. The coaxial line should be as short as possible to minimize its influence on the measuring signal, nevertheless a certain length of the line is necessary to ensure thermal decoupling of sample and measuring port. Furthermore, lines with a minimum of dielectric material between inner and outer conductor are preferable to avoid temperature dependent changes of the line properties. To correct for contributions of connectors and the coaxial line a proper calibration (using three standard impedances, "open", "short" and "load") has to be performed. To enhance measurement resolution, an additional compensation of the sample holder should be carried out.[1,149]

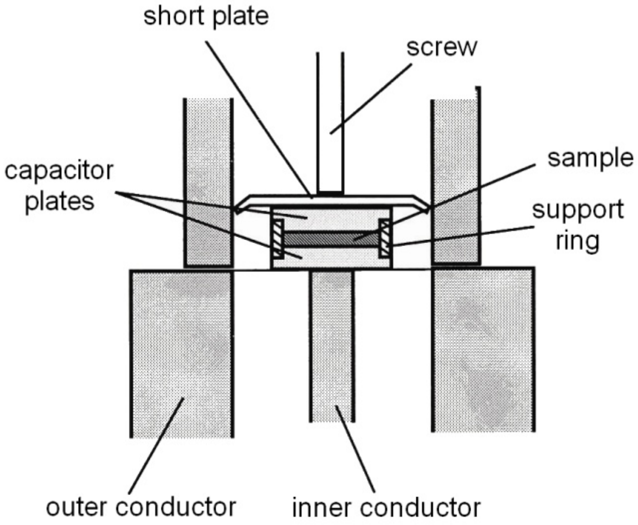

Figure 3.5: Schematic drawing of the sample geometry for reflection measurements of liquids using a parallel plate configuration.[1]

Within this work two different devices, the impedance analyser HP 4291A (1 MHz – 1.8 GHz) and the Agilent 4991 (1 MHz – 3 GHz), were used. A direct current-voltage measurement is performed. The signal applied to the sample and the signal at a reference impedance, connected in series to the sample, are multiplexed and fed into the receiver. This signal is proportional to the current through the sample. The impedance is determined from the ratio of complex voltage and current.[1,157–159]

- ***Transmission technique***

The coaxial transmission technique[160,161] is used to characterize materials up to 40 GHz. The sample material is put into a coaxial line and fills the space between inner and outer conductor. The ends of the line are sealed with thin Teflon discs. As transmission depends exponentially on the dielectric loss of the sample, different temperature regions require the use of various line lengths (from 10 mm to 300 mm) to keep transmission in the resolution window of the network analyser. To ensure homogeneous cooling of the whole line, specially designed nitrogen-cryostats are used. Thermal coupling to the sample can be improved by using brass lines with optimized geometry. A schematic view of the setup is shown in figure 3.6.

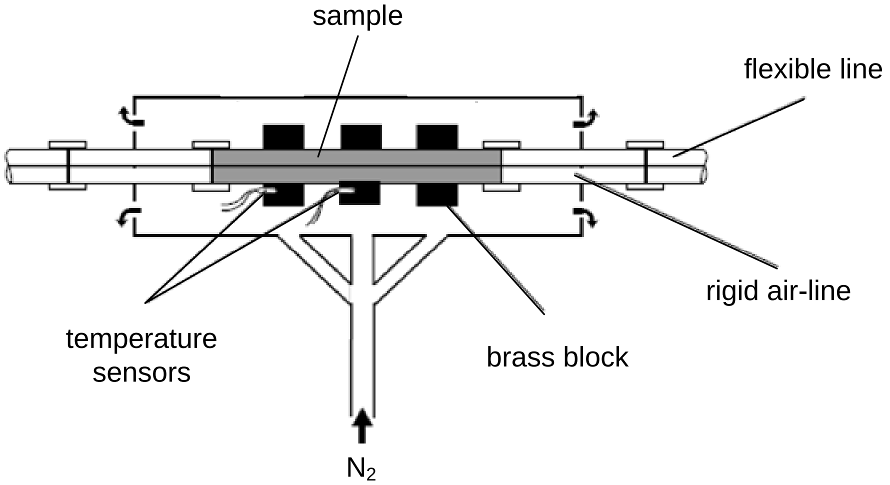

Figure 3.6: Schematic view of the setup used for transmission measurements.[21]

The transmission coefficient is calculated from the measured *s*-parameter values. Mathematically they can be treated by a complex matrix $\hat{S}$, which connects the amplitudes a_n of the incoming with the amplitudes of the out coming ones b_n[162–164]

$$\begin{pmatrix} b_1 \\ b_2 \end{pmatrix} = \begin{pmatrix} S_{11} & S_{21} \\ S_{12} & S_{22} \end{pmatrix} \begin{pmatrix} a_1 \\ a_2 \end{pmatrix} \tag{3.3}$$

Using only source a_1, S_{11} is equivalent to the input complex reflection coefficient, while S_{21} is the forward complex transmission coefficient:

$$S_{11} = \frac{reflected}{incident} = \frac{b_1}{a_1} \quad \text{and} \quad S_{21} = \frac{transmitted}{incident} = \frac{b_2}{a_1} \tag{3.4}$$

For better visualisation the equivalent circuit for the s-parameters is shown in figure 3.7. The knowledge of these magnitudes allows for the calculation of the complex reflection and transmission coefficients Γ^* and T^*, respectively (see Appendix 6.1). To account for multiple reflections a special MathCAD program is used.

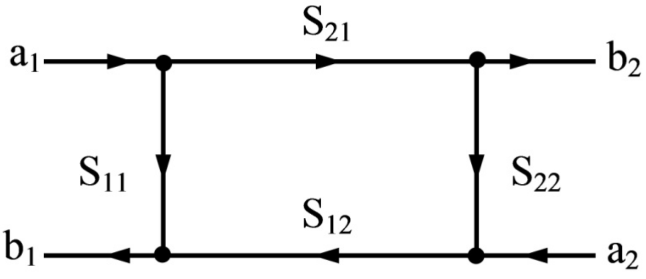

Figure 3.7: S-parameter flow graph notation for a two-port device. The first number represents the output port and the second one the input port ($S_{\text{out in}}$).

3.1.3 *Quasioptical method: submillimeter wave spectroscopy*

For measurements in the submillimeter-region (60 GHz - 1.2 THz) a quasioptical submillimeter spectrometer is used. Its operation mode is based on the principle of a Mach-Zehnder interferometer. Tuneable monochromatic radiation is generated by so-called backward wave oscillators (BWOs).

- ***Backward wave oscillators***

BWOs are miniature electro-vacuum devices. Put in a magnetic field and supplied with high voltage they emit monochromatic electromagnetic radiation. For radiation detection in free space infrared detectors (Golay cell or pumped helium bolometer) are used.

In figure 3.8 a schematic illustration of a BWO is shown. When the heater is switched on, the cathode emits electrons, which are accelerated by a high voltage electrical field and travel towards the anode. The electrons are collimated in a beam by an external magnetic field and fly over a comb-like electrode (slowing system) which intents to transfer the kinetic energy of the electrons to the electromagnetic field. They are grouped periodically by moving in the variable potential of the comb-electrode and form an electromagnetic wave travelling in the opposite direction to the electrons. The radiation leaves the BWO through the waveguide. By changing the strength of the accelerating field, the characteristic frequency range of the BWO can be scanned.

Two different types of BWOs can be distinguished. At low frequencies ($\nu < 180$ GHz) mainly packetized BWOs which have their own magnet are used. Higher frequencies ($\nu > 180$ GHz) require stronger magnetic fields and, for this reason, are produced unpacketized. They have to be mounted into a strong external magnet. Latter are cooled by water whereas former are cooled by air.[153]

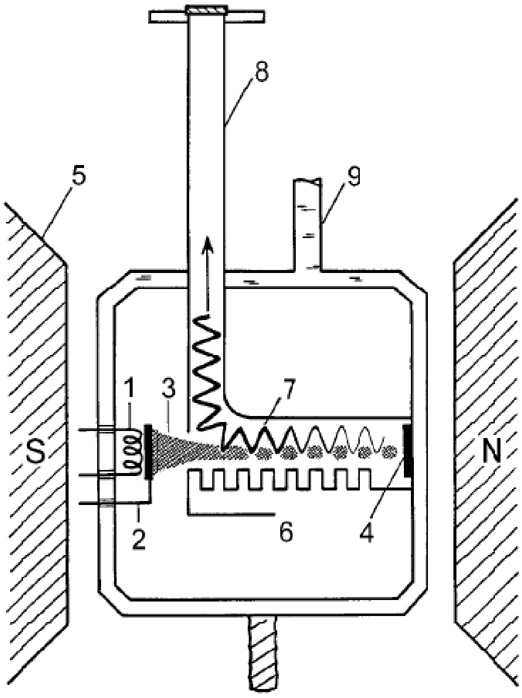

Figure 3.8: Schematic illustration of a backward wave oscillator.[153] The legend is as follows: (1) heater, (2) cathode, (3) electron beam, (4) collector (anode), (5) permanent magnet, (6) slowing system, (7) electromagnetic wave, (8) waveguide and (9) water cooling.

- ***Submillimeter spectrometer***

The spectrometer follows a Mach-Zehnder setup and allows for direct measurement (no Kramers-Kronig analysis required) of the transmission coefficient T and phase shift ϕ of the radiation passing the sample. For the determination of the phase shift both arms of the spectrometer are used. The radiation produced by the BWO leaves the source as a divergent beam that is collimated into a plane-parallel beam with a Teflon lens. The beam splitter produces two polarized beams, one for each arm of the spectrometer. Grey arrows in figure 3.9 indicate the polarization of the E-vector of the radiation in each arm. In arm I, the beam is focussed on the sample by two Teflon lenses, while arm II serves as reference, and is used for determination of the change of the optical path-length. Both beams recombine at grid 2 and interfere. The result of interference is recorded by the detector. The absolute value of the phase shift is calculated by means of the positions of the moving mirror 1 and the static mirror 2. This is done software-controlled at every fixed frequency of the spectra. To eliminate the radiation characteristics of the BWO an additional reference measurement without sample has to be performed.

For the measurement of the transmission coefficient arm II is blocked with an absorber. Two measurements are performed, one with sample and one without sample as reference. The ratio of the intensities, $T = I_{sample}/I_{reference}$, gives the absolute transmission measurements. To improve the signal-to-noise ratio a chopper is used for the transmission and a modulator at mirror 2 for the phase measurement.

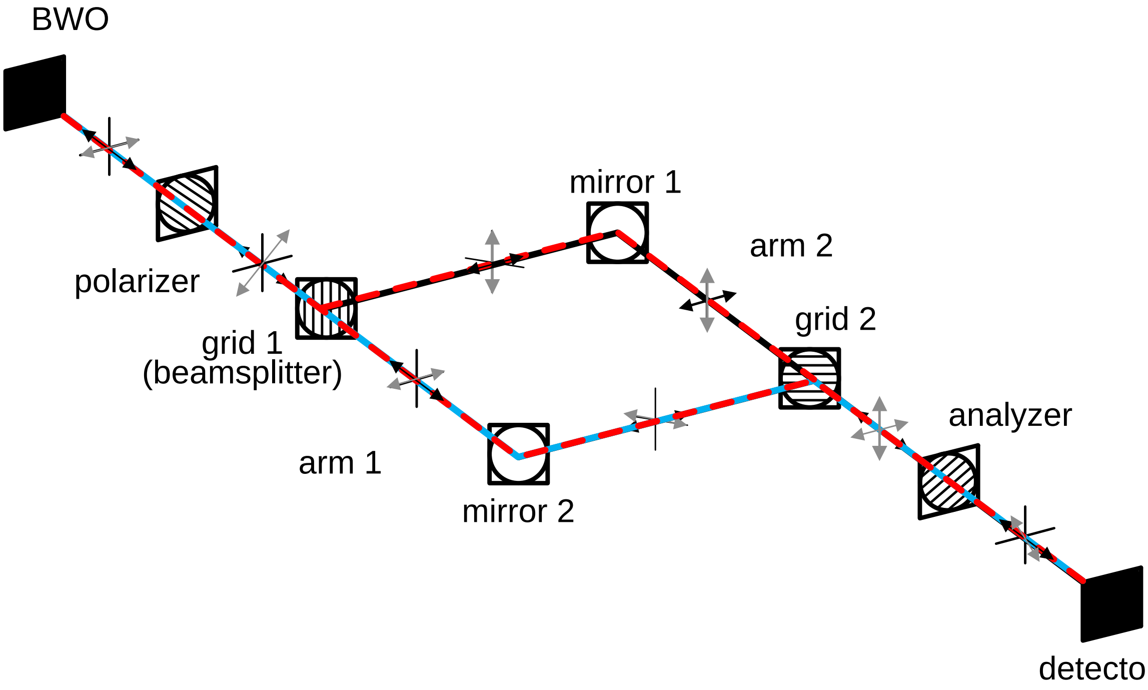

Figure 3.9: Quasioptical submillimeter spectrometer. Dashed lines (arm 1 is coloured in blue and red, arm 2 in black and red) and arrows show the propagation direction of the beam, grey arrows indicate the E-vector of the radiation.[165]

- ***Calculation of ε' and ε''***

Any (non-magnetic) material is characterized by two independent optical parameters. From transmission T and phase ϕ refraction and extinction coefficients n and k can directly be calculated. They are connected via the Fresnel expressions (see, e.g., Refs. 151 and 166) for complex transmission of a plane-parallel layer by:

$$T = e^{-\frac{4\pi kd}{\lambda}} \cdot \frac{(1-R)^2 + 4Rsin^2\psi}{\left(1 - R \cdot e^{-\frac{4\pi kd}{\lambda}}\right)^2 + 4R \cdot e^{-\frac{4\pi kd}{\lambda}} \sin^2\left(\frac{2\pi nd}{\lambda} + \psi\right)} \tag{3.5}$$

$$\begin{aligned} \phi = \frac{2\pi nd}{\lambda} - arctan\frac{k(n^2+k^2-1)}{(k^2+n^2)(2+n)n} \\ + arctan\frac{R \cdot e^{-\frac{4\pi kd}{\lambda}} \sin^2\left(\frac{2\pi nd}{\lambda} + \psi\right)}{1 - R \cdot e^{-\frac{4\pi kd}{\lambda}} \cos^2\left(\frac{2\pi nd}{\lambda} + \psi\right)} \end{aligned} \tag{3.6}$$

R and ψ correspond to the absolute value and the phase of the complex reflection.

$$R = \frac{(n-1)^2+k^2}{(n+1)^2+k^2}, \quad \text{and} \quad \psi = \arctan\left(\frac{2k}{n^2+k^2-1}\right) \tag{3.7}$$

So, R and ψ are just functions of the wavelength, the sample thickness and the complex refraction index n^*. As n and k are directly connected with ε^* via:

$$n^* = n + ik = \sqrt{\varepsilon^*}, \tag{3.8}$$

real and imaginary parts are easily obtained:

$$\varepsilon' = n^2 - k^2 \tag{3.9}$$

$$\varepsilon'' = 2nk \tag{3.10}$$

The intensity of the radiation that passes through the sample is attenuated according to:

$$T =\cdot e^{-\frac{4\pi k}{\lambda}d} \tag{3.11}$$

In addition to the damping of the radiation, a rotation of the phase takes place, depending on the thickness of the sample.

$$\beta = \frac{2\pi n d}{\lambda_0} \tag{3.12}$$

Here, λ_0 is the vacuum-wavelength. To account for multilayer interferences caused by the contributions of the windows of the sample cell, it is necessary to know the optical parameters of the window glass precisely. The spectrum of the empty cell has to be recorded before filling it with sample material to obtain the parameters of each layer (glass + air + glass). The software used at the submillimeter spectrometer allows for numerical calculation of the above presented system of equations, so that the frequency dependent magnitudes n, k, ε', and ε'' are directly obtained.

3.1.4 Fourier transform infrared spectroscopy (FTIR)

In the frequency region above 100 GHz, commercially available infrared spectrometers are used. For the measurements the Fourier-transform spectrometer *Bruker IFS 113v* was employed. By the use of various lamps and detectors a total frequency range of

400 GHz ≤ ν ≤ 360 THz can be covered. In contrast to submillimeter-wave spectroscopy it is only possible to measure the transmission or reflection of the sample but not to determine the phase shift caused by the sample. For this reason a Kramers-Kronig transformation has to be performed to deduce the complex dielectric permittivity from the transmission (or reflection) measurement. However, just as in submillimeter-wave spectroscopy, data analysis has to consider optical multilayer interferences taking into account the known optical parameters of windows of the sample cell.[1,167]

3.2 Neutron scattering

At this point only a very short introduction into neutron scattering is given. Neutron scattering is a very sophisticated technique and it is beyond the scope of this work to explain it in detail. The interested reader is referred to the vast literature. A good overview is given in Refs. 168 and 169.

Generally scattering methods provide information on the structure and the dynamics of matter. There are many different kinds of scattering methods, each one suited for particular questions of interest. Neutron spectroscopy allows for the investigation of motion of atoms and molecules on a microscopic scale of 0.2 Å – 200 Å and on time scales of 0.1 ps –1 μs. If magnetic scattering processes are not taken into account, neutrons are, in contrast to X-ray diffraction, not scattered at the electronic shell of the atom but at its nucleus. Nuclei have a diameter in the range of 10^{-15}m, much smaller then the wavelength of cold/thermal neutrons (~10^{-10}m) and can therefore be considered as punctiform. This means, that shape or internal structure of the nuclei do not influence the scattering experiment and only the arrangement and movement of the nuclei is observed.

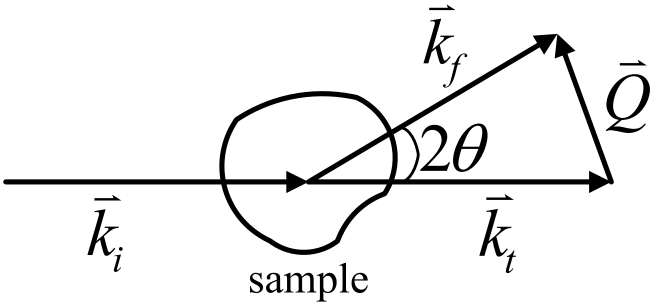

Figure 3.10: Schematic representation of a scattering experiment. $\vec{k}_{i,f,t}$ represent wavevectors of the incoming, scattered and transmitted neutron, respectively. $\vec{Q}$ represents the scattering vector.

From the measured intensity, two basic quantities, the scattering vector $\vec{Q}$ and the energy transfer $\hbar\omega = E_f - E_i = \Delta E$, can be determined. The wave vector transfer is defined as

$Q = \vec{k}_f - \vec{k}_i$, as shown schematically in figure 3.10. Information on the spatial arrangement of the nuclei can be obtained from the intensity of the elastic scattering as a function of Q (the diffractogram), whereas the scattering intensity at a certain Q -value as function of the energy (the spectrum) gives information on the motion of the nuclei.[168,169] With this information, the scattering function $S(Q,\omega)$ is obtained, which is proportional to the susceptibility χ''. A detailed explanation is given in Ref. 169.

3.2.1 *The high-resolution time-of-flight spectrometer TOFTOF*

Neutron scattering experiments were performed at the TOFTOF spectrometer at the research neutron source Heinz Maier-Leibnitz (FRM II) in Garching. This spectrometer is a multidisc chopper time-of-flight spectrometer for cold neutrons.[170] A schematic illustration is shown in figure 3.11. The TOFTOF has one order removal chopper more and operates with cold neutrons. They are guided through an s-shaped neutron guide to the primary spectro-meter. There, seven high-speed neutron chopper discs are used to select short mono-chromatic neutron pulses from the continuous neutron beam. The different kinds of choppers are used to produce short polychromatic neutron pulses (1st pair), two choppers are used to suppress transmission of neutrons with higher order wavelength and one single chopper is used to decrease the overlap of successive pulses (frame overlap). The 2nd chopper pair is used as a counter rotating monochromating chopper. The neutron pulses hit the sample in the cryostat that is attached to the primary spectrometer (figure 3.11). The time-of-flight of the neutrons from the sample to the detector is measured and from $N(2\theta, tof)$ the neutron spectra $S(Q,\omega)$ are calculated. For details see Ref. 170.

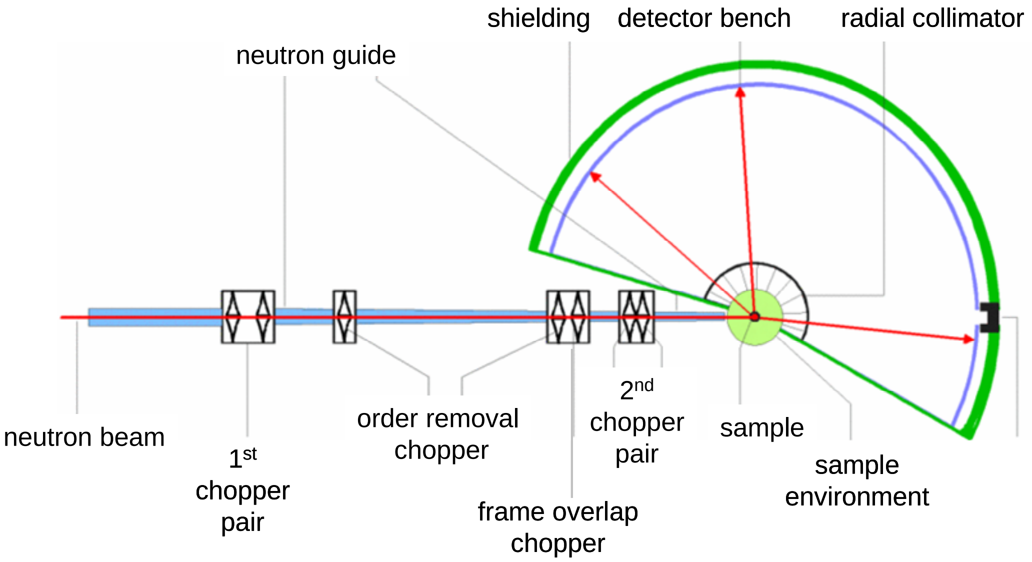

Figure 3.11: Schematic illustration of a time-of-flight spectrometer. The TOFTOF has one additional order removal chopper. The illustration is taken from the FRM II homepage.

In addition to the measurements of the samples (here 0%, 0.5%, 4% 10% and 20% LiCl in glycerol) measurements of background and a vanadium standard have to be performed.
The raw data is analysed with the help of the FRIDA[III] program.

3.3 Positron annihilation lifetime spectroscopy (PALS)

Positron annihilation lifetime spectroscopy (PALS) experiments were performed at the SAS-Polymer Institute in Bratislava. Positrons are generated during the radioactive decay of certain elements. One of the most utilized is $^{22}_{11}Na$, which decays under simultaneous emission of e^+ and a γ-photon of 1.28 MeV to $^{22}_{10}Ne$. In dielectric, amorphous materials a part of the positrons is formed to a bound state of a positron and an electron. This state is called positronium (Ps) and can exist in two ground states depending on the mutual spin orientation of the $e^- - e^+$ pair. The positron and the positronium both annihilate by emitting γ-rays (see figure 3.12 for details). As the para-positronium (singlet state) has a very short self-annihilation time of τ_1 = 0.125 ns, it is not used for measurements. However, the ortho-positronium (triplet spin state) has a relatively long intrinsic lifetime of τ_3 = 142 ns, and therefore is an adequate measure for free volume.[171,172]

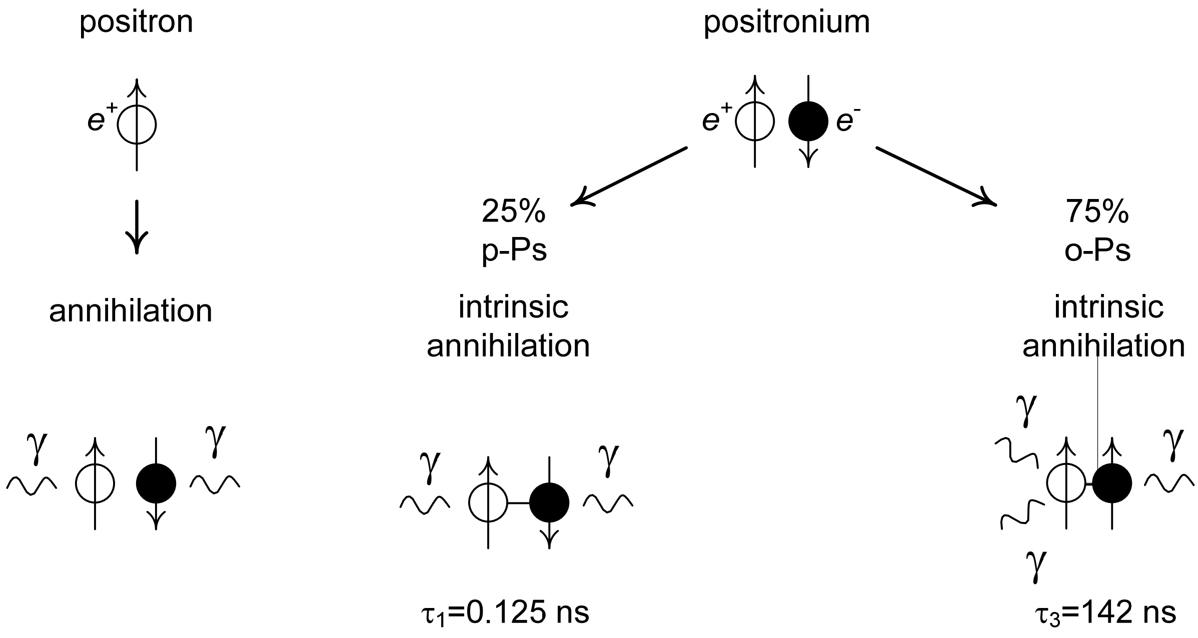

Figure 3.12: Simplified schematic illustration[173] of the different annihilation possibilities of positron and positronium. Positrons are shown as filled circles, electrons as open circles.

[III] FRIDA (Fast Reliable Interactive Data Analysis) is software for scientific data analysis. It is based on Joachim Wuttke's IDA, which has been used since the early 1990s at important neutron research centers. The current relaunch is a joint effort of scientists from different institutes.

During the measurement, the lifetime of the positron in the sample (time between injection and annihilation) is determined. ${}^{22}_{11}Na$ emits almost simultaneously a positron and γ-photons (1.28 MeV). By the detection of the created photon at the first detector and the detection of an annihilation γ-photon (0.51 MeV) at the second detector, connected in parallel, the lifetime is determined by the difference between the two detector signals. In an homogeneous environment all positrons have the same annihilation probability, leading to one single exponential in the lifetime spectrum. However, in a heterogeneous material, the positrons have different environments and create different positron states after slowing down. Therefore, the presence of positrons/positronia leads to different populations of the positron state. The positron lifetime spectrum is composed of a sum of several exponentially decaying components with characteristic lifetime values. For data analysis usually the o-Ps lifetime τ_3 is plotted versus the temperature T.[172]

3.4 Overview on the methods: advantages and disadvantages

- **Dielectric spectroscopy**

Dielectric spectroscopy covers a range of up to 21 decades in frequency. A combination of different experimental techniques allows to determine the dielectric response in a very broad frequency and temperature (1.5 - 1500 K) range. While the range from 10^{-6} Hz to 10^{9} Hz is relative easy to access, especially measurements in the submillimeter region are rather sophisticated, difficult to perform and time-consuming. For infrared measurements, the investigated liquid samples have to be prepared in very thin layers (~µm). In contrast to the quasi-optical measurements no phase shift is measured, and for calculating the dielectric loss, a Kramers-Kronig transformation has to be performed.

The main advantage of dielectric spectroscopy is the excellent energy resolution but only materials with a dipole moment are suited for this method, and it is not possible to obtain momentum resolution.

- **Neutron scattering**

Neutron scattering is an important tool to study the fundamental properties of condensed matter. As the neutron is electrical neutral, this technique offers the possibility to gain information on static, dynamic and magnetic properties that cannot be obtained by other techniques like X-ray scattering or using synchrotron radiation.[174,175] In the present work, we are only interested in quasielastic neutron scattering to probe the dynamics of the molecular glass formers. In contrast to dielectric spectroscopy not the dipolar reorientation is probed but density fluctuations. Only measurements at the TOFTOF-spectrometer were performed.

Here, the number of detected neutrons and their time-of-flight, $N(2\Theta, t)$, to the detector is measured. From this information, the q-dependent neutron spectra $S(Q, \omega)$ are calculated. However, to extend the frequency range, it would be necessary to carry out measurements at other instruments, e.g., backscattering experiments at the SPHERES spectrometer at the FRM II.

- **Positron Annihilation Lifetime spectroscopy**

Positron annihilation lifetime spectroscopy[176] is based on the annihilation behaviour of the ortho-positronium (o-Ps) in condensed matter. The technique is very sensitive to regions of low electron density and vacancies in crystals or free volume holes, defects and voids in amorphous materials.[172] PALS has been considered as a very complex, indirect way to investigate condensed matter, but the combination of PALS studies with other spectroscopic methods allowed in many cases to solve the question of defect identification.[177] In this work the link to dielectric spectroscopy is established, and the aim is to get a deeper understanding of the glassy dynamics by comparing both methods.

4 Results and discussion

4.1 Broadband dielectric spectra of glass-forming liquids

This chapter is composed of four main parts. In the first one, the dielectric spectra of typical molecular glass formers, Salol, xylitol and benzophenone are discussed. Afterwards systematic studies on a series of propylene glycols and on the binary system glycerol with varying LiCl content are presented. In the end, the concept of fragility and its connection to the boson peak is discussed on the basis of the results presented in the beginning of this chapter.

4.1.1 Salol and xylitol – discussion of a "Type A" and "Type B" system

Figures 4.1 (a) and (b) provide broadband dielectric loss spectra of two typical glass-forming liquids, xylitol ($C_5H_{12}O_5$, $T_g \approx 248$ K) and Salol ($C_{13}H_{10}O_3$, $T_g \approx 218$ K) at various temperatures. For the present work, the data in submillimeter region has been measured in addition to the available low-frequency data. Both materials are representative examples for small molecular organic glass-formers with a relatively high dipole moment. While in Salol an excess wing is observed at frequencies beyond the α-relaxation (type A), xylitol shows additional secondary peaks at low and shoulders, revealing the presence of a β-relaxation peak, at higher temperatures (type B).[23]

- ***The α-relaxation***

The dominating feature in the dielectric loss spectra of xylitol and Salol, as shown in figures 4.1 (a) and (b) is the α-relaxation peak, which directly mirrors the slow down of the molecular dynamics. The continuous freezing from the low viscosity liquid to the solid glass is characterized by a tremendous frequency shift from the GHz to mHz range, while the temperature changes only by about a factor of two. The α-peaks are asymmetrically shaped and broader than expected for the Debye case. In the double logarithmic representation of figure 4.1, the low- and high-frequency flanks of the α-relaxation peaks are linear and can be described by two power laws. The exponent of the low-frequency power law is close to one, the high-frequency exponent is increasing with temperature. For data description, usually the phenomenological CD formula, equation (2.4) with $\alpha = 0$, or the Fourier transform of the KWW function, cf. equation (2.5), are applied. Indeed, the sum of a CD/HN function accounting for the α-relaxation and a CC function for additional contributions at higher frequencies, overall provide a good data parameterization. The fits are shown by the lines in figure 4.1. To account for a slight broadening of the low-frequency flank of the α-peak, the more general HN function was used for xylitol above 300 K and for Salol below 263 K.

In figures 4.2 (a) and (c), the width parameter β_{HN}, for fits with the CD function, and $\beta_{HN}(1-\alpha_{HN})$ for fits with the HN function is shown. The quantity $-\beta_{HN}(1-\alpha_{HN})$ is best suited to compare the parameters from fits with both functions, as long as α_{HN} is small. The width parameter is increasing with temperature to 0.7 for xylitol and shows saturation about 0.8 for Salol. The deviation from unity denotes the non-exponentiality of glassy dynamics, which is explained by a distribution of relaxation times, caused by the disorder in the glassy material.[92,93]

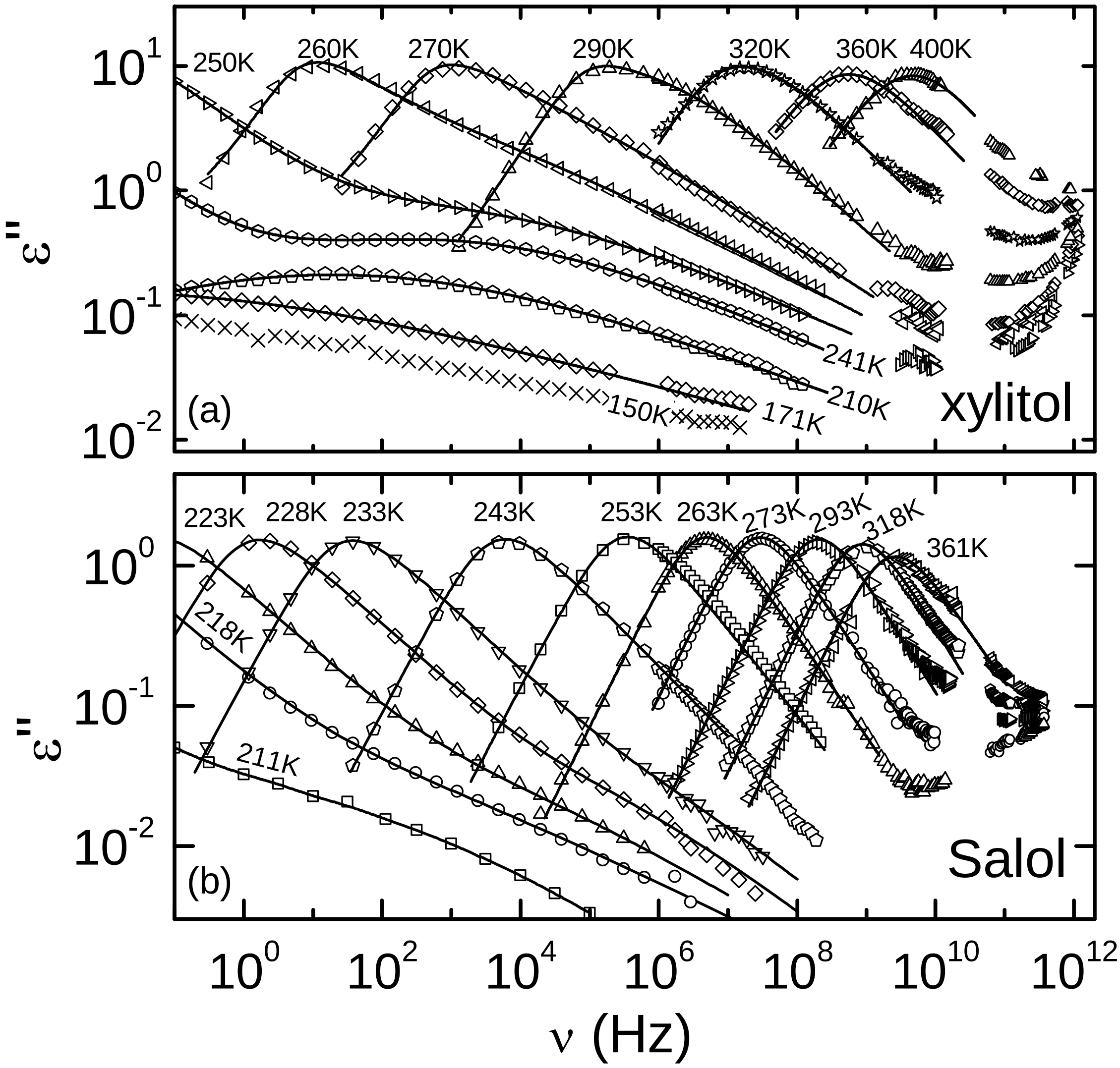

Figure 4.1: Broadband dielectric loss spectra of xylitol (a) and Salol (b) for various temperatures. The solid lines are fits with the sum of a CD and a CC function for α- and β-relaxation, respectively. In (a), above 300 K and in (b) up to 258 K, a HN function had to be used instead of a CD function. The frequency-dependent spectra of Salol are partly published in Ref. 34 and those of xylitol up to 10^{10} Hz in Ref. 25. For the present work, the data in submillimeter region has been measured.

In figures 4.2 (b) and (d), the temperature dependent relaxation strengths for xylitol and Salol are displayed. For glassy matter, Curie behaviour, $\Delta\varepsilon(T)\sim 1/T$, is expected. However, the temperature dependent relaxation strength of Salol is characterized by a

Curie-Weiss law, $\Delta\varepsilon(T) \sim 1/(T - T_{CW})$, with T_{CW} = 90 K, as indicated by the solid line in figure 4.2 (d). This behaviour may be caused by cooperative relaxation processes. The relaxation strength of xylitol, figure 4.2 (b), does not show any distinct tendency in its temperature dependence.

The most important parameter obtained from the fits of the dielectric loss spectra is the relaxation time. The average α-relaxation times $\langle\tau_\alpha\rangle$ for Salol and xylitol are shown in figure 4.3.[17,25,34,154,178] For both, clear deviations from the thermally activated Arrhenius behaviour are observed. For xylitol, the phenomenological VFT-law, equation (2.7), provides a good fit of the experimental data,[25] while for Salol two different VFT fits are needed for data parameterisation.[88,89,154] One for low and one for high temperatures. The closed symbols for the α-relaxation time were obtained from aging experiments[25,154,178] and in both cases give a reasonable extension of the $\tau_\alpha(T)$ curves from equilibrium measurements. For xylitol, the relaxation time at 241 K (4.15 K^{-1}) does not match the fit curve, as this point was obtained from a non-equilibrium measurement (T_g = 248 K).

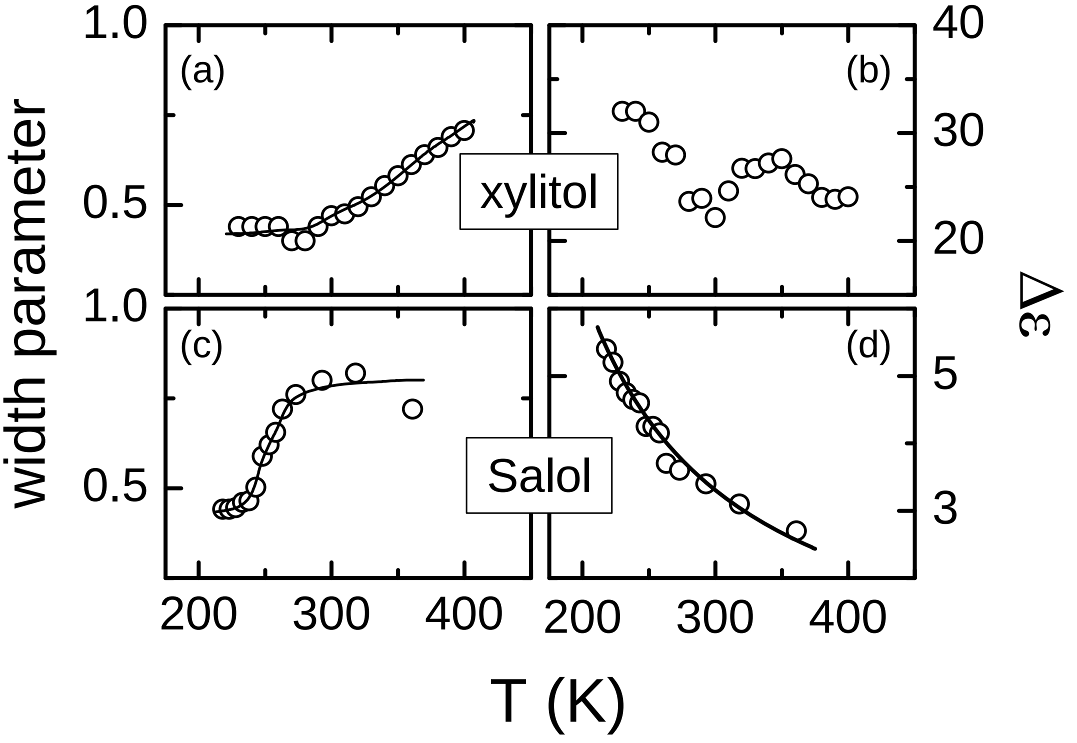

Figure 4.2: Width parameters and relaxation strengths of the α-process of xylitol as obtained from fits of the dielectric loss spectra. The width parameter is given by β_{CD} for the fits with the CD function and by $\beta_{HN}(1-\alpha_{HN})$ for fits with the HN function. Lines in (a) and (c) are drawn to guide the eyes. The line in (d) is a fit using the Curie-Weiss law. The corresponding Curie-Weiss temperature is 90 K.

- ***The excess wing and the (slow) β-relaxation***

At frequencies beyond the α-relaxation, a second but weaker power law, $\varepsilon''{\sim}\nu^{-b}$, the so-called excess wing with $b < \beta$ shows up in Salol, figure 4.1 (b). It is best seen at low temperatures as its slope increases with increasing temperature. At high temperatures (~ 253 K), it merges with the high-frequency flank of the α-relaxation. The curve at 211 K (squares) was obtained after an aging time of 6.5 days.[34] Instead of the excess wing, a well developed shoulder emerges, which is indicative of a β-relaxation peak. It is known, that aging affects α- and β-relaxation times in a different way. As the primary process is influenced stronger by aging, its peak frequency shifts faster to lower frequencies than for the β-peak. This leads to a separation of both peaks.[178]

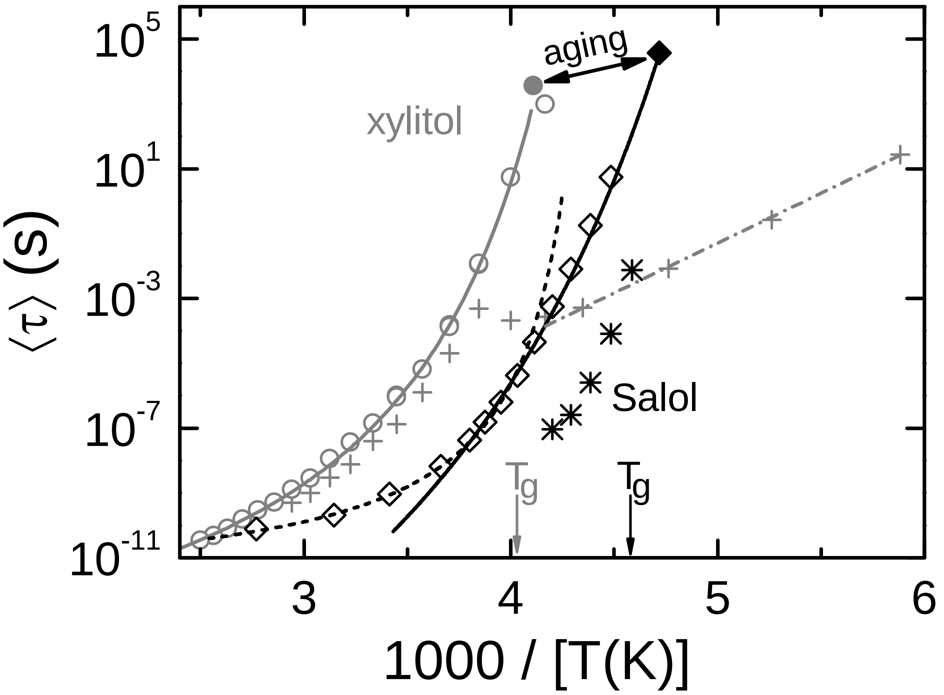

Figure 4.3: Temperature dependent average relaxation times τ_α (open symbols) and τ_β of xylitol (plusses) and Salol (stars) in Arrhenius representation.[17,25,34,154,178] The closed symbols for the α-relaxation were obtained from long-time aging experiments.[25,154,178] The α-relaxation times were fitted with one VFT law for xylitol and two VFT laws for Salol.[25,154] The dash-dotted line demonstrates Arrhenius behaviour of $\tau_\beta(T)$ in xylitol at low temperatures. An energy barrier of 0.61 eV was determined from the slope.

Instead of an excess wing, in xylitol a well-developed secondary β-relaxation peak shows up. Comparing the dielectric spectra of figures 4.1 (a) and (b), it is obvious that below and close to T_g, a larger separation of α- and β-timescales arises. This is already evident, when looking at the temperature dependence of the β-relaxation times in figure 4.3. Here, the β-relaxation times for Salol exhibit a temperature dependence, parallel to that of the α-relaxation times while in xylitol an Arrhenius behaviour is observed to low temperatures.

From the slope of the dashed line in figure 4.3, an energy barrier of 0.61 eV is determined. At temperatures around T_g a minimum shows up in $\tau_\beta(T)$. Such kind of minimum was previously observed in other glass formers[81,82,179,180] and is explained by different models.[82,180]

- ***The fast β-process***

Figure 4.4 shows the minimum region of the dielectric loss of xylitol (a) and Salol (b) in more detail than in figure 4.1. The great interest in this region was mainly triggered by MCT,[11–14,125] but for a model-free check of the excess intensity the insets show fits (dashed lines) with a sum of two power laws.

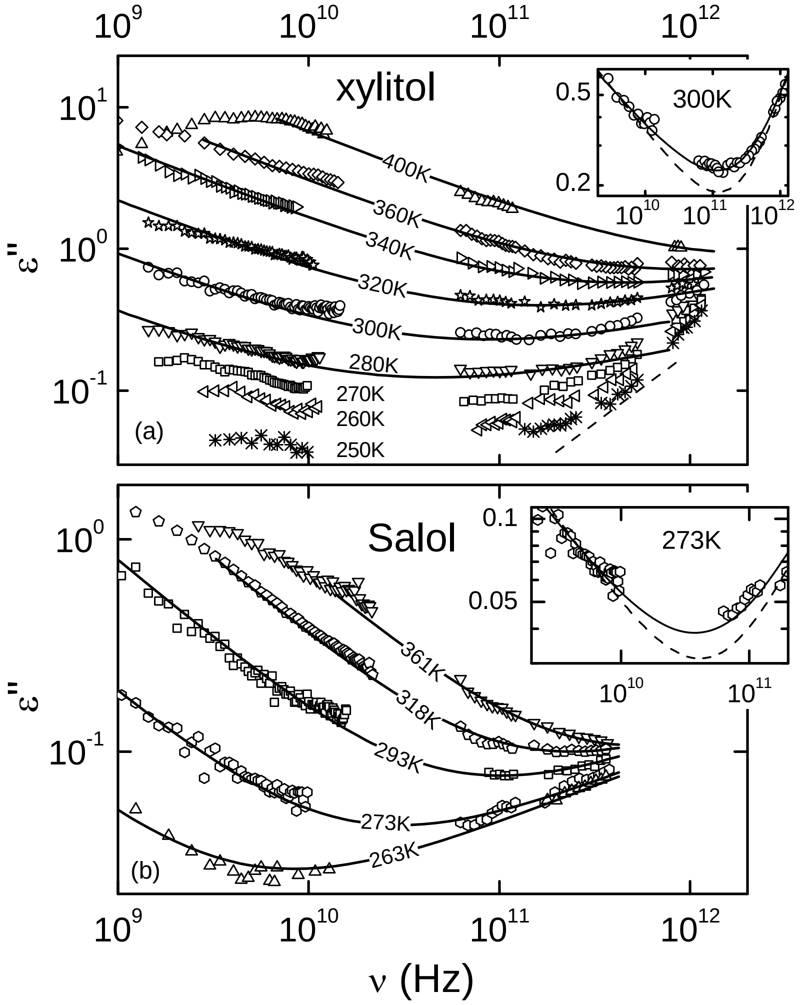

Figure 4.4: Dielectric loss spectra of (a) xylitol and (b) Salol in the high frequency range. The solid lines are fits of the minimum region with idealized MCT, using equation (2.20) with identical parameters a and b for all temperatures. The dashed line in both insets is a fit with the sum of two power laws, each accounting for one flank of the minimum to prove the existence of excess intensity. The solid line in both insets accounts for an additional constant loss contribution.

As the increase towards the boson peak should be steeper than linear,[54,112] the high-frequency power law should have an exponent of at least one. This clearly shows, that this ansatz is not sufficient for data description, but gives evidence for excess intensity in the minimum region. Assuming an additional constant loss contribution[55,114-116] using two power laws with $b < 1$ and $n \geq 1$, one arrives at:

$$\varepsilon'' = c_b \nu^{-b} + \varepsilon_c + c_n \nu^n \tag{4.1}$$

As shown by the solid lines in the insets, the minimum region can be reasonably well described by this equation. This is in accord with the results found in other glass-forming liquids.[35,51,52,113] One possible explanation for the constant loss contribution is given by the extended coupling model.[55]

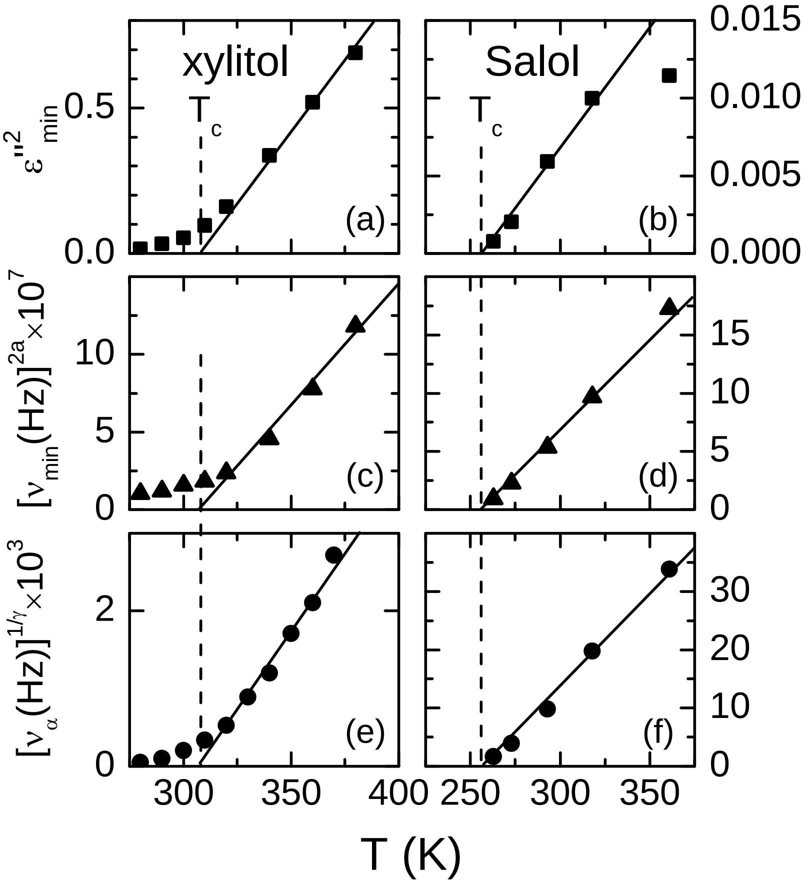

Figure 4.5: Temperature dependence of the minimum amplitude ε_{min} (a), (b) and position ν_{min} (c), (d) and of the α-relaxation rate ν_α (e), (f) of xylitol and Salol. ε_{min} and ν_{min} were obtained by fits with equation (2.20). According to the predictions of MCT, representations have been chosen that should result in linear behaviour. The solid lines demonstrate a consistent description of all three quantities with a T_c of 308 K for xylitol and 256 K for Salol.

In figure 4.5, the temperature dependence of ε_{min}, ν_{min} and ν_{α} are shown for both glass formers. The representations have been chosen in such way, that the critical laws, equations (2.25), (2.26) and (2.23), are linearised and therefore should lead to straight lines extrapolating to T_c. The solid lines demonstrate a consistent description of all three quantities with a T_c of 308 K for xylitol and 256 K for Salol. Especially for xylitol, data partly deviate from linear behaviour near T_c. Within MCT, this can be ascribed to a smearing out of the critical behaviour due to hopping processes. These correspond to the escape of the caged particle, and are considered in extended versions of MCT only.[14,181] The exponent parameters a and b of the von Schweidler (ν^{-b}) and critical (ν^{a}) law are related via the so-called system parameter λ, equation (2.22). They are material specific and independent of temperature. a and b were determined to 0.297 and 0.53 ($\lambda \approx 0.76$) for xylitol and to 0.352 and 0.75 ($\lambda \approx 0.63$) for Salol, respectively.

4.1.2 The structural glass-former benzophenone

- ***The α- and slow β-relaxation***

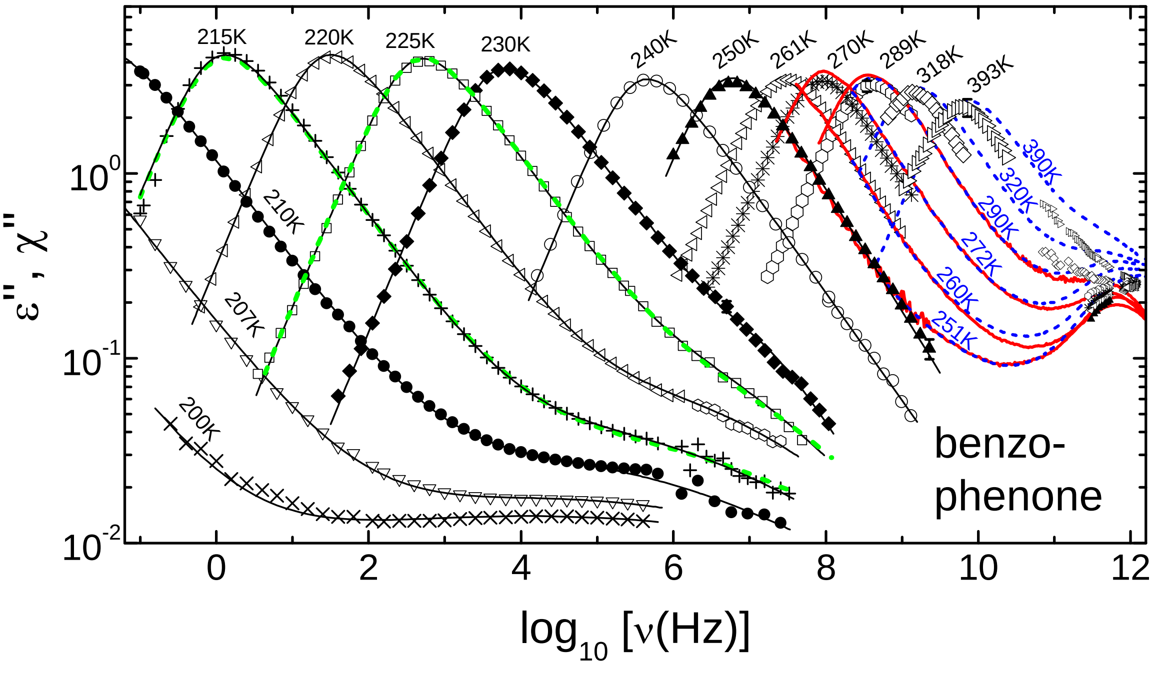

Figure 4.6: Frequency dependent dielectric loss of BZP for various temperatures.[50] The solid lines are fits with the sum of a CD and CC function. At $T > 230$ K the CC amplitudes were set to zero. The green dashed lines represent fits for 215 K and 225 K performed with the convolution ansatz as promoted in Ref. 124. Blue dashed and red solid lines show the imaginary part of the susceptibility data obtained from OKE[128] and DLS[182] measurements. To match the dielectric data at 250 K, the susceptibility data were vertically scaled with a single factor for all temperatures. For the present work, dielectric measurements in the submillimeter region have been performed.

Figure 4.6 shows the frequency dependent dielectric loss of the molecular glass-former benzophenone (BZP) together with the susceptibility spectra from optical Kerr effect (OKE)[128] and dynamic light scattering (DLS)[182] experiments for various temperatures. The dielectric data is partly published in Refs. 50 and 131. For the present work, the measurements in the submillimeter range have been performed. The dielectric spectra are dominated by the α-relaxation peaks, strongly shifting to higher frequencies with increasing temperature. In addition, an excess wing ($T \geq 220$ K) and a β-relaxation ($T \leq 215$ K) are observed. For data parameterisation, fits with the sum of a CD and CC function were carried out, to describe the α- and β-relaxation (or the excess wing), respectively.[50] Above 230 K only a single CD function was used. The fits are shown as solid black lines.

Figure 4.7 shows the width parameter β_{CD} (a) and the relaxation strength $\Delta\varepsilon$ (b) of the α-process as obtained from the fits.[50] β_{CD} increases with increasing temperature and tends to saturate at a value below unity. This signifies non-Debye behaviour, usually explained by a distribution of relaxation times.[92,93] The saturation of β_{CD} is reached at a temperature somewhat higher than the reported values of T_c (250 K[129] and 235 K[127]). MCT predicts that the time-temperature superposition principle for $T > T_c$ should be obeyed and that for these temperatures the α-relaxation should be non-exponential, implying a temperature independent width parameter. The relaxation strength increases with decreasing temperature. As in Salol, $\Delta\varepsilon(T)$ is parameterized by a Curie-Weiss-law, $\Delta\varepsilon \sim 1/(T - T_{cw})$, with T_{CW} = 107 K, pointing to cooperative relaxation processes.

α- and β- relaxation times (full and open circles) as obtained from the fits are shown in an Arrhenius representation in figure 4.8. The α-relaxation times show clear deviations from thermally activated Arrhenius behaviour and are fitted with the commonly used VFT law, equation (2.7). The fit parameters are $\tau_0 = 4.2 \cdot 10^{-13}$s, $T_{VF} = 189$ K and $D = 3.8$. However, the VFT function does not provide a perfect fit, and clear deviations show up for high and low temperatures. At low temperatures they are due to the fact that the sample is not in thermal equilibrium at $T < T_g$. Deviations at high temperatures are also observed in other glass-formers if the covered temperature and frequency range is broad enough.[88] The β-relaxation times show Arrhenius-like behaviour below the glass transition temperature. The dash dotted line in figure 4.8 is a fit of the β-relaxation times for $T < T_g$, assuming an Arrhenius law (τ_0=$8.8 \cdot 10^{-15}$ s, E = 0.36 eV). In the glassy state, this behaviour commonly is found for α- and β-relaxations.[23,28,81,183,184] Above T_g, the β-relaxation times are in the same range as theoretically predicted by the coupling model. For comparison, the primitive relaxation times of the CM, calculated by equation (2.14), are shown as crosses. Above T_g they are in good accord with τ_β, as determined from the fits.

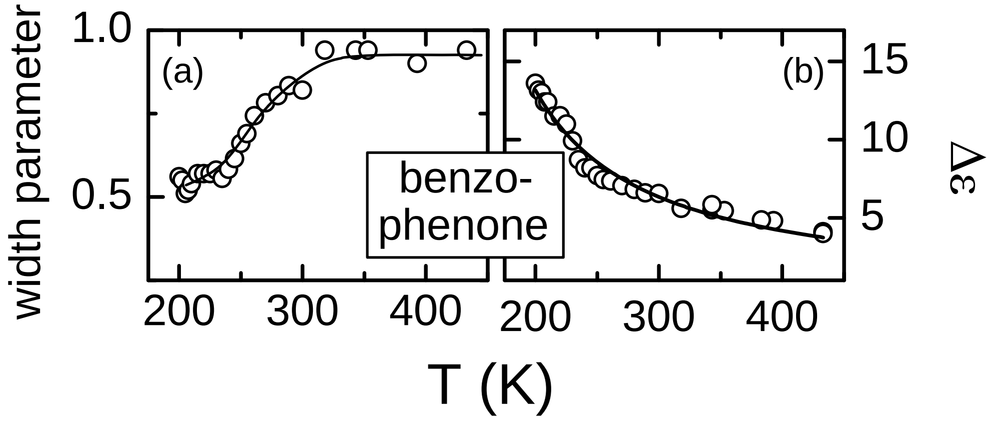

Figure 4.7: Width parameter β_{CD} and relaxation strength $\Delta\varepsilon$ of the α-process as obtained from fits of the dielectric loss spectra.[50] The line in (a) is drawn to guide the eyes; in (b) a fit using the Curie-Weiss law is shown. The corresponding Curie-Weiss temperature is 107 K.

However, one should mention, that in literature the use of a simple additive superposition is highly debated. Another alternative is the convolution approach promoted in Ref. 124, based on the product ansatz by Williams.[185,186] In Ref. 50, we applied the convolution approach exemplarily for 215 K and 225 K. The fits are shown as dashed green lines in figure 4.6. These fits, using the same α- and β-relaxation times, are of equal quality as the ones for the additive ansatz. However, no physical reason exists for favouring one fitting procedure over the other.

- ***The high-frequency response***

As an example, the high-frequency response of BZP as obtained by different measurement techniques is shown in figure 4.6.[50] Blue dotted lines show the imaginary part of the susceptibility from optical Kerr effect (OKE) measurements,[129] while red lines show dynamic light scattering (DLS)[182] data. To match the dielectric data at 250 K, the susceptibility was vertically scaled with a single factor for all temperatures. The α-peak positions seem to be in rather good agreement. This is also seen in figure 4.8, which reveals that the relaxation times from all three methods are close together. They are shown as open squares and crosses (×) regarding OKE[129] and DLS[182] data, while relaxation times from dielectric measurements[131] are shown as full circles. In the case of BZP, only at high temperatures small deviations of the DLS from the dielectric data show up. This may be due to imperfect thermal coupling or the different methods of determining the relaxation times. Because of different coupling to translational and reorientational degrees of freedom and different tensorial properties[187,188] of both methods, the relaxation times of light scattering experiments usually are smaller as known from earlier comparisons.[3,187–191]

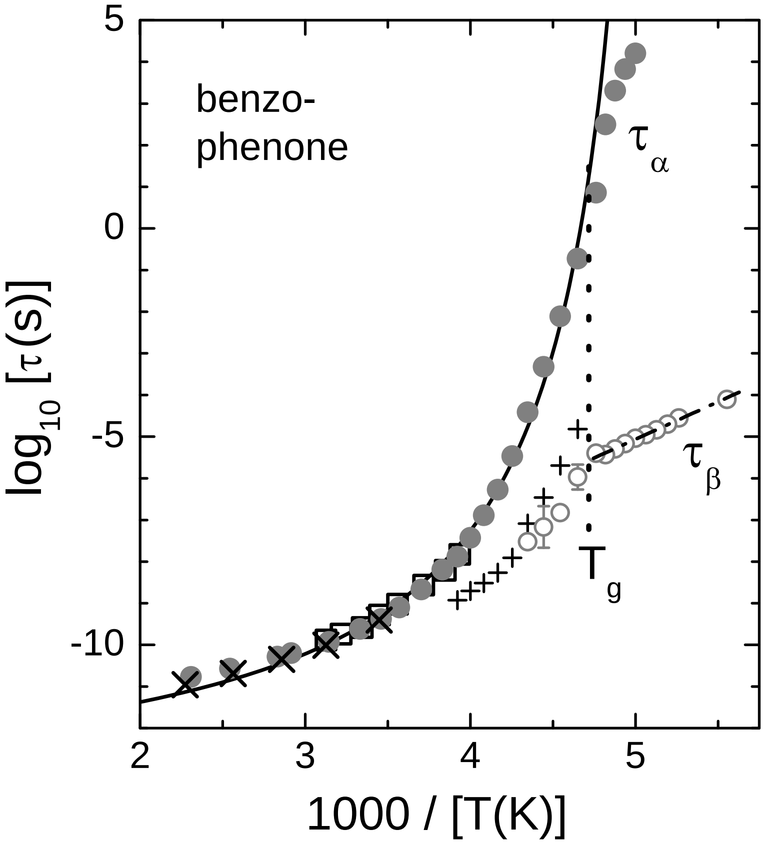

Figure 4.8: α- and β-relaxation times (full and open circles)[50] as determined from the fits, partly shown in figure 4.6. Open squares and ×´s show literature data from OKE and DLS experiments.[182,129] The solid line is a fit of the dielectric relaxation times, using a VFT equation. The dash dotted line shows a fit of the β-relaxation time for $T < T_g$, assuming an Arrhenius law. The plus signs show the primitive relaxation times of the CM[33] as calculated from equation (2.14).

As observed before,[61,141] when scaling the results of different methods on the α-relaxation peak, the minimum region is differently pronounced in each method. For molecular glass formers usually most excess intensity is observed in neutron scattering data, followed by light scattering and dielectric data. To our knowledge, no neutron scattering experiments have been performed until now, but at least for the DLS and dielectric data, this statement can be verified in BZP.[50,131]

4.2 Glassy dynamics in mono-, di-, and tripropylene glycol

Many groups studied the dynamics of propylene glycols of different polymerisation grade and by different techniques, e.g., as neutron[192] and light scattering,[193–197] optical Kerr effect,[198] photothermal[199] and dielectric spectroscopy.[48,200–208] The frequency range usually was restricted to frequencies below 10 MHz, except of Ref. 201 where spectra up to 1 GHz were reported. In the present work, the frequency range is extended up into the far-infrared region for propylene glycol ($C_3H_8O_2$), dipropylene glycol ($C_6H_{14}O_3$) and tripropylene glycol ($C_9H_{20}O_4$). Previous measurements are reported in Ref. 209 and further discussions are provided in Ref. 179. Details on the molecular masses and glass-transition temperatures are given in table 1. In the following discussion, special emphasis is put on the dynamics beyond the α-relaxation and the systematic behaviour regarding molecular size effects. To highlight similarities and differences between molecular and polymeric glass formers a short discussion of the relaxational behaviour of the polymer polypropylene glycol 4000 (PPG 4000) is included. In addition, results from dielectric spectroscopy are compared to light scattering (only for the monomer), neutron scattering and positron annihilation lifetime spectroscopy (PALS) measurements.

	propylene glycol	dipropylene glycol	tripropylene glycol
Chemical formula	$C_3H_8O_2$	$C_6H_{14}O_3$	$C_9H_{20}O_4$
$M[g/mol]$	76.1	134.2	192.3
$T_g(DSC)$	170	196	194
$T_g(diel)$	166	189	193

Table 1: Characteristic parameters of PG, DPG and TPG.

4.2.1 Broadband dielectric spectra

Figure 4.9 shows the frequency dependent dielectric loss $\varepsilon''(\nu)$ of (a) propylene glycol (PG), (b) dipropylene glycol (DPG) and (c) tripropylene glycol (TPG) for various temperatures. All spectra are dominated by the structural α-relaxation peak, shifting to higher frequencies with increasing temperature. The strong shift displays the tremendous slowing down of glassy dynamics towards the glass transition. At frequencies beyond the α-relaxation, an excess wing shows up for the monomer, while the dimer and trimer exhibit a well pronounced secondary relaxation peak.[48,205,207] With increasing temperature, this peak becomes successively submerged under the dominating α-peak, leading to an excess wing at about 210 K. Above 240 K both processes are merged.

To obtain information about the characteristic parameters of *α*- and *β*-relaxation, least square fits of the experimental data were simultaneously performed for real (not shown) and imaginary part of the dielectric permittivity. For the fitting procedure, a sum of the commonly used CD[39] and CC[37] functions is applied. The asymmetrically shaped CD function accounts for the *α*-, and the symmetrically broadened CC function for the slow *β*-relaxation. Above 220 K in PG and TPG and above 230 K in DPG, both relaxation processes are merged, so that the amplitude of the CC function in the fitting procedure was set to zero. As mentioned in section 4.1.2, an additive ansatz works well for data parameterisation, and there is no compelling need[50] for the use of an alternative[124] ansatz.

To higher frequencies, a shallow minimum shows up in the GHz regime of all three glycols. It shifts to higher frequencies with increasing temperature while its amplitude increases. Such behaviour is also found in other glass formers like, e.g., glycerol or propylene carbonate.[3,35,51–54] In the THz region, the so-called boson peak (BP) is observed. To maintain readability, in figures 4.9 (a) - (c) only room temperature measurements of the boson peak are shown.

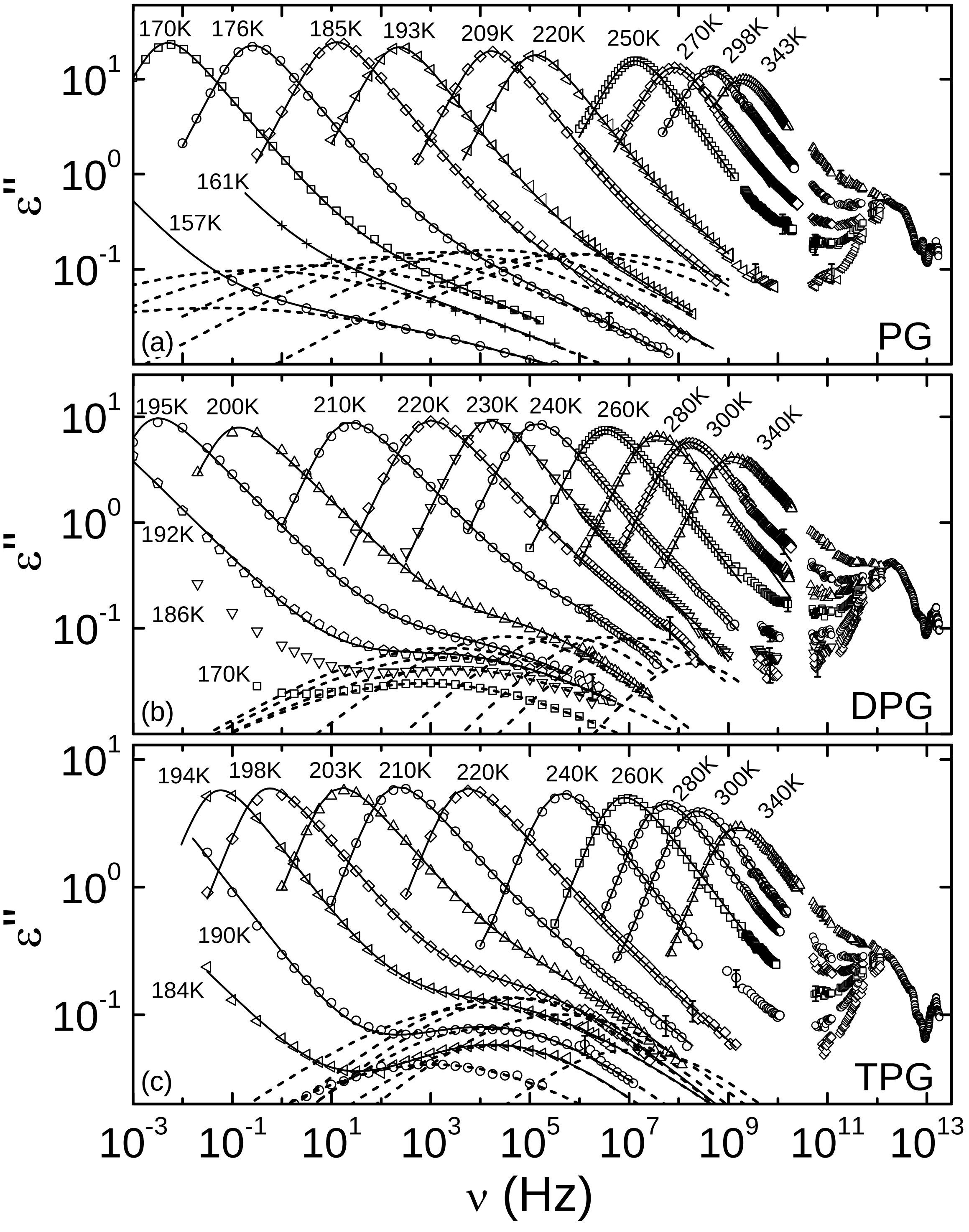

Figure 4.9: Frequency dependent dielectric loss of (a) propylene glycol, (b) dipropylene glycol and (c) tripropylene glycol. Solid lines are fits with a sum of a CD and CC function for the α- and β-relaxation, respectively. The dashed lines show the CC contribution. At $T \geq 220$ K for PG and TPG and $T \geq 230$ K for DPG, the CC amplitude was set to zero. In the THz-range the boson peak shows up. The low frequency data is partly shown in Ref. 179. For the present work, measurements above 20 GHz have been performed.

4.2.2 The α-relaxation

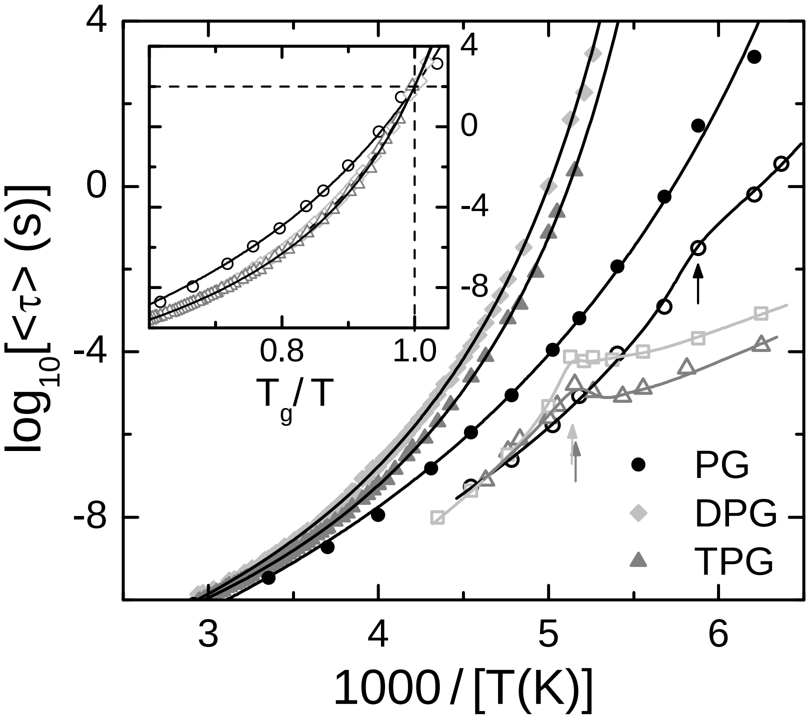

Figure 4.10: Average relaxation times $\langle\tau\rangle$ for the α- and β-relaxation as obtained from the fits shown in figure 4.9.[179] Solid lines are fits of the α-relaxation times (closed symbols) with a VFT law. Open symbols show the β-relaxation times, lines are to guide the eye. The arrows indicate the glass-transition temperatures. The inset shows the α-relaxation time in an Angell-plot.[83,84]

Figure 4.10 displays the average relaxation times in Arrhenius representation as determined from the fits, partly shown in figure 4.9. Closed symbols denote the average α-relaxation times, determined by $\langle\tau_\alpha\rangle = \tau_{CD}\beta_{CD}$, open symbols illustrate the β-relaxation times. Former clearly deviate for all three glycols from thermally activated behaviour and can be well parameterised by the phenomenological VFT-law, equation (2.7), which is typical for the dynamic behaviour of glassy matter. The fits are shown as solid lines.

	PG	DPG	TPG
τ_0 $[fs]$	14	25	53
T_{VF}	115	150	150
D	17	10	9
m	48	69	74
m^{207}	53	64	71

Table 2: Parameters as obtained from the VFT fits shown in figure 4.10. In addition the fragility parameter m as determined in this work and literature values from Ref. 207 are given.

Fit parameters, given in table 2, agree reasonably well with the values reported in literature.[200,201,207] In figure 4.10, the trimer relaxes faster than the dimer. A possible explanation may be that the flexibility of the molecular backbone of TPG is increased by the replacement of $-CH_2-$ units by ether links $-O-$ which lack the barrier to rotation put up by adjacent methylene protons.[210] Another possibility may be the onset of a transition to a polymer-like behaviour. In this case, segmental motions play a decisive role in the relaxation processes. However, in the Angel-plot (inset of figure 4.10), the behaviour of di- and trimer interchanged and the molecules relax the slower the bigger they are.

The fragility parameter m was determined from the inset of figure 4.10, and increases from 48 to 74 with increasing molecular size. These values characterize the glycols as intermediate glass-formers. Similar values for m are reported in literature[207] (cf. table 2). In the framework of the potential energy landscape in configuration space, the fragility is related to the structure of its surface.[211] Within this picture, the increase of fragility accounts for a landscape that has a higher density of minima due to the higher complexity of the bigger molecules. Following this argument, the energy landscape of the more complex TPG seems to be quite rougher then for PG and DPG, inducing a higher fragility index.

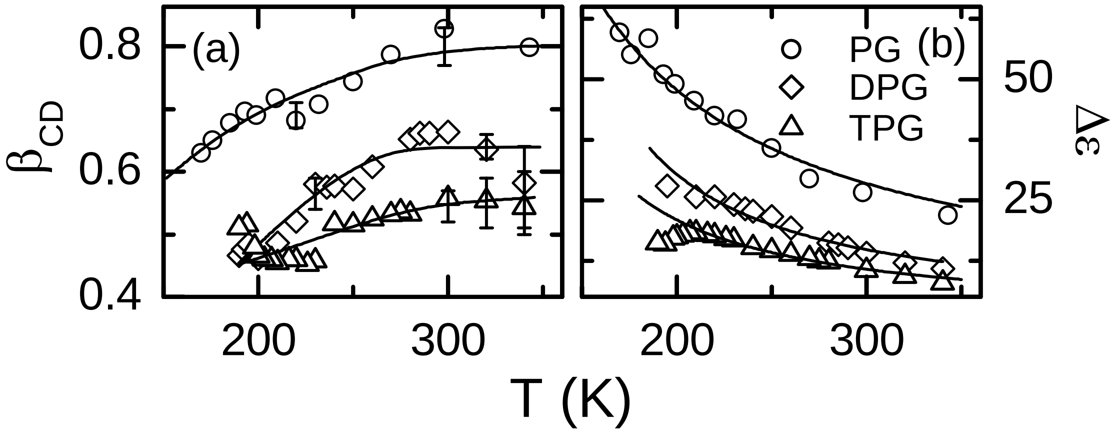

Figure 4.11: Width parameter β_{CD} (a) and relaxation strength $\Delta\varepsilon$ (b) of the α-relaxation as obtained by the fits shown in figure 4.9. Solid lines in (a) are to guide the eye, in (b) they are fits with a Curie-Weiss law.[179.]

The width parameter $\beta_{CD}(T)$ and the relaxation strength $\Delta\varepsilon(T)$ of the α-relaxation are displayed in figures 4.11 (a) and (b) for mono-, di- and trimer. While β_{CD} increases with increasing temperature, $\Delta\varepsilon$ behaves vice versa. Solid lines in figure 4.11 (b) show the parameterisation of $\Delta\varepsilon(T)$ by a Curie-Weiss law, $\Delta\varepsilon \sim 1/(T-T_{CW})$. The Curie Weiss temperatures[179] are determined to 53, 105 and 95 K for PG, DPG and TPG, respectively. The deviations showing up for DPG and TPG when approaching 200 K are ascribed to the fact that their glass transition temperatures are in this temperature region and thus the samples fall out of thermodynamic equilibrium. The width parameters shown in figure 4.11 (a), saturate for high temperatures below unity for all three glycols. However, the saturation limit decreases with increasing molecular size from β_{CD} =0.55, 0.63 and 0.8, approximately.

4.2.3 Secondary relaxations

The β-relaxation times for PG, DPG and TPG as obtained from the CC contribution of the fits, partly shown in figure 4.9, are displayed as open symbols in the relaxation map of figure 4.10. Corresponding lines are to guide the eyes. They do not show simple Arrhenius behaviour and the course of the relaxation times is qualitatively different below and above T_g. In the following we call these secondary peaks, showing up in figure 4.9 at ambient pressure, β-peaks. One has to be aware that nomenclature in literature is not consistent as they are sometimes called γ-peaks, as at high-pressure additional peaks show up which are then called β-peaks.[201,204,212]

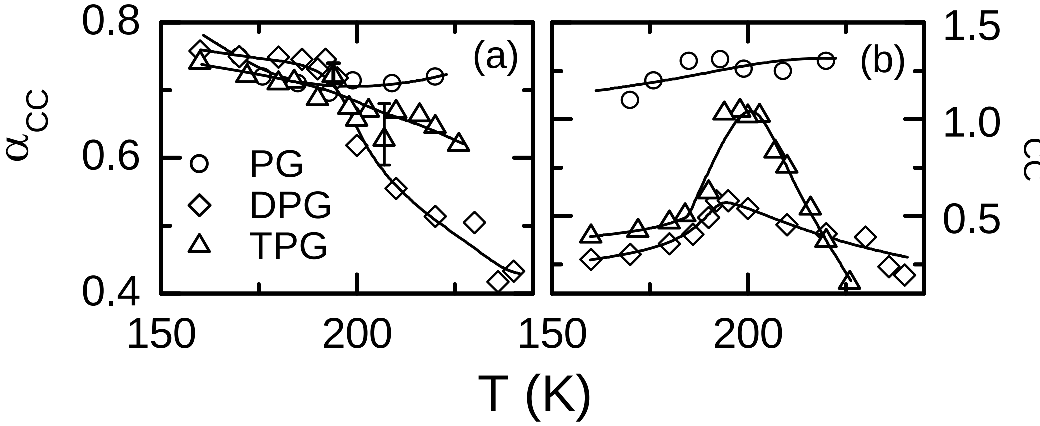

Figure 4.12: Width parameter α_{CC} (a) and relaxation strength $\Delta\varepsilon_{CC}$ (b) of the β-relaxation as obtained by the fits shown in figure 4.9. Solid lines in (a) and (b) are to guide the eyes.[179]

In the sub-T_g region some kind of minimum is observed in the β-relaxation times of the di- and trimer. It was not possible to perform the fittings in a way that no minimum appeared. There are different explanations[82,180,212] of this behaviour in literature, which are partly discussed below.

Above T_g (indicated by the arrows in figure 4.10) $\tau_\beta(T)$ shows a transition into a stronger temperature dependence than at $T < T_g$. For other glass-formers, like Salol or xylitol, similar behaviour is known from literature.[25,48,50] However, one should be aware, that for $T > T_g$ determined β-relaxation times are less reliable due to the strong merging of the structural α- and the secondary β-process. For this reason the behaviour in this region is not finally clarified.[81]

The width parameters α_{CC} and the relaxation strengths $\Delta\varepsilon_{CC}$ of the β-relaxations are provided in figures 4.12 (a) and (b), respectively. α_{CC} tends to decrease for all three glycols, i.e., the β-peaks narrow with increasing temperature,[179] a typical behaviour for secondary relaxations.[23,50] Located close to T_g, the di- and trimer show a peak in $\Delta\varepsilon_{CC}(T)$ This behaviour is predicted by the minimal model,[82] but it is not clear if the decrease above T_g is an artefact due to merging.

The behaviour of the secondary relaxations of propylene glycols were extensively studied and discussed in various previous publications.[48,201,204] In the monomer, the secondary relaxation was classified as a genuine JG-relaxation,[28] while the situation in the other glycols is quite different, as the secondary peaks were identified as non-JG.[201,204] Remarkably, from the relaxation map of figure 4.10 it is obvious that the β-dynamics for all three glycols approach each other with increasing temperature. This seems to contradict the fact that the β-relaxation has different microscopic origins in PG and DPG/TPG.[201,204] Pressure experiments revealed the existence of a further secondary relaxation peak in DPG and TPG, situated in the frequency range between α- and β-relaxation.[204] This additional process, appearing only at elevated pressure, was identified as genuine JG-relaxation.

The anomalous behaviour of the β-relaxation times exhibiting a minimum in $\tau_\beta(T)$, was also observed by J. C. Dyre and N. B. Olsen[82] for TPG. They proposed the so-called minimal model (chapter 2.4.2) for β-relaxations in viscous liquids. This model is clearly oversimplified but it is able to make the contrasts between the β-relaxation in the liquid and the glassy state of matter clear. Moreover, Paluch *et al.*[205] applied the minimal model successfully to fit the β-relaxation times of different polypropylene glycols. They found out, that the parameters of the double well potential, namely U and Δ decrease with increasing molecular weight, and ascribe this behaviour to the smaller amount of H-bonds per unit volume.[205]

In addition, this minimum appears in the data obtained from high pressure experiments of the Paluch group.[212] The application of pressure leads to a better separation of the structural α- and the secondary β-process and therefore nonmonotonic behaviour of $\tau_\beta(T)$ is regarded as a real physical phenomenon and not as a fitting artefact.[212]
Shortly after publishing the analysis in the framework of the minimal model,[205] Grzybowska *et al.*[212] analysed the same data with the so-called nonmonotonic relaxation kinetic model[212–214] (NRKM). They pointed out, that the analysis in terms of the MM leaves the origin of secondary relaxations unresolved. In opposite, within the NRKM, they relate the anomalous β-relaxation behaviour to changes in the dynamics of hydrogen bonding.[212]

Ngai *et al.*[180] explained the purported anomaly of the β-relaxation near and above T_g by the effect of encroachment. They state that deep in the glassy state the β-relaxation is not influenced by the JG-process. Latter is not resolved at normal pressure and situated in the frequency range between α- and β-relaxation.[212] So, when the β-relaxation is not influenced, τ_β shows usual Arrhenius behaviour. Nevertheless, near and above T_g the relaxation times of both processes become comparable and are no longer independent of each other. According to Ngai *et al.*, the β-relaxation is then hybridized by the JG-relaxation and the relaxation times approach each other. This becomes noticeable in the development of a minimum in the relaxation times. Figure 4.13 compares α- and β-relaxation times of DPG and TPG as determined from our fits (open circles) and from Ref. 180 (plusses and crosses, respectively). In addition, open squares show the JG relaxation times τ_{JG} as calculated from the α-relaxation times in the framework of the coupling model (shown as plusses) and $n = 0.37$ by equation (2.13). The overall behaviour resembles that, suggested by Ngai *et al.*[180] The approach of τ_{JG} as determined from the coupling model to τ_γ on increasing temperature or decreasing pressure (see Ref. 180) is taken as evidence that this hybridization of the β-relaxation with the JG relaxation causes the anomalous T-dependence of τ_γ.

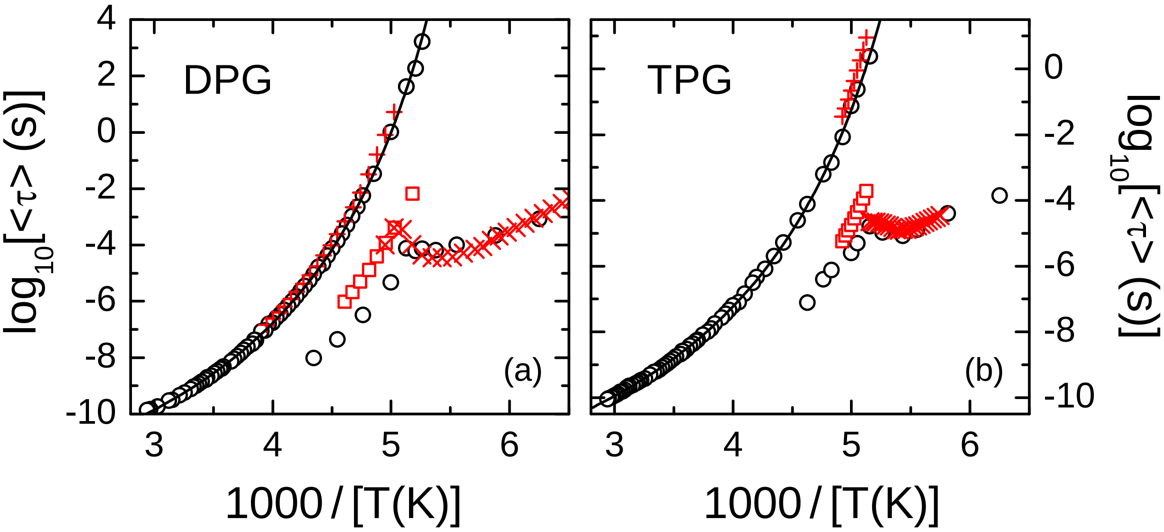

Figure 4.13: The open circles are the average relaxation times of α- and β-process as obtained by the fits shown in figure 4.9. Plusses and crosses show relaxation times as determined in Ref. 180. Open squares are primitive relaxation times calculated from the α-relaxation times.[179]

The data of the present work extends the frequency range beyond 1 MHz and thus the shoulder or wing caused by the secondary relaxation is resolved up to higher temperatures. Therefore, it is possible to determine a couple of β-relaxation times at temperatures significantly above T_g, which may be due to true JG-relaxations. Deviations of the α-relaxation times maybe due to the fact that we generally show mean relaxation times

$\langle\tau_\alpha\rangle = \tau_{CD}\beta_{CD}$. In $\tau_\beta(T)$ stronger deviations at high temperatures occur, as the fit results in this region suffer from the merging of α- and β-process and for this reason should have large error bars. Nevertheless, both sets of fit parameters agree, at least qualitatively, quite reasonably.

4.2.4 *The fast β-relaxation*

Figure 4.14 shows a zoom into the high frequency region of the dielectric loss of PG (a), DPG (b) and TPG (c) for various temperatures. To provide evidence for excess intensity in the minimum region, again a model free check was performed for one representative temperature (270 K or 280 K) in each sample. For this purpose the data was analysed with a simple sum of two power laws, accounting for the crossover from the α-relaxation (or excess wing, if visible) to the boson peak. For the increase towards the boson peak, the smallest possible exponent $n = 1$[112] is chosen. The fits are shown as dashed lines in the insets in figures 4.14 (a) - (c) and reveal that the $\varepsilon''(\nu)$ minimum in all cases is too shallow to be explained in such a simple way. This gives evidence for the contribution of additional fast processes to the dynamics of the investigated materials.

One possible explanation of a constant loss contribution gives, e.g., the extended coupling model.[55] Assuming an additional constant loss contribution, equation (4.1) is applied for the description of the minimum region. Fits performed for two representative temperatures are shown for each glycol as solid lines in the insets of figures 4.14 (a) - (c). Apparently, equation (4.1) is a good tool for data description as the fits characterize the data quite well. The parameter c_3 was set to zero.

	PG	DPG	TPG
a	0.33	0.319	0.302
b	0.653	0.612	0.55
λ	0.692	0.717	0.7556
γ	2.28	2.38	2.57
T_c (K)	239	259	250
T_c/T_g	1.41	1.32	1.28

Table 3: Parameters as derived from data analysis with idealized MCT.

Special attention was paid to check for a consistent description of the $\varepsilon''(\nu)$ minima within the framework of idealized MCT (chapter 2.4.5). Solid lines in figures 4.14 (a) - (c) show fits obtained by equation (2.20). The increase towards the boson peak becomes too steep for lower temperatures and does not allow for reasonable fits. However, the fits in figures 4.14 (a) - (c) provide a good description of the data from 1 - 2 decades below ν_{min} up to the boson peak frequency for $T \geq 270$ K. Deviations near the critical temperature T_c, are expected, as the simple interpolation formula, equation (2.20), is only valid in the vicinity of the minimum. Especially at low temperatures, deviations of data and fits towards the boson peak are observed. Exponent parameters a and b of the critical and von Schweidler law, as well as the related system parameter λ are provided in table 3. A slight decrease of a and b with increasing molecular size is observed. This accounts for a slight broadening of the minimum.

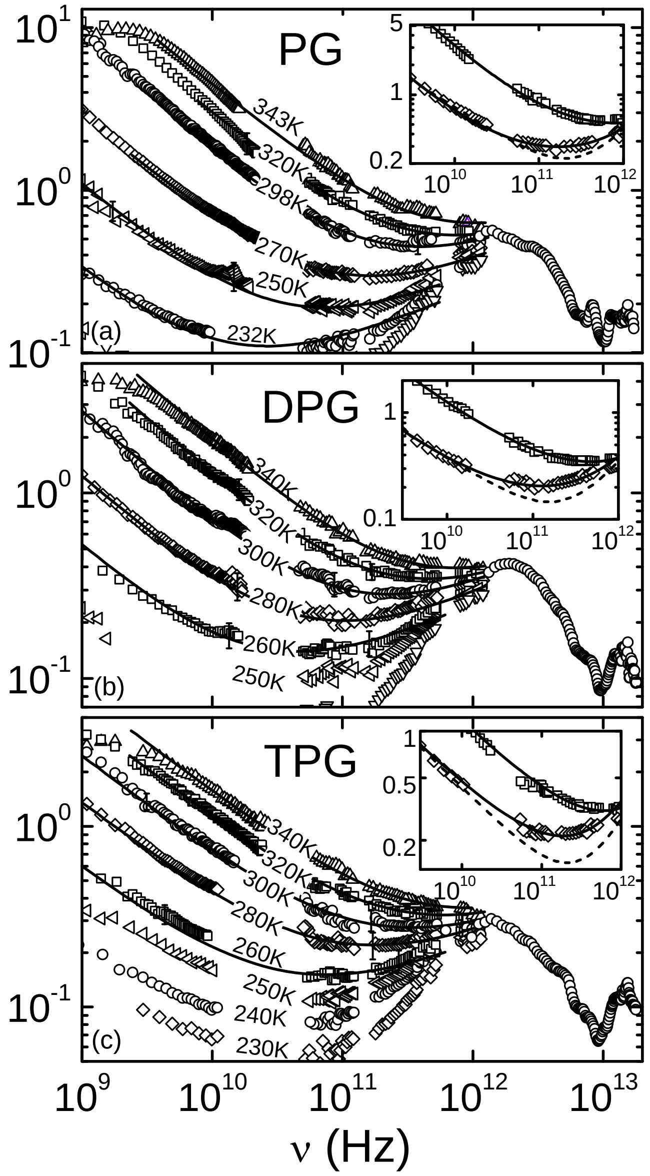

Figure 4.14: $\varepsilon''(\nu)$ of PG (a), DPG (b) and TPG (c) at high frequencies for various temperatures. The lines are fits with equation (2.20). The insets show spectra for two temperatures, fitted with equation (2.15). The parameter c_3 was set to zero. Dashed lines are calculated by the sum of two power laws. Data is partly published in Ref. 179.

Figures 4.15 (a) - (i) show the mode coupling parameters ε_{min} and ν_{min} as obtained from the fits with equation (2.20), and the α-relaxation rate ν_{α} in a representation that leads to a linearization of the critical laws of MCT, equations (2.23), (2.25) and (2.26), respectively. Thus, straight lines should extrapolate to T_c. Depending on the choice of the exact extrapolation curve, different values for the critical temperatures can be obtained. Although similar analysis are often used in literature, the significance of this representation should not be overemphasized. In figure 4.15, the complete set of parameters is consistently described with $T_c \approx 239$ K for PG, $T_c \approx 259$ K for DPG and $T_c \approx 250$ K for TPG, as demonstrated by the solid lines. The ratio T_c/T_g decreases from 1.41 to 1.28 with increasing molecular size, only slightly above 1.2, a value often mentioned in literature. There, only for the monomer some inconsistent data were reported with critical temperatures of 198 K, 314 K and 251 K.[196,215]

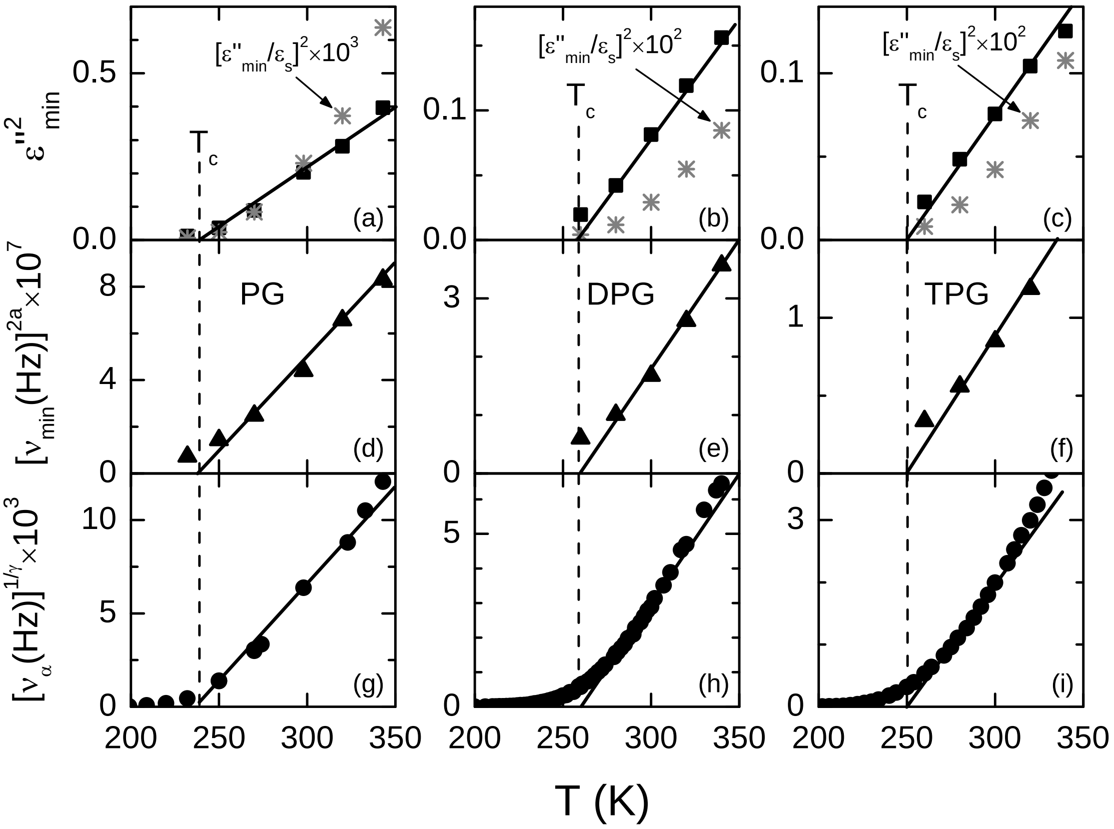

Figure 4.15: Temperature dependence of the minimum amplitude ε_{min} (a) - (c) and position ν_{min} (d) - (f) and of the α-relaxation rate ν_{α} (g) - (i) of PG, DPG and TPG.[179] ε_{min} and ν_{min} were obtained by fits with equation (2.20). According to the predictions of MCT, representations have been chosen that should result in linear behaviour. The solid lines demonstrate a consistent description of all three quantities with a T_c of 239 K for PG, 259 K for DPG and 250 K for TPG. In charts (a) - (c), additional results obtained from scaled loss data, as proposed in Ref. 216, are included as grey stars.

If the dielectric loss data is scaled with the static permittivity of the α-process before applying MCT, the temperature dependence of ε_{min} changes. This procedure was proposed by Adichtchev *et al.*,[216] but as the stars in figures 4.15 (a) - (c) demonstrate, even these scaled data are consistent with the values of T_c, given in table 3.

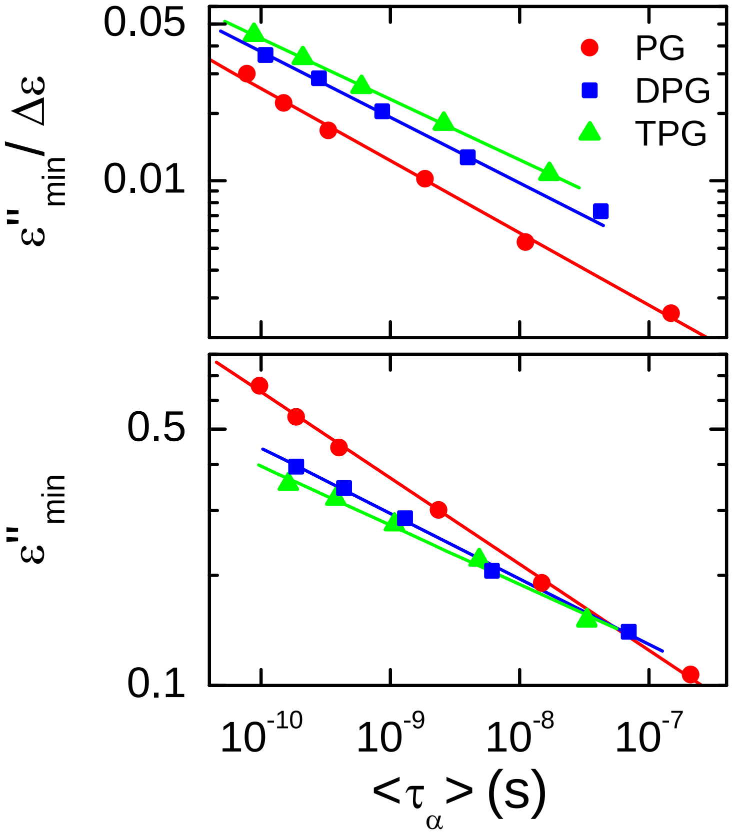

Figure 4.16: (a) Minimum amplitude of PG (●), DPG (■) and TPG (▲), relative to the α-relaxation strength vs. α-relaxation time. Solid lines are linear fits. The minimum amplitude is shown without scaling with $\Delta\varepsilon$ in (b). Partly published in Ref. 179.

To compare the behaviour of the fast β-relaxation of the different glycols, a new kind of representation is introduced:[179] Usually relaxation times at the same temperature are compared, but to account for the same α-relaxation dynamics, figure 4.16 (a) displays the minimum amplitude relative to the α-relaxation strength *vs.* the mean α-relaxation time $\langle\tau_\alpha\rangle$. The relative minimum amplitude and thus the strength of the fast β-process increases with increasing molecule size. Solid lines represent linear fits. The minimum amplitude is shown without scaling with $\Delta\varepsilon$ in (b). The increasing minimum amplitude relative to the α-relaxation strength with molecular size as shown in figure 4.16 (a), may be ascribed to a better coupling of the dielectric loss to translational modes for the larger molecules. Compared to the susceptibilities determined by scattering methods like light- or neutron scattering, the relative amplitude of the fast process is weaker in dielectric spectroscopy. However, these methods couple more directly to density fluctuations.[3,51,53,54] It can be speculated, that for the spatially more extended DPG and TPG molecules steric hindrance may rise and thus the coupling to translational motions becomes more important, and reorientational motions may be more strongly coupled to translational ones.

In principle, it should be possible from figure 4.16 (b) to determine the exponent parameters a and b of MCT via the relation

$$\varepsilon_{min} \sim \nu^{1/2\gamma} \tag{4.2}$$

with $\gamma = \frac{1}{2a} + \frac{1}{2b}$. The quality of this kind of analysis should not be overemphasized, as we obtain 2.13, 2.8 and 3.1 for γ instead of 2.28, 2.38 and 2.57 for PG, DPG and TPG, respectively. Although it mirrors the right trend, the absolute values do not correspond to each other. This analysis is not possible taking into account $\Delta\varepsilon$ as done in figure 4.16 (a), as the strength parameter is temperature dependent as shown in figure 4.11.

- **Test for scaling behaviour**

The scaling laws of MCT predict a temperature independent set of exponent parameters a and b for each material. Therefore, it should be possible to scale the $\varepsilon''(\nu)$-minimum (or the q-independent $\chi''(\nu)$-minimum, respectively) onto a master curve, determined by $\varepsilon''(\nu/\nu_{min})/\varepsilon_{min}$. For temperatures above T_c, values for minimum position and amplitude as obtained by the data analysis in the framework of idealized MCT as presented in the previous paragraph were used. For temperatures too low as to allow for reasonable fits, they are estimated by eye. Figures 4.17 (a) - (c) show the scaled spectra of PG, DPG and TPG, respectively. The same colours always correspond to the same temperature, as indicated in figure 4.17.

The scaling seems to work well for PG on the low frequency side of the minimum as all spectra fall onto the master curve. They all show the same temperature-independent slope. The calculated master curves are indicated as solid lines in each chart of figure 4.17. However, on the high-frequency side of the minimum clear deviations from the theoretical master curve occur. These may be attributed to the increasing influence of the boson peak on the spectra.

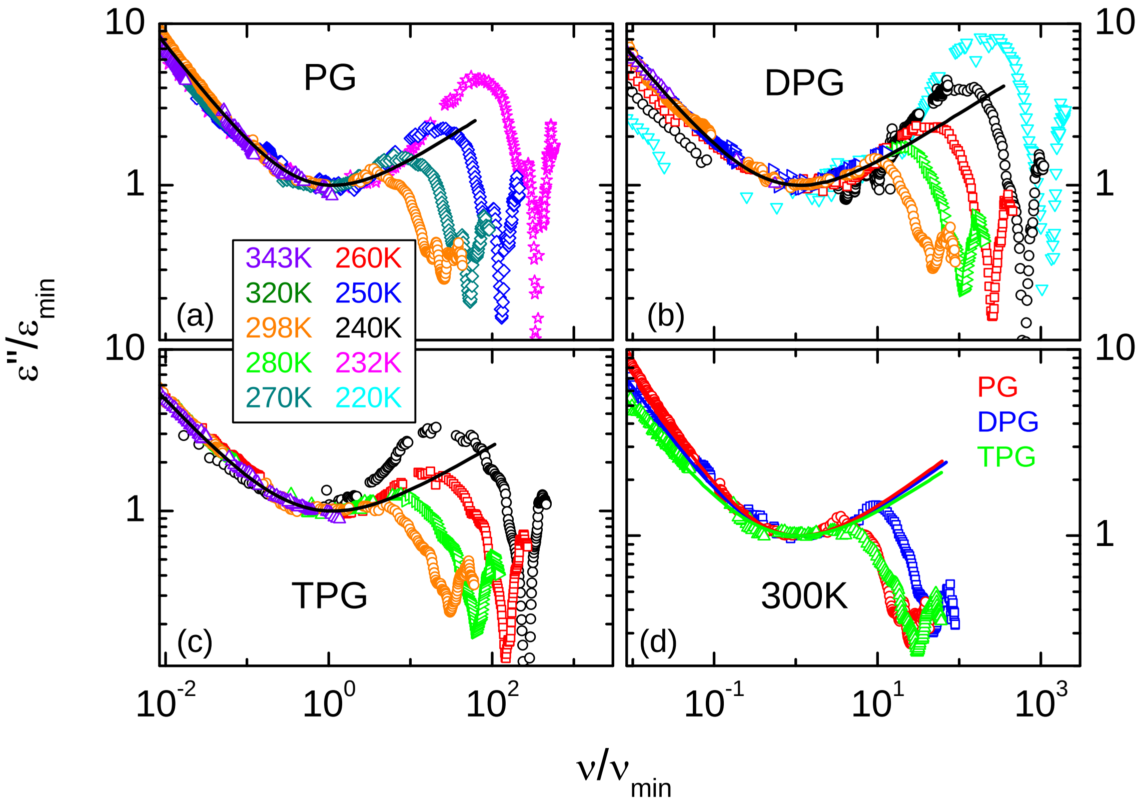

Figure 4.17: Master curves $\varepsilon''/\varepsilon_{min}$ vs. ν/ν_{min} for PG (a), DPG (b), and TPG (c) as obtained from the datasets of figure 4.9. Except for the 220 - 240 K curves, for scaling always ε_{min} and ν_{min} as obtained from MCT fits from equation (2.20) were used. In (d) the behaviour at 300 K (298 K for the monomer) is compared directly for all three glycols.

Also in figures 4.17 (b) and (c) the measured curves fall onto the master curve and the von Schweidler law is nicely seen. In contrast to the monomer, the scaling on the high-frequency flank seems to work better, as the curves coincide with the shown master curve in a broader frequency region. However, deviations due to the increasing role of the boson peak show up. The deviations at 220 K and 240 K for DPG and at 240 K for TPG are in accord with MCT as the scaling is expected to fail at temperatures below T_c.

The critical law is nicely seen in frames (a) - (c) on the high-frequency flank of the minimum. In contrast to the scaling behaviour of glycerol and the investigated binary glycerol-LiCl mixtures (cf. section 4.3.3), the minimum is smoothly shaped almost to the onset of the maximum of the boson peak.

Figure 4.17 (d) shows a comparison for all samples at the same temperature (300 K for DPG and TPG, 298 K for PG). According to the increase of the system parameter λ with increasing molecule size, the scaled curves show a slight broadening in the minimum region. This is obvious as λ is directly related to the power law exponents a and b via equation (2.22), characterizing the slopes of low and high frequency flank of the minimum.

- **Analysis in the framework of the F12-modell**

In addition to the MCT analysis in the framework of idealized MCT (I-MCT), a MCT analysis with the two-correlator F_{12} model is performed. This schematic model is defined by the equation of motion (2.16) and the memory kernels, equations (2.18) and (2.19), as explained in section 2.4.5. The inner loop of the fit routine calculates $\Phi(t)$ and $\Phi_s(t)$ by iteratively solving equation (2.16). The obtained susceptibilities are fitted to the experimental data. For details on the fitting procedure see Ref. 217.

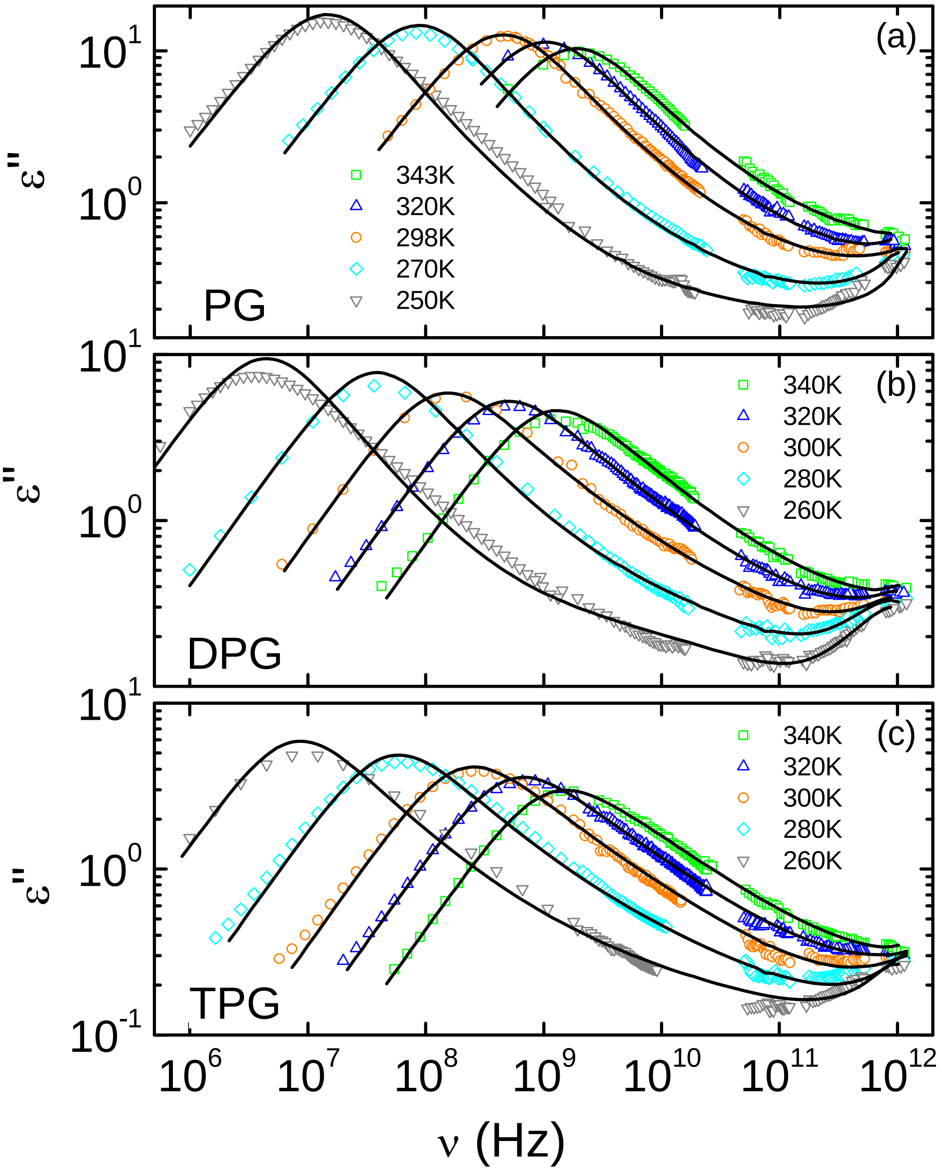

Figure 4.18: Dielectric loss for propylene glycol (a), dipropylene glycol (b) and tripropylene glycol (c) for selected temperatures. The legend in frame (c) also accounts for frame (b). Solid lines are fits by solutions of the two-component schematic F_{12} model of MCT, as explained in section 2.4.5.

Solid lines shown in figure 4.18 are fits obtained by solving these equations. In contrast to the I-MCT analysis, the analysis now is extended to frequencies including the α-relaxation process. In each compound, the fits give a reasonable representation of the data at least for the three highest temperatures. For $T \leq 270$ K for PG and 280 K for di- and tripropylene glycol, deviations of the fits and the α-peak amplitude are observed. In addition to the deviations in the region of the structural relaxation peak, the fits fail on the low-frequency flank of the minimum for DPG and TPG at 260 K, as some kind of additional power law seems to develop in the fits, which cannot be observed in the data. However, it was not possible to perform better fits for these temperatures. An explanation is perhaps that 260 K is quite close to the critical temperature, which was estimated by the previous I-MCT analysis as 259 and 250 K for DPG and TPG, respectively. As we do not consider additional hopping processes to restore the ergodicity breaking, the fits are expected to fail close to T_c.

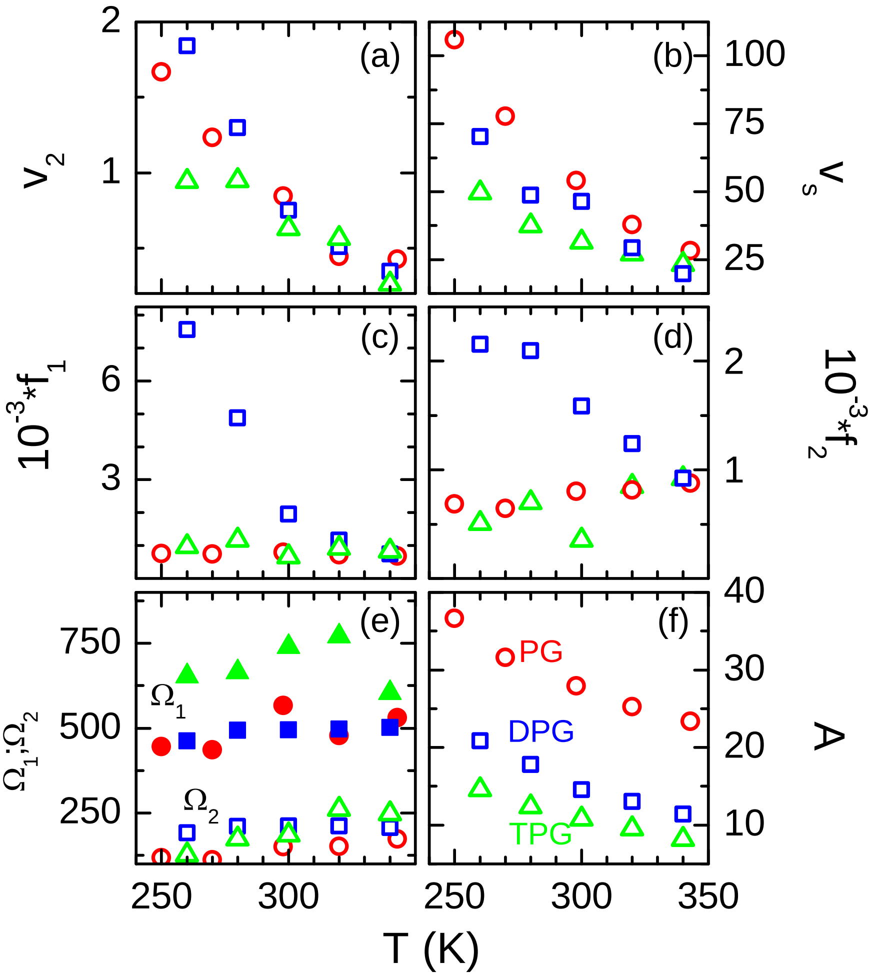

Figure 4.19: Parameters as obtained by the fits with the schematic F_{12}-model of MCT. Circles account for PG, squares for DPG and triangles for TPG. The frames show the coupling coefficients v_2 (a) and v_s (b), damping coefficients f_1 (c) and f_2 (d) as well as the characteristic frequencies Ω_1 and Ω_2 (e) and the amplitude A (f).

Fit parameters are shown in figures 4.19 (a) - (f). The schematic F_{12}-model contains several parameters. The two frequencies Ω_1 and Ω_2 characterize the ballistic short time motion, while the damping coefficients f_1 and f_2 represent fast contributions to the memory kernel in equation (2.16). v_1, v_2 and v_s are coupling coefficients. A further parameter A is not part of the model but needed to adjust the experimental intensity scale. The parameters are expected to vary smoothly and monotonously with temperature.[217] The coupling coefficients v_2 (a) and v_s (b) decrease continuosly with increasing temperature, while v_1 stays nearly constant at least at high temperatures. However, as v_1 and v_2 are additionally shown in the phase diagram in figure 4.20, former is not shown in figure 4.19. In frames (c) and (d), the damping coefficients f_1 and f_2, in (e) the characteristic frequencies Ω_1 and Ω_2 and in (f) the amplitude A are shown. The frequencies and the amplitude show a smooth evolution with temperature. The friction coefficients for PG and TPG display an increasing tendency with increasing temperature, while they are decreasing with temperature for DPG. However, it was not possible to perform the fits in a way that the friction coefficients simultaneously show a corresponding behaviour for all glycols.

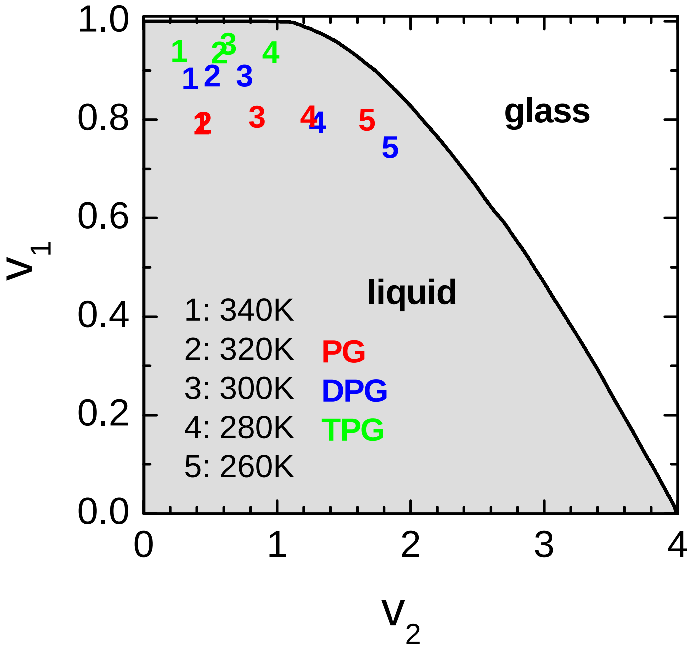

Figure 4.20: Mode coupling coefficients v_1 and v_2 in the phase diagram of the F_{12}-model. The solid line is curve of the liquid to glass transition.

Figure 4.20 shows the mode coupling coefficients v_1 and v_2 in the phase diagram of the F_{12}-model. The solid line indicates the ideal glass transition boundary. The frequency dependence of the α-relaxation is essentially given by the coupling coefficients.[217] For all glycols the coupling parameters fall into the liquid phase but a general tendency to approach the glass-transition singularity with decreasing temperature is observed.

However, from the available fit parameters it is not possible to extrapolate with sufficient accuracy a hypothetical trajectory by which each glycol would approach the glass transition if further supercooled. The system parameter λ cannot be determined as it is defined by the v_1 and v_2 values where the trajectory perpendicular crosses the glass transition line via $v_1 = (2\lambda - 1)/\lambda^2$ and $v_2 = 1/\lambda^2$ with $0.5 \leq \lambda < 1$.[218]

4.2.5 The boson peak

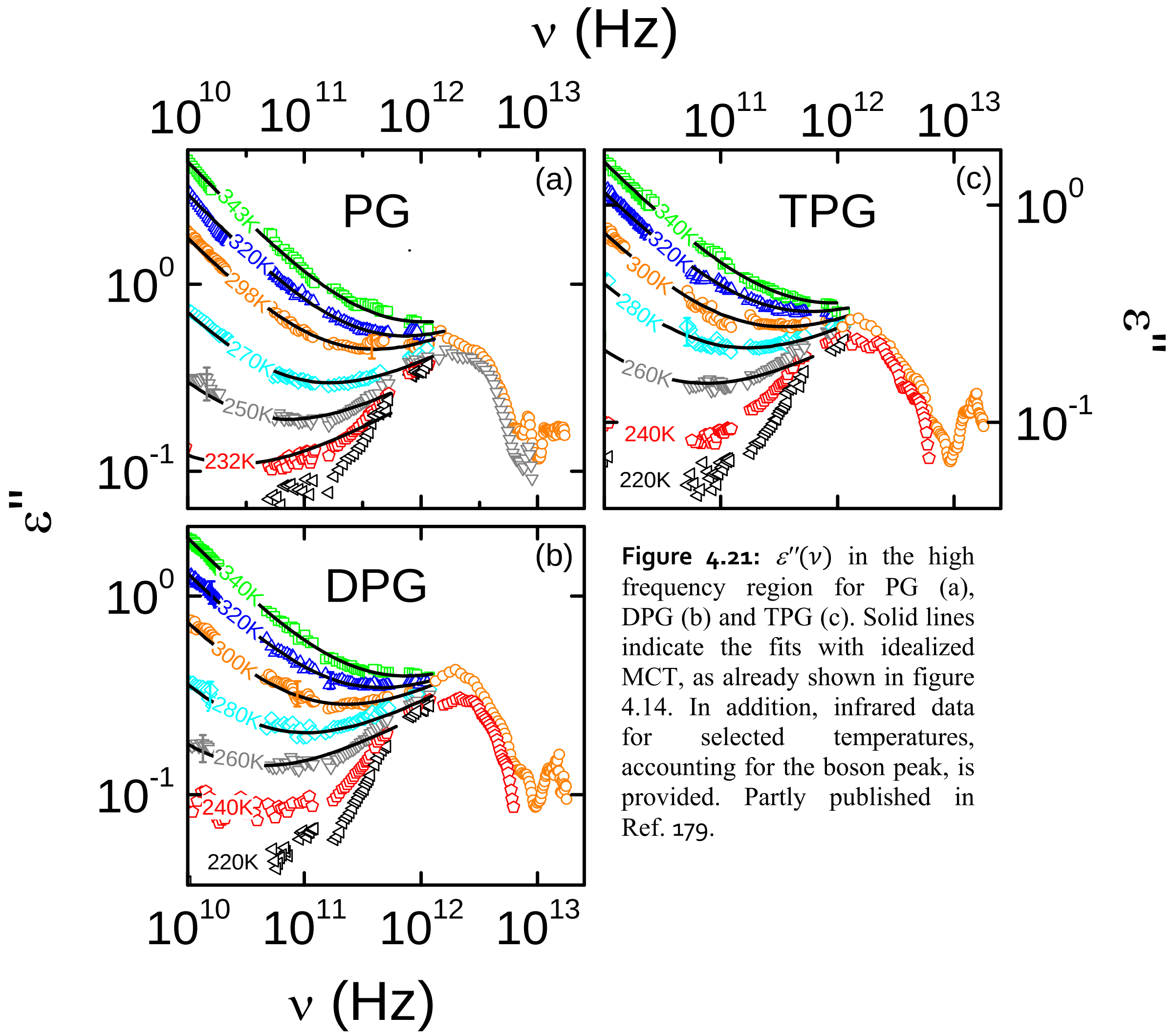

Figure 4.21: $\varepsilon''(\nu)$ in the high frequency region for PG (a), DPG (b) and TPG (c). Solid lines indicate the fits with idealized MCT, as already shown in figure 4.14. In addition, infrared data for selected temperatures, accounting for the boson peak, is provided. Partly published in Ref. 179.

Figure 4.21 shows the frequency dependent dielectric loss of PG, DPG and TPG in the high frequency region. Solid lines indicate fits with idealized MCT, as already provided in figure 4.14. In addition, infrared data for selected temperatures, accounting for the boson peak, is shown. However, as the temperature dependence in this region is negligible, and to maintain readability only two representative temperatures are shown in each frame of figure 4.21. These results add three further molecular glass formers to the sparse list of materials [3,22,60,219–223] for which real broadband spectra, including the FIR region, exist. We now present a systematic study of the dependence of the BP on molecular size and in chapter 4.3.3.2 of the influence on the ion content.

The microscopic peaks provided in figures 4.21 (a) - (c) are shaped rather broad with a relatively moderately increasing low frequency wing. The resonance like, very sharp infrared bands showing up at about 10^{13} Hz in the room temperature spectra of figures 4.21 (a) - (c) are ascribed to intramolecular excitations.[224,225] This feature is decoupled from glass-formation. Due to experimental difficulties, the low temperature spectra in the FIR region could not be measured with sufficient accuracy above 10 THz, so that the intramolecular modes are not shown here.

In literature, the BP often is defined as a peak in the density of states (DOS) divided by the squared frequency, $g(\omega)/\omega^2$, implying an excess over the Debye vibrational DOS. It was demonstrated,[3,22,219] that IR spectroscopy leads to very similar results as light- or neutron scattering although it mainly couples to reorientational instead of translational motions. For sake of comparison, figure 4.22 shows spectra of $\varepsilon''T/\omega$, which is a good approximation of $g(\omega)/\omega^2$, for PG (at 250 K), DPG (260 K) and TPG (260 K) together with data of the canonical glass former glycerol and the plastic crystal *ortho*-carborane (OCA).

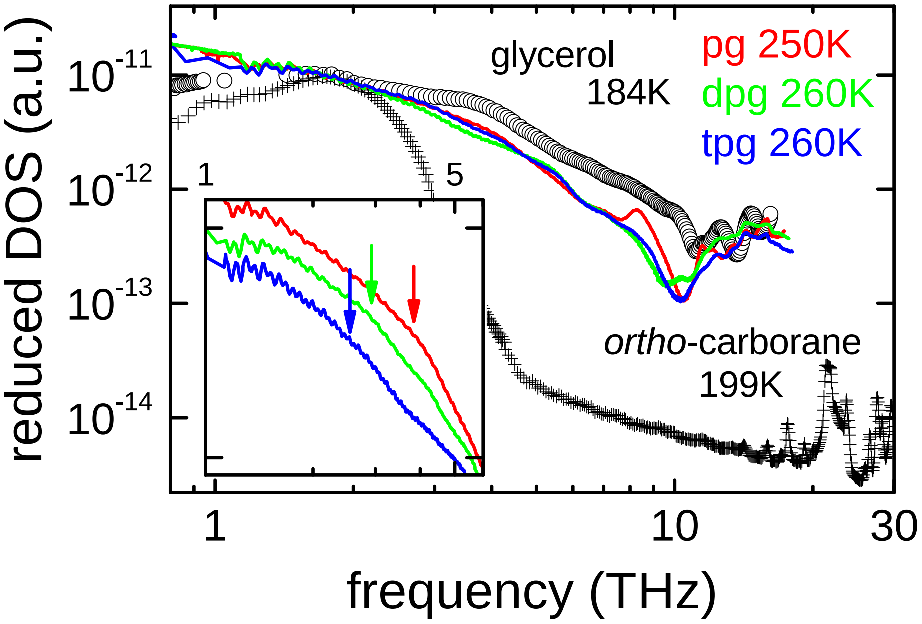

Figure 4.22: Spectra of $\varepsilon''T/\omega$ in the THz region for glycerol[60] and plastic crystalline OCA[60] and the investigated glycols. The plotted quantity is approximately proportional to the reduced DOS, divided by the squared frequency, $g(\omega)/\omega^2$. The inset shows a zoom into the glycol spectra, which are vertically shifted by an arbitrary factor to obtain readability. The arrows indicate a slight stiffening of the phonon modes with increasing molecular size.

The spectra of the canonical glass former glycerol looks quite similar compared to the glycol spectra. The high frequency wing exhibits a rather shallow decrease, before the intramolecular modes at about 10 THz come into play. However, the similarity of the overall curve characteristics is not puzzling, as glycerol and at least propylene glycol differ from each other only by one –OH group in their chemical structure.

Apart from the low frequency wing, the OCA spectra look quite different compared to the molecular glass formers. OCA is a prototypical plastic crystal,[226–228] and the OCA molecule, $B_{10}C_{12}H_{12}$, forms a rigid icosahedron, which is shaped nearly spherically and experiences only little steric hindrance for reorientational processes in the plastic crystalline phase. One possible explanation, given in Ref. 60 is, that the BP may reflect the complete phonon DOS, becoming IR active via the strong hybridization of collective phonon modes with local relaxational excitations.[3,22,220,221,229] As OCA can be viewed analogous to a monoatomic crystal, it should only exhibit purely acoustic Debye DOS, being responsible for the steep decrease at about 2 THz.

In addition, glycerol and the three glycols show some kind of double peak structure. There is plenty of room for speculations what this double peak structure may signify and if it is inherent to the spectral shape of molecular glass forming materials. One possibility may be that also optical phonon modes may play a role here, representing the complete vibrational DOS. The high-frequency part of the double peak structure is magnified in detail in the inset of figure 4.22. A slight shift of this shoulder to lower frequencies with increasing molecular size is observed, indicating a stiffening of the phonon modes. This behaviour may give a hint to denser packing of the molecules, maybe due to the increasing fraction of covalent bonding *vs.* van der Waals bonds with increasing molecular size.

4.2.6 Relaxational behaviour of the polymer PPG 4000

Figure 4.23 displays the frequency dependent dielectric spectra of polypropylene glycol 4000. With a weight of 4000g/mol one polymeric molecule has about 69 monomeric units. The spectra are dominated by the so-called α-relaxation peak, shifting to higher frequencies with increasing temperature. In polymers, the α-relaxation is not ascribed to the reorientational motion of the whole molecule, but to large-scale conformational rearrangements of the chain backbone. These rearrangements occur by a mechanism of hindered rotation around main-chain bonds,[230] that means they are associated with local segmental motions.

At frequencies beyond the α-relaxation peak, a further process, here labelled β-relaxation, is observed for temperatures below 278 K. The origin of secondary relaxations in polymers is not clear but they are often ascribed to hindered rotations of side-groups.[230]

In addition, at frequencies below the α-relaxation frequencies a further process appears. This feature is not observed in PG, DPG nor TPG, as it is typical only for polymers. It is called normal mode and related to the diffusional properties of the whole chains.

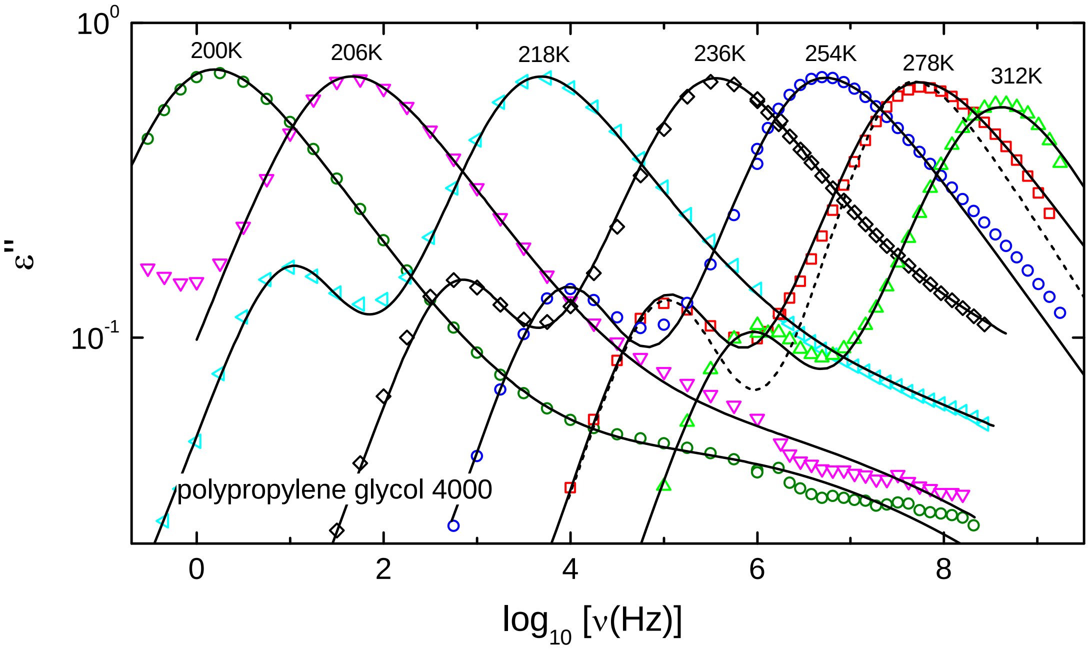

Figure 4.23: Frequency dependent dielectric loss of polypropylene glycol 4000 for various temperatures. Solid lines are fits with a sum of a CC, HN and a CC for the normal mode, the α-relaxation and the β-relaxation, respectively. The dashed lines shows a fit with a CD instead a HN function, accounting for the α-relaxation.

The normal mode process generally is only observed in so-called Type A polymers,[231] having a dipole moment parallel to the chain. Thus a total dipole vector, proportional to the end-to-end vector, results and hence the overall chain dynamics can be determined.[232]

Solid lines in figure 4.23 show fits with a sum of a CC, HN and a further CC law accounting for the normal mode, the α-relaxation and the β-relaxation, respectively. For sake of clearness the contributions of the particular relaxations are not shown. The α-relaxation is often parameterised by a CD function and no HN function is necessary. However, when assuming a CD function, the fitting procedure, as exemplarily shown by the dashed line for the 278 K curve, does not work sufficiently well. This may be due to additional contributions, e.g., ac-conductivity, contributing mainly at lower frequencies.

In figure 4.24, the relaxation times for the normal mode, α- and β-relaxation as obtained from the fits shown in figure 4.23, are displayed. The behaviour of the NM and the α-relaxation times deviate clearly from thermally activated Arrhenius behaviour. The solid and the dashed lines are fits with a VFT law. The β-relaxation times show an Arrhenius like behaviour and can be reasonably well described by a linear fit. Using the slope $m = 3.44$ of the linear fit, the energy barrier is calculated to $E_B = m \cdot k_B \cdot \ln 10 = 0.68$ eV.

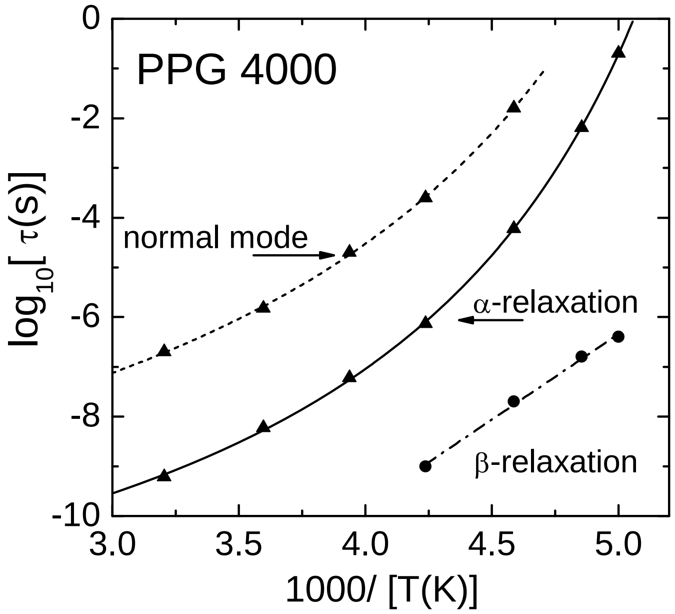

Figure 4.24: Relaxation times for the α- and β-relaxation and for the normal mode, as obtained from the fits shown in figure 4.23. The solid and dashed lines are fits with a VFT law. The dash-dotted line is an Arrhenius fit for the β-relaxation times.

Figure 4.25 displays the dielectric loss spectra at $T = 245$ K for different polypropylene glycol samples, with $13 \leq n \leq 69$ monomeric units. At this temperature, both, the segmental and normal mode relaxation is in the experimental window. The black lines display data, digitalized from Ref. 233, while the grey curve has been obtained by our own measurement of PPG 4000. As the segmental dynamics are largely unaffected by the chain length, all data exhibit the global peak at the same frequency. The peak positions of our measurement and the ones from literature[233] are slightly different. This may be due to the use of different temperature sensors, or to different thermal coupling. To enable a direct comparison, the data were normalized to the α-peak amplitude. However, the relative strength of the normal mode decreases steadily with increasing chain length, except for our sample. The positions of the α-relaxation and normal mode peak separate more with increasing molecular weight.

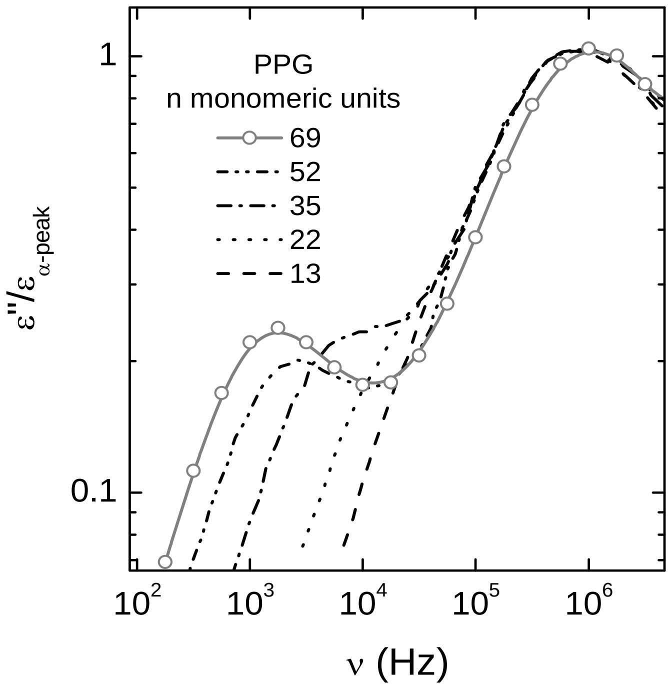

Figure 4.25: Black curves show dielectric loss spectra of PPG with different chain length at 245 K from Ref. 233. All spectra are normalized by the maximum of the α-peak. The grey curve is from our measurement of PPG 4000 at 243 K. The growth of the normal mode with increasing chain length is clearly visible.

4.2.7 *Comparison with other experimental methods*

4.2.7.1 *Light scattering*

In figure 4.26, the high frequency region of the dielectric loss spectra of PG (symbols) is compared with the imaginary part of the susceptibility as determined from Raman and Brillouin scattering experiments (solid lines).[195] The scattering results give no information on the absolute values of χ'', and the data sets have been vertically shifted to yield a comparable height of the boson peak. However, there is no rationale for this and scaling on the α-peak or on the minimum position may be justified as well.[1] It becomes clear from figure 4.26, that the α-peaks from dielectric spectroscopy are located at significantly lower frequencies if compared to light scattering. This is in contrast to the chemically similar glycerol, also a hydrogen-bonded molecular glass former, where different methods as dielectric spectroscopy, specific heat spectroscopy, ultrasonic's and light scattering lead to very similar α-relaxation times.[234–237] This indicates decoupling of reorientational and translational motions of the molecules in propylene glycol.

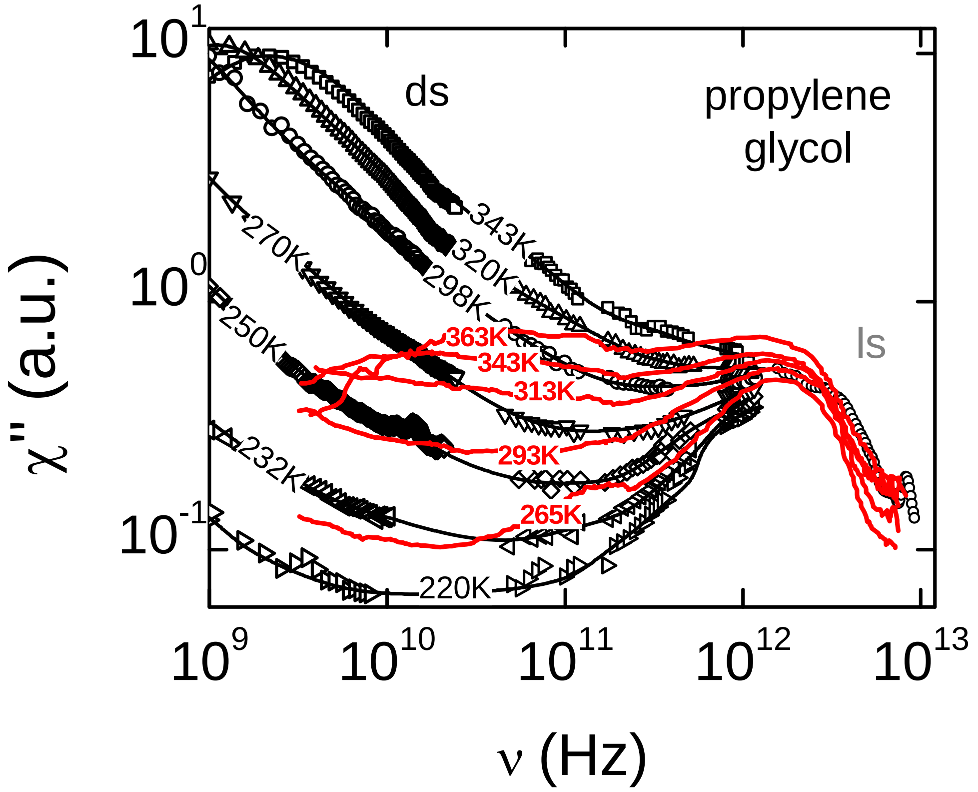

Figure 4.26: Frequency dependence of the imaginary part of the susceptibility of PG. The symbols represent the present dielectric results (ds), solid lines show light scattering (ls) data from Ref. 195. The ls data set has been vertically shifted to give a comparable intensity of the boson peak.

In contrast to the behaviour of the α-relaxation peak, the THz-peak is located at the same frequencies for both methods. In addition, the decrease at the high frequency flank is comparable. However, in comparison to the α-relaxation peak, the amplitude of the microscopic peak is much smaller in dielectric spectroscopy. A smaller ratio of α- and boson peak amplitude in dielectric spectra (compared to neutron and light scattering spectra) was found in experiments on Salol,[189] glycerol,[53] PC[54] and in numerical molecular-dynamics simulations of various glass-forming systems.[187,238,239] The differences arise from different coupling to translational and rotational degrees of freedom in both methods and an explanation was given by considering the different tensorial properties of the experimental methods.[134,137,187,218,240]

One of the main predictions of MCT[14,133,241] is, that the same parameters T_c and λ should arise from all different spectroscopic methods. This is clearly not the case for PG, as reported values of T_c and λ, determined from light scattering experiments are inconsistent[196,197,215] (values for T_c vary from 198 K to 314 K) and do not agree in any case with the ones determined by dielectric spectroscopy.[179]

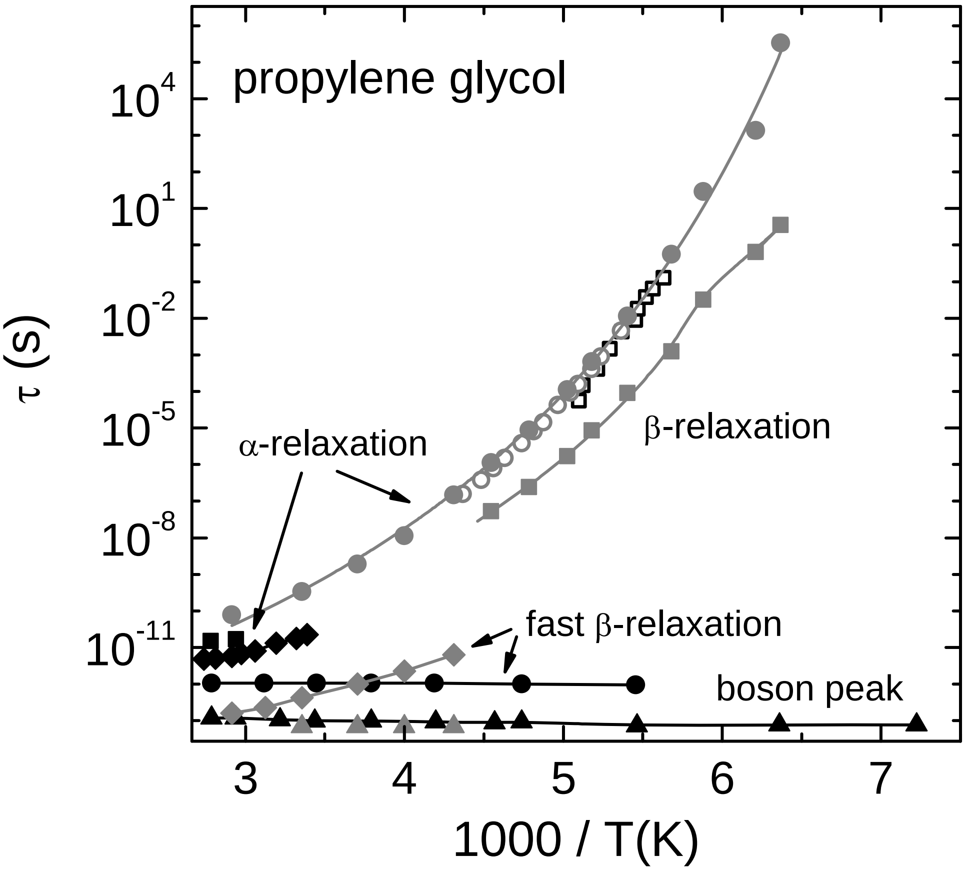

Figure 4.27: Relaxation times of PG as determined by different methods. Closed grey symbols are fit parameters of our own measurements. Open circles are from dielectric measurements from literature, open squares determined from photothermal measurements. Closed black symbols are determined from light scattering experiments.[195]

Light scattering data,[195] (shown as solid lines in figure 4.26), was fitted in Ref. 195 with an additive superposition of three peaks accounting for the α-relaxation, the fast β-relaxation and the boson peak. According to the fits, the so-called fast β-process seems to appear at the 313 K curve at about 190 GHz as a small bump and becomes more pronounced to lower temperatures. However, no such peak is visible in the dielectric data. Usually the fast β-process shows up as excess intensity in the minimum region and not as an additional relaxation process. The origin of this additional peak in the light scattering data remains unclear. The relaxation times, determined from both methods are provided in figure 4.27. The α-relaxation times from our dielectric measurements (closed grey circles) are in good accord with the α-relaxation times from dielectric (open circles) and photothermal (open squares) measurements from literature.[195] However, deviations in the range of one order of magnitude in the α-relaxation times determined by light scattering are observed. It is obvious from figure 4.27, that relaxation times of the fast β-process from light scattering do not correspond to the ones determined by dielectric spectroscopy (for the relaxation time, the minimum position was taken) nor to any other feature in the relaxation map shown in figure 4.27. From light scattering no slow β-relaxation process could be resolved.

Nevertheless, position and shape of the boson peak of both methods are in good accord, and their relaxation times are comparable (grey and black triangles).

A comparison with light-scattering measurements is only possible for the monomer as no LS data for DPG and TPG is found in literature.

4.2.7.2 Neutron scattering

Figure 4.28 shows the frequency dependence of the imaginary part of the susceptibility $\chi''(\nu)$ and the dielectric loss $\varepsilon''(\nu)$ of PG, DPG and TPG as obtained by dielectric spectroscopy and neutron scattering experiments. Latter were performed at the TOFTOF spectrometer at the FRM II in Garching. The measured intensity spectra are related to the imaginary part of the susceptibility by the fluctuation-dissipation theorem.[242] Dielectric results (cf. figure 4.9 for a broader frequency range) are shown as open symbols. For DPG and TPG the same temperatures are displayed, as indicated in frame (b). Susceptibility data are shown as green lines and correspond from top to down to the same temperatures as shown for the dielectric measurements in each frame.

As scattering results usually provide no information on the absolute values of χ'', the data sets have been shifted vertically to yield a comparable height of the boson peak. As mentioned before, there is no rationale for this, but as the frequency range of the neutron scattering data is restricted to frequencies above GHz, it is not possible to scale on the α-relaxation. The peak positions in the neutron scattering experiments occur at lower frequencies compared to the dielectric measurements. The increase towards the boson peak at the high frequency flank of the minimum is nearly the same in both methods and the slope of the of the low frequency wing of the boson peak is similar in all three samples. This is best seen at lower temperatures (232 K - 250 K).

In glycerol, which is chemically very similar to propylene glycol, the situation is different.[1] The minimum positions in the distinct methods indeed differ there too, but the THz peak as determined from light- and neutron scattering experiments is located at the same frequency as in dielectric spectroscopy. In general, the different ratio between α- and boson peak as well as the varying minimum position between the different methods in the susceptibility is explained by considering the different tensorial properties of the experimental probes.[134,137,187,218,240] Nevertheless, there seems to be no straightforward explanation for the difference of the boson peak position and broadness. To our knowledge this was not observed in literature before and further research is necessary to clarify this issue.

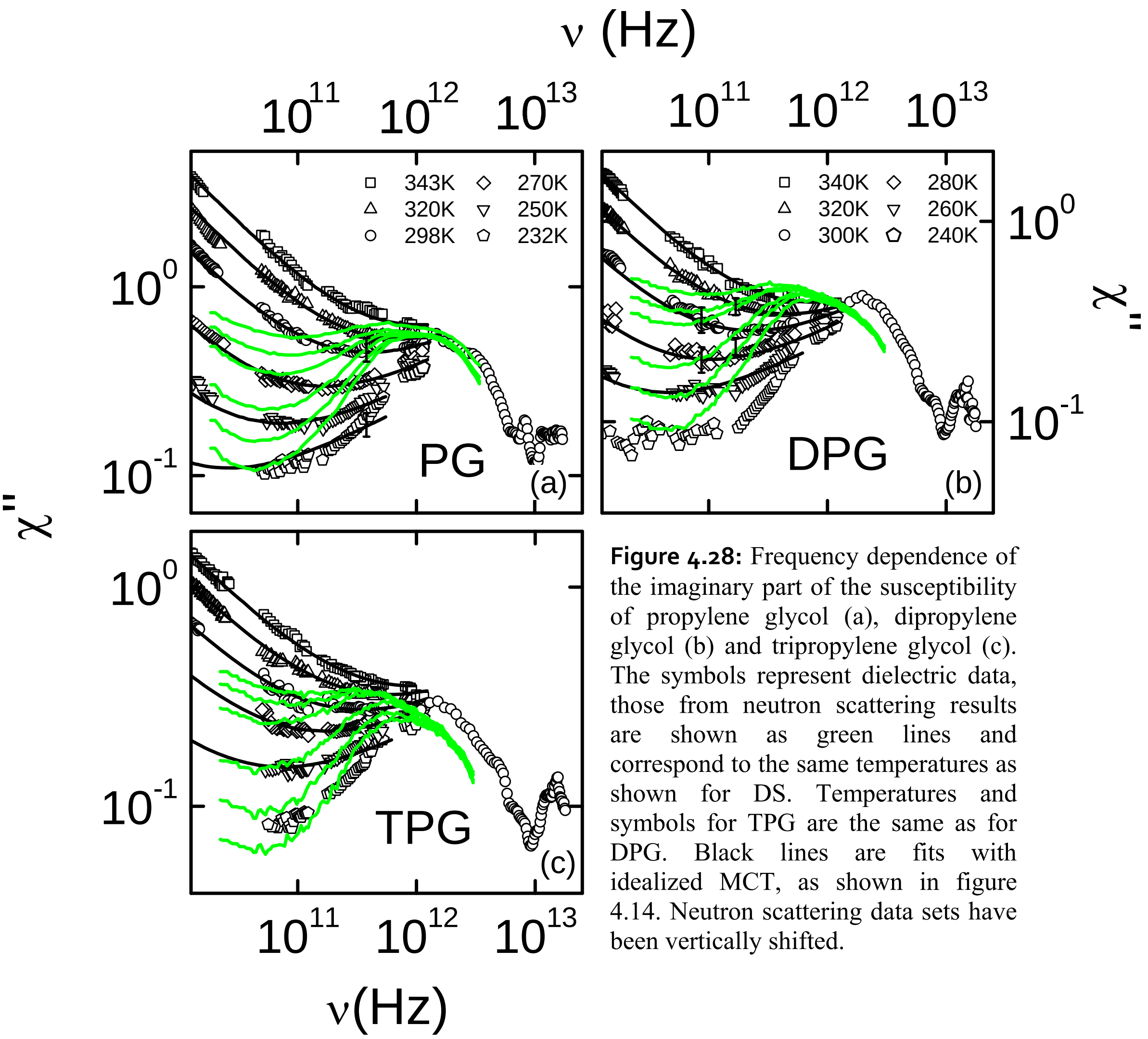

Figure 4.28: Frequency dependence of the imaginary part of the susceptibility of propylene glycol (a), dipropylene glycol (b) and tripropylene glycol (c). The symbols represent dielectric data, those from neutron scattering results are shown as green lines and correspond to the same temperatures as shown for DS. Temperatures and symbols for TPG are the same as for DPG. Black lines are fits with idealized MCT, as shown in figure 4.14. Neutron scattering data sets have been vertically shifted.

In figure 4.29, the susceptibility data of PG, DPG and TPG, as shown in figure 4.28, are scaled on the minimum, χ''/χ_{min} vs. ν/ν_{min}. As the frequency range of the neutron scattering data is limited, it was not possible to perform an analysis in the framework of idealized MCT and to determine minimum position and amplitude as fit parameters. For sake of comparison, the master curves as determined from the dielectric measurements are shown as dashed lines in figures 4.29 (a) - (c) and the neutron scattering minima were just scaled by eye.

It is obvious, that the displayed master curves are way too flat at the high-frequency flank of the minimum. At low frequencies no statement can be made, because of the lack of data. However, in the minimum region, the data seems to scale quite well. The slope towards the boson peak is comparable for the spectra from 232 K - 300 K in all three compounds, but the influence of the boson peak is quite strong. Compared to figure 4.17, the scaling behaviour of the neutron scattering data qualitatively looks different from the dielectric data. It is possible to scale latter on a broader frequency range, and the onset of the boson peak seems to influence the critical law less.

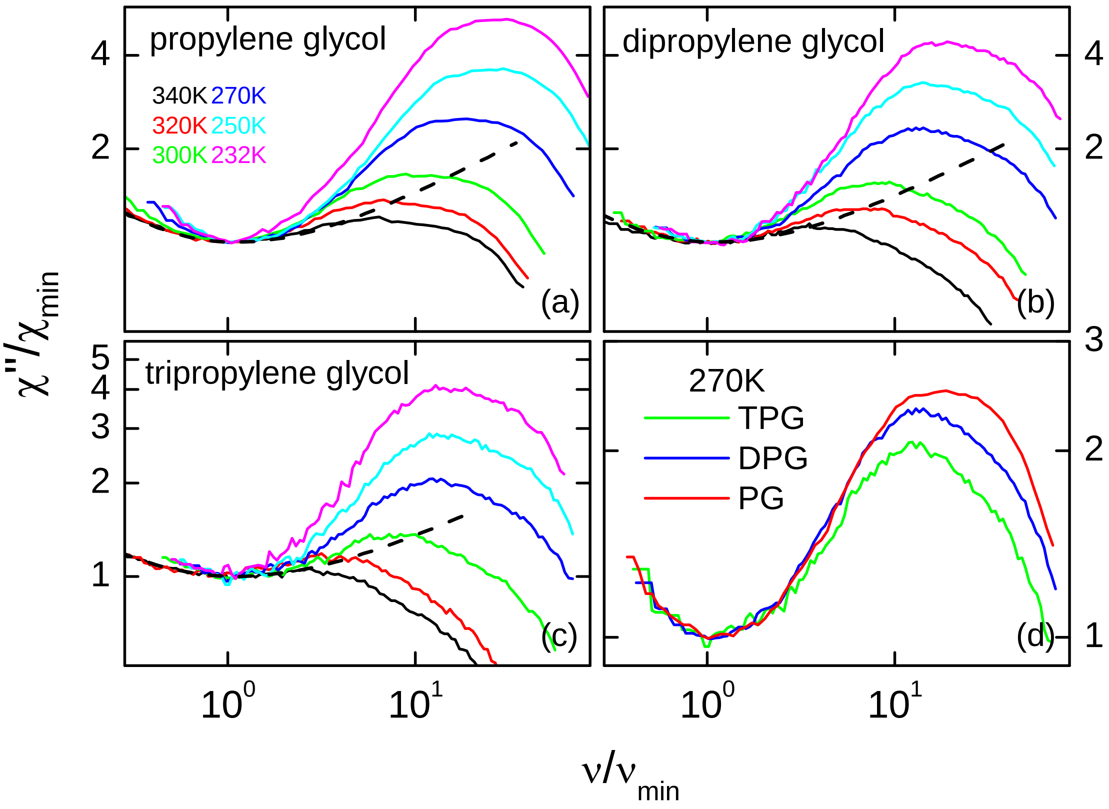

Figure 4.29: Susceptibility data as shown in figure 4.28 scaled on the minimum χ''/χ_{min} vs. ν/ν_{min} for (a) PG, (b) DPG and (c) TPG. Temperatures are indicated in frame (a). In addition the spectra of PG, DPG and TPG are directly compared for 270 K in frame (d).

Figure 4.29 (d) shows the scaled spectra of PG, DPG and TPG at 270 K. Compared to each other, they show an increasing strength of the boson peak with decreasing molecular size. However, the neutron scattering data does not show any broadening of the minimum of the fast β-process. In the framework of MCT this means, that the α-peak position should also be comparable in all three compounds. To check for the behaviour of the α-relaxation further measurements at lower frequencies would be necessary.

4.2.7.3 Positron annihilation lifetime spectroscopy

The PALS technique is based on the annihilation of the so-called ortho-positronium (o-Ps) and is mainly used for free volume characterisation.[172,243] The lifetime τ_3 of the o-Ps is determined by its annihilation with an electron in the sample. In general, the $\tau_3(T)$ curve exhibits a typical quasi-sigmoidal shape, schematically shown in figure 4.30. Recent analysis of small molecular and polymeric glass-formers[172,244,245] revealed the existence of several characteristic PALS temperatures like T_g^{PALS}, T_{b1}^L, and T_{b2}^L, as indicated in figure 4.30 (a).

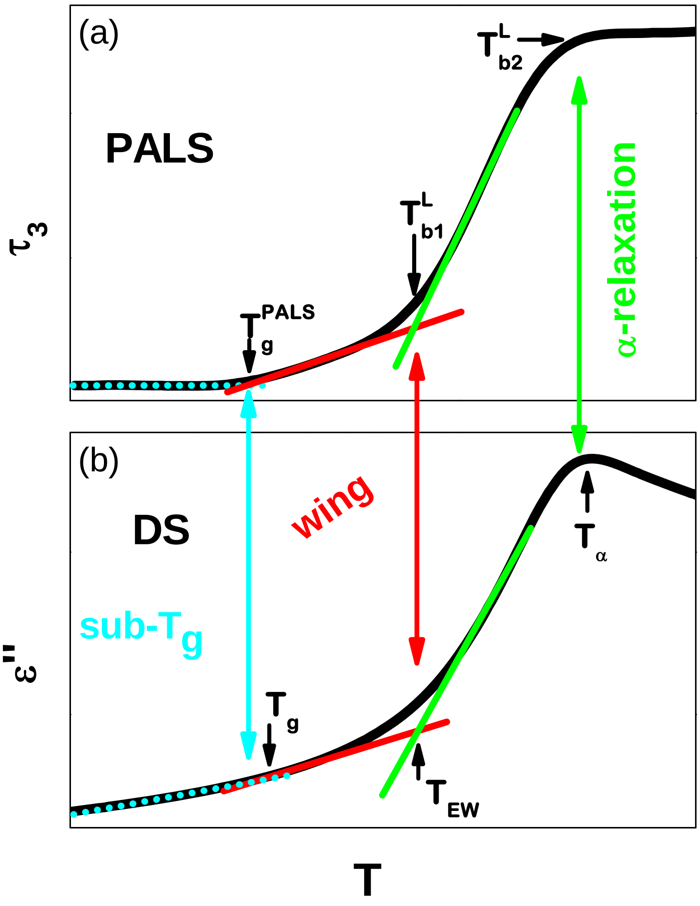

Figure 4.30: Schematic drawing of the typical temperature dependent response from PALS (a) and dielectric spectroscopy (b). The three characteristic PALS temperatures T_g^{PALS}, T_{b1}^L, and T_{b2}^L seem to correspond to T_g, T_{EW}, defining the transition from α- to wing dynamics, and T_α.

Here, T_g^{PALS} denotes the glass-transition temperature probed by the PALS technique. In the $\tau_3(T)$ diagram T_g^{PALS} is situated at the onset of the low temperature plateau. In $\varepsilon''(T)$, T_g is characterized by the transition to a shallower slope at lower temperatures, as the sample falls out of equilibrium at T_g, shown in figure 4.30 (b). The comparison of PALS and BDS measurements of small molecular glass formers like propylene carbonate[246] or glycerol[245] revealed that the glass transition temperatures of both techniques approximately correspond to each other: $T_g^{PALS} \approx T_g$. In figure 4.30, also the other characteristic PALS temperatures are indicated: At T_{b2}^L, τ_3 is often close to the mean α-relaxation time $\langle\tau_\alpha\rangle$ of dielectric spectroscopy, while T_{b1}^L is defined by the change of the slope of the curve between the two plateaus. The temperature corresponding to the α-peak position is labelled as T_α, while the "inflexion" point indicates the crossover from α- to wing-dynamics and therefore is labelled as T_{EW}. However, α- and β-relaxations show a different dynamic behaviour, and the transition between both processes is not always very clear in the $\varepsilon''(T)$ diagram, as the mutual influence sometimes leads only to a slight change of the slope at T_{EW}.

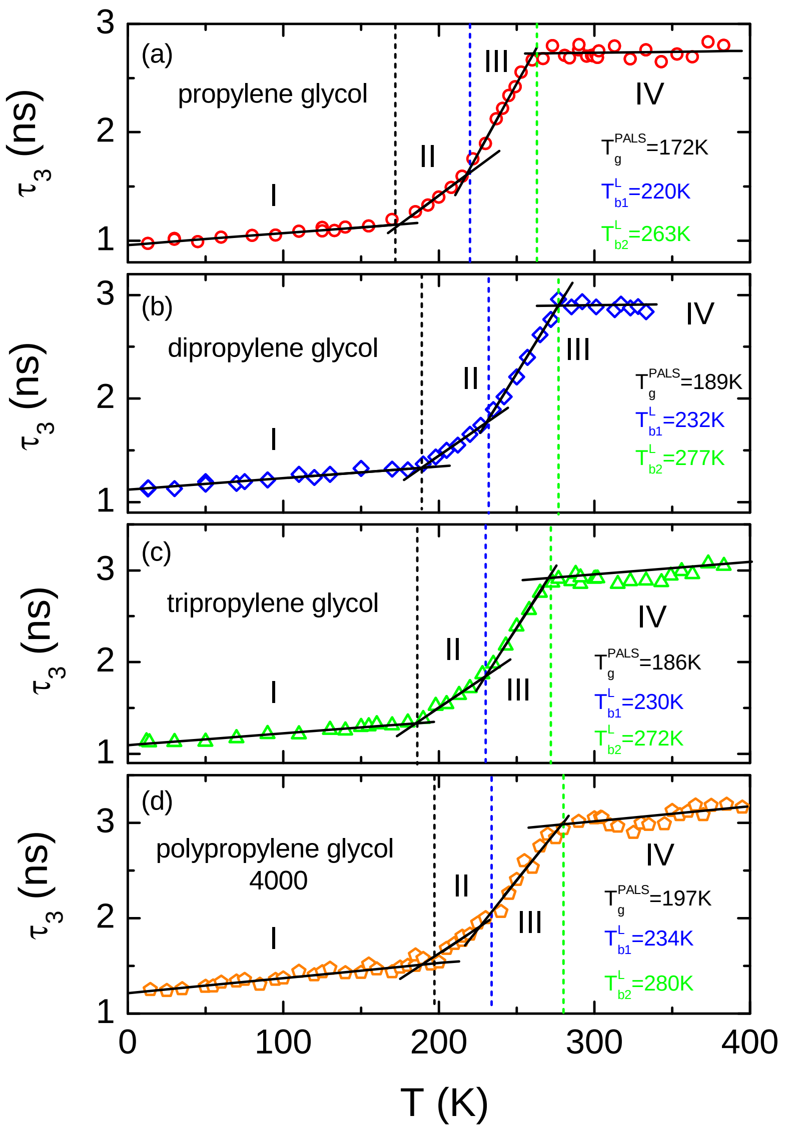

Figure 4.31: o-Ps lifetime τ_3 as a function of temperature for PG (a), DPG (b), TPG (c) and PPG 4000 (d). Solid lines are linear fits, providing the characteristic PALS temperatures T_g^{PALS}, T_{b1}^L, and T_{b2}^L. The PALS measurements were performed at the SAS Polymer Institute in Bratislava by the Bartos group.

Figures 4.31 (a) - (d) display the o-Ps lifetime τ_3 as a function of temperature for PG (a), DPG (b), TPG (c) and PPG 4000 (d) as measured by the Bartos group at the SAS Polymer Institute in Bratislava. For all samples, the typical quasi-sigmoidal curve shape is observed. The onset of the low and high temperature plateau defines the characteristic PALS temperatures T_g^{PALS} and T_{b2}^L as discussed in the last paragraph. Glass transition temperatures are determined to 172, 189, 186 and 197 K, which is in good agreement with transition temperatures determined from DSC and dielectric measurements, provided in table 1.[179] T_{b2}^L is determined to 263, 277, 272 and 280 K ordered by increasing size of the molecular glass formers. From figures 4.31 (a) - (d), T_{b1}^L is determined to 220, 232, 230 and 243 K by the linear fits between both plateau values. In figure 4.31 (d) an additional peak is observed at about 300 K in the high temperature plateau of PPG 4000. This peak probably reflects the normal mode dynamics, a typical feature in Type A[231] polymers. This additional process shows up at frequencies below the α-process and is more pronounced for polymers with a longer backbone chain (cf. section 4.2.6).[233]

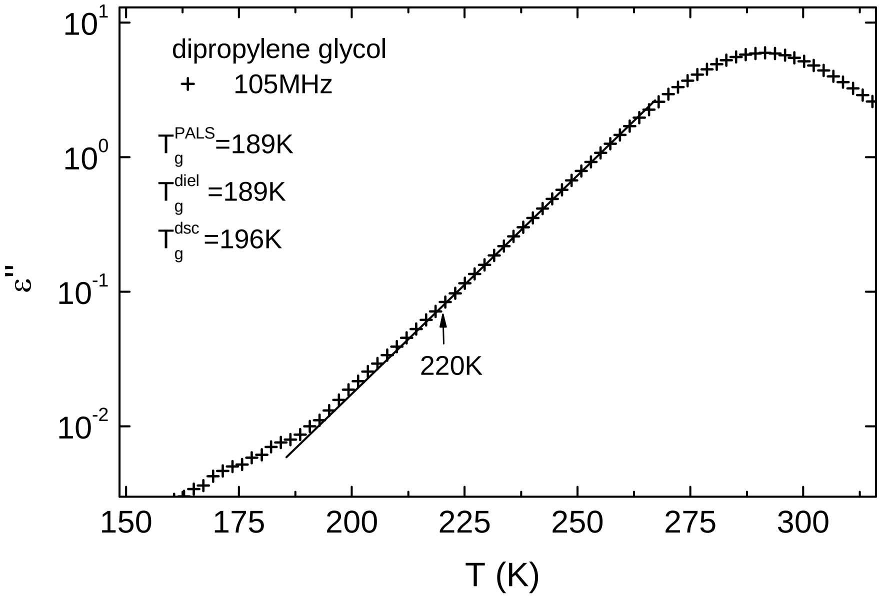

Figure 4.32: Temperature dependent dielectric loss of DPG for 105 MHz. The arrows indicates an onset to a steeper slope at 220 K.

To enable a direct comparison of the dielectric and PALS results, the temperature dependent dielectric loss $\varepsilon''(T)$ is exemplarily plotted for DPG at 105 MHz in figure 4.32. This representation corresponds to a cut at a fixed frequency in figure 4.9. The increase at temperatures beyond the peak in figure 4.32 is due to charge-transport contributions arising from ionic impurities. The characteristic temperatures T_g and T_α, shown schematically in figure 4.30, are determined to 189 K and 290 K. Former corresponds exactly to T_g^{PALS}. For a comparison of T_α to T_{b2}^L, one has to consider that τ_3 varies from about 1 - 3 ns over the whole temperature range. The dielectric spectra for the 105 MHz curve shown in figure 4.32, corresponds to $\tau_3 \approx 1.5$ ns. Indeed, T_α approximately corresponds to T_{b2}^L =277 K. However, from figure 4.32, it is not easy to determine the transition of α- to wing dynamics as the slope of the 105 MHz curve does not significantly change between T_g and T_α. A slight change occurs at $T \approx 220$ K. For a better detection, the solid black line is drawn into the spectrum and the transition temperature is indicated by an arrow. Difficulties to distinguish T_{b1}^L from $\varepsilon''(T)$ may be due to the different dynamic behaviour and the mutual influence of structural and secondary relaxation process. In contrast to propylene carbonate[246] the $\varepsilon''(T)$ representation seems not to be very useful in the case of DPG (nor for the other glycols, not shown here).

To determine T_{b1}^L, it seems better to analyse the behaviour of the dielectric spectra at about 10^8 Hz in the frequency dependent dielectric loss, $\varepsilon''(\nu)$. When looking at the spectra at 10^8 Hz of DPG in figure 4.9 (b), it becomes apparent, that the 280 K and 260 K curves are cut at the α-relaxation. The wing-dynamics set in at the 240 K curve, which then would correspond to the dielectric T_{b1}^L. The transition temperatures determined by both methods roughly agree. Deviations are ascribed to the fact, that it is a simplification to look at one fixed frequency as τ_3 varies from 1-3 ns.

4.3 Influence of the ion content on slow and fast relaxation dynamics

Glycerol is a hydrogen-bonded glass-former, with a melting temperature of $T_m = 291$ K and a calorimetric glass-transition at $T_g = 185$ K. In the "strong-fragile" classification scheme introduced by Angell and co-workers[247] it is characterized, with a fragility parameter of $m = 53$,[248] as intermediate. In the following section, a thorough characterisation of glass-forming glycerol with varying concentrations of LiCl is presented. Information on the dc-conductivity, the dielectric relaxation time (from the dielectric loss) and the conductivity relaxation time (from the dielectric modulus) is provided.[249] However, for the present work mainly the measurements above 3 GHz have been performed. The low frequency data have been analysed in Ref. 250. Therefore I will concentrate on the high frequency behaviour and discuss the influence of the increasing ion concentration in the high frequency regime of the fast β-process and the boson peak in detail. In addition, the results of neutron scattering experiments, performed at the time-of-flight spectrometer TOFTOF in Garching, are presented and discussed.

4.3.1 The α-relaxation

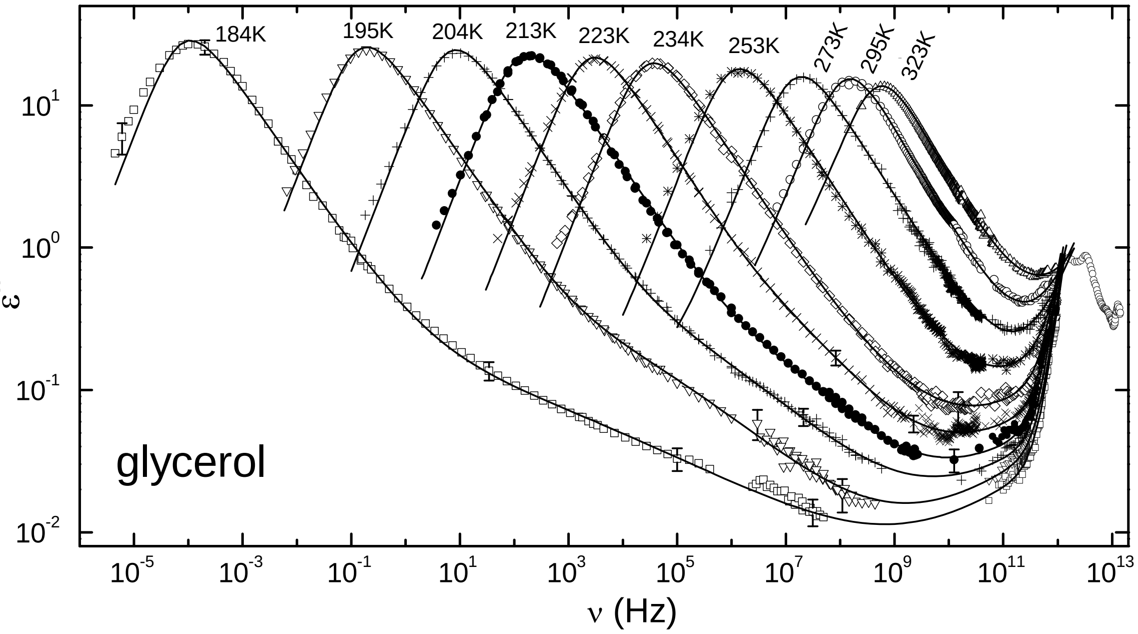

Figure 4.33: Frequency dependent dielectric loss of glycerol for selected temperatures.[1] The solid lines are fits with the sum of a CD function, accounting for the α-peak, and a CC function for the wing and the term $\varepsilon_c + c_3\nu^{0.3} + c_n\nu^n$. Taken from Ref. 1.

Figure 4.33 shows the frequency-dependent dielectric loss, $\varepsilon''(\nu)$, of glycerol[1] for various selected temperatures in the whole frequency range investigated. Glycerol shows a very low crystallization tendency and is one of the most thoroughly investigated glass-forming materials.[38,39,53,54,251–253] The strong temperature dependent shift of the asymmetrically shaped α-peak mirrors the continuous slow down of the molecular dynamics when approaching the glass transition. At frequencies beyond the α-relaxation peak, $\nu > \nu_\alpha$, the dielectric loss follows a power law $\varepsilon'' \sim \nu^{-\beta}$. For $T > 253$ K a smooth transition into the high-frequency minimum is observed. To lower temperatures an additional, shallower power law, ν^{-b}, the so-called excess wing, shows up, with $b < \beta$. With increasing temperature, b increases and merges with the α-peak at 273 K. The minimum showing up in the GHz - THz region of the dielectric loss becomes significantly broader with decreasing temperature and its amplitude and frequency position decreases, too. In the infrared region the minimum is followed by the so-called boson peak (in figure 4.33 shown exemplarily only for one temperature). For the parameterisation of the α-relaxation peak often the Fourier transform of the Kohlrausch-Williams-Watts (KWW) function, equation (2.5), or the Cole-Davidson (CD) function, equation (2.4) are applied. The solid lines in figure 4.33 show fits with a sum of a CD function for the α-peak and a CC function for the excess wing. To account for the minimum and the increase towards the boson peak, a constant loss contribution and two power laws, $\nu^{0.3}$ and ν^n with $n \geq 1$, were added to: $\varepsilon'' = CD + CC + \varepsilon_c + c_3\nu^{0.3} + c_n\nu^n$.[1] More details on glycerol are found, e.g., in Refs. 1, 51, 54, 113, 141, 218 and 254 - 256.

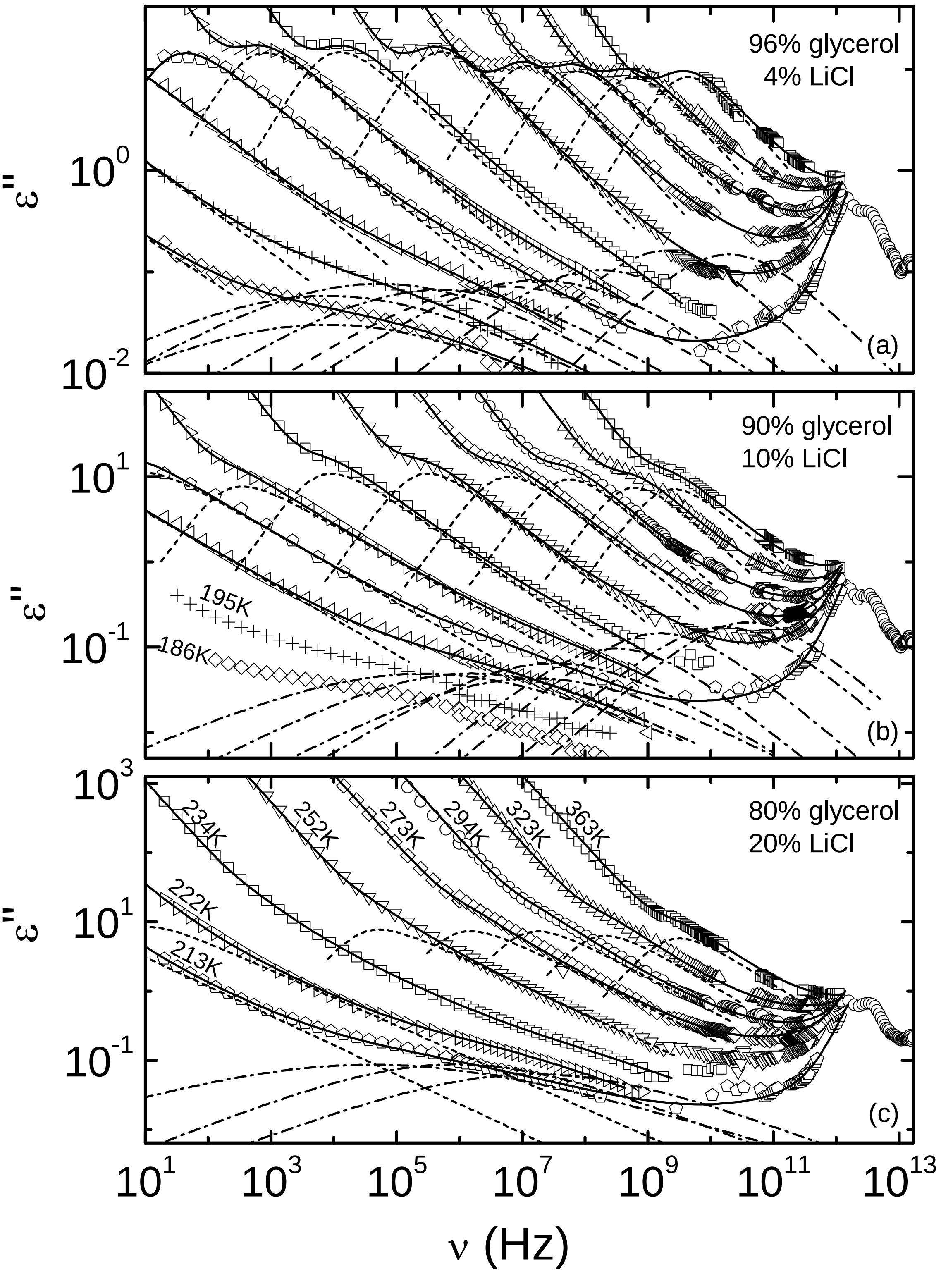

Figure 4.34: Frequency dependent dielectric loss $\varepsilon''(\nu)$ of glycerol with (a) 4, (b) 10 and (c) 20 mol% LiCl at various temperatures. The temperatures in (a) and (b) are the same as indicated for the corresponding curves in (c). Solid lines are fits with equation (4.3). Dashed lines show the CD, dash-dotted lines the CC contribution. The measurements above 3 GHz have been performed for the present work.

Figures 4.34 (a) – (c) show the frequency dependent dielectric loss $\varepsilon''(\nu)$ for glycerol with ion contents of (a) 4, (b) 10 and (c) 20 mol % LiCl for various temperatures up to THz frequencies. The spectra of glass-forming glycerol with 4 and 10 mol% LiCl ions look quite similar to that of pure glycerol. The α-peak shifts by more than 10 decades of frequency by changing the temperature by about a factor of two. At frequencies beyond the structural relaxation, also a second, shallower power law shows up, identified as excess wing. At higher frequencies and temperatures this excess wing seems to have merged with the dominating α-relaxation peak before the minimum is reached.

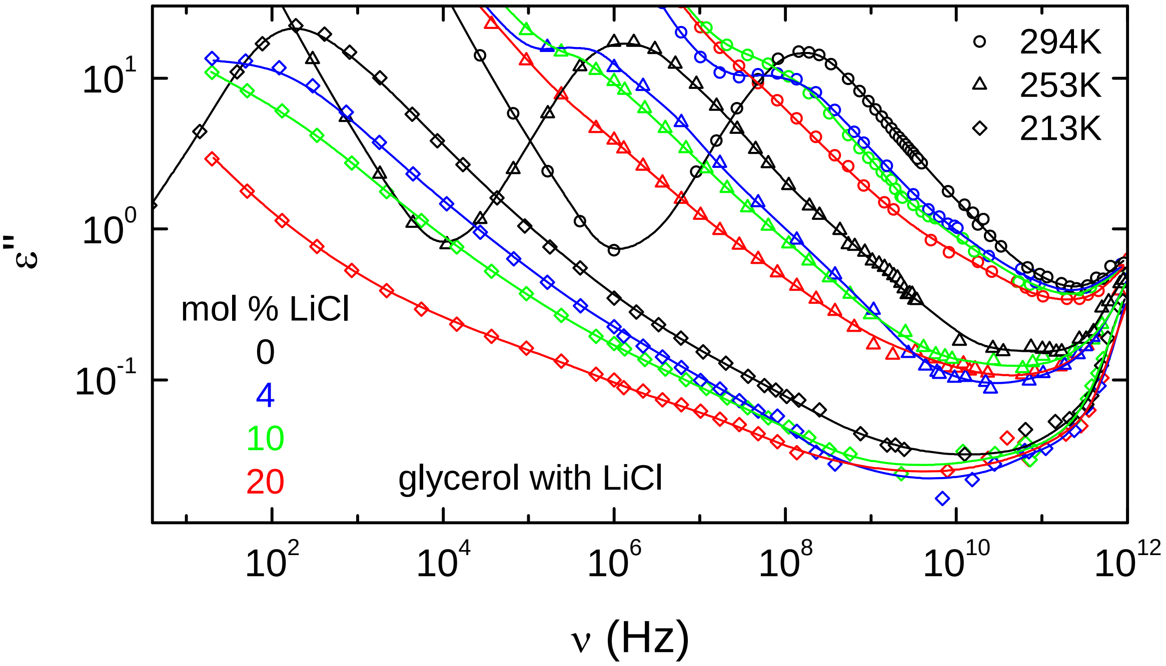

Figure 4.35: Broadband dielectric loss $\varepsilon''(\nu)$ for pure glycerol[48] and three glycerol samples, doped with different contents of LiCl (4, 10 and 20 mol%) for 295 K, 253 K and 213 K. Lines are to guide the eyes. To keep track of the data, not all points are shown.

With increasing ion content in the sample, the α-relaxation peak gets more and more dominated by the dc-conductivity, as seen at the low frequency side of the α-process, this gets even clearer in figure 4.35. Here, spectra for three selected temperatures, already shown in figures 4.33 and 4.34 (a) – (c) are compared. The ion content of the shown mixtures was chosen as 4, 10 and 20 mol%. Regarding the spectra of each sample, the α-relaxation peak shifts to higher frequencies with increasing temperature. This typical behaviour of glass-forming matter is especially revealed in pure glycerol and the slightly doped 4 mol% LiCl sample. The increase of the conductivity contribution especially gets visible in the higher doped 10 and 20 mol% LiCl in glycerol samples. While in former the α-peak position is still easily distinguishable, latter seems totally dominated by the conductivity contribution. The increasing ion content has a tremendous influence on the α-

relaxation dynamics, as it leads to a significant slowing down. While the structural relaxation, connected mainly with the reorientation of the dipoles, shows similar dynamic behaviour at high frequencies, the low frequency response differs enormously. Because of the immense shift to lower frequencies with lower temperatures and higher concentrations, the excess wing gets more pronounced. Interestingly, the high-frequency response seems less influenced by the increase of LiCl ions in the sample. Minimum position and amplitude, ν_{min} and ε_{min}, at a first glance seem to be comparable at least in the 295 K curves. To lower temperatures the minimum seems to broaden with increasing ion content of the sample, which is understood as a consequence of the strong shift to lower frequencies of the α-relaxation peak. The conductivity contributions as observed in figures 4.34 and 4.35 are assumed to be frequency-independent, $\sigma(\nu) = \sigma_{dc}$, and expected to behave as $\varepsilon'' \sim \sigma_{dc}/\nu$ in the dielectric loss. Figure 4.36 exemplarily shows the 363 K curve for 96 mol% glycerol with 4 mol% LiCl in more detail. At low frequencies (below 10^4 Hz) a change in the slope to a weaker frequency dependence than $1/\nu$ occurs. Such behaviour accounts for the effect of blocking electrodes meaning the formation of a space charge close to the sample surface, due to the fact that the ions cannot penetrate the metallic electrode plates.[257] The increase of the slope at even lower frequencies may be due to the fact, that two different types of ions, namely Li^+ and Cl^-, are in the sample. Probably, the bigger and more immobile Cl^- ions show blocking electrode effects at lower frequencies, due to their slower diffusion. The effect of blocking electrodes generally arises at very low frequencies if the quantity of ions is high enough. Electrode polarization effects lead also to huge values of ε'. As they provide no further information, they are not shown in the present work.

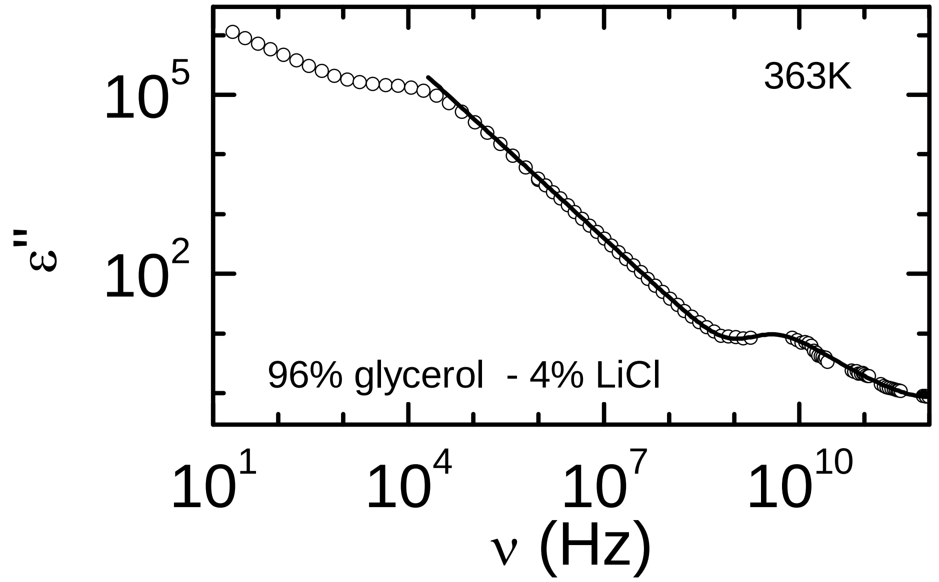

Figure 4.36: Frequency dependent dielectric loss in 96% glycerol with 4% LiCl at 363 K. Towards low frequencies the conductivity contribution $\varepsilon'' \propto \sigma'/\nu$ is seen. Below 10^4 Hz a transition to a weaker frequency dependence, due to the effect of blocking electrodes, is observed.

The α-peak position, can be identified by two different ways. First one is to subtract the conductivity contribution from the spectra, leading to the appearance of a clear α-relaxation peak, or secondly, to fit the $\varepsilon'(\nu)$ spectra first, as the conductivity does not contribute in the real part of the dielectric permittivity, and perform the $\varepsilon''(\nu)$ fits with the obtained parameters. However, both methods lead to coinciding results, but first way of data analysis seems to be the method of choice as it seems to be more straightforward. After considering the influence of the conductivity contribution, the spectra are treated in the same way as described for the glycerol sample with 4 mol% LiCl.

For the parameterisation of the $\varepsilon''(\nu)$ spectra in figures 4.34 (a) – (c), an additive superposition of different contributions to the dielectric loss is chosen. For the α-relaxation peak the CD function is applied, while for the excess wing the symmetrically broadened CC function is used (cf. equation (2.4)). The conductivity contribution is taken into account by $\sigma_{dc}/2\pi\nu\varepsilon_0$. For the high-frequency region, an additional constant loss term and two power laws with $\nu^{0.3}$ and ν^n are added, to take account of the minimum and the increase towards the boson peak. The exponent n is restricted to $n \geq 1$. Due to the steep increase towards the boson peak was always chosen as $n = 2$. Then one arrives at:

$$\varepsilon''(\nu) = \frac{\sigma_{dc}}{2\pi\nu\varepsilon_0} + CD + CC + c_n\nu^{\,n} + \varepsilon_c + c_3\nu^{0.3} \tag{4.3}$$

Due to the large number of parameters, it is not astonishing that this ansatz can give a good parameterization of the data. Especially the amplitude and position of the CC peak, can be shifted nearly arbitrarily. In addition, is it not clear, if a simple additive superposition of the different contributions is justified or if an alternative multiplicative ansatz is better suited.[124,185,186]

The dielectric loss of the glycerol samples, doped with 10 and 20 mol% LiCl, shown in figures 4.34 (b) - (c), is dominated by the conductivity contributions of the ions. Therefore, information on the α-relaxation is not directly accessible. To overcome this problem the modulus representation for ionic conductors was introduced by Macedo *et al.*[258] The complex modulus M^* is defined as the inverse of the dielectric permittivity $M^* = 1/\varepsilon^*$. Electrode and conductivity contributions are strongly suppressed in this representation and it is commonly applied to obtain information about the charge carrier dynamics in ionic conductors. The applicability and correct evaluation of the dielectric modulus still is controversially debated.[56,259–263] Nevertheless, it appears as a good tool for data analysis,[249] as it seems to be a good measure of the ionic dynamics and as it gives direct access to the translational dynamics determining the glass transition.

Figures 4.37 (a) - (c) show the frequency dependent imaginary part $M''(\nu)$ of glass forming glycerol with 4, 10 and 20 mol% LiCl, over a temperature range from 204 - 363 K. In contrast to the dielectric loss spectra, two peaks are observed. It is well known, that a relaxation peak in $\varepsilon''(\nu)$ also leads to a relaxation peak in $M''(\nu)$, significantly shifted to higher frequencies.[264–266] So, the high-frequency M''-peak is identified with the dipolar α-relaxation. The additional weaker peak, showing up at lower frequencies is ascribed to the translational ion dynamics and thus mirrors the conductivity relaxation of the mobile ions. To account for the different relaxation times, the one of the low frequency peak in $M''(\nu)$ is labelled τ_σ while the other one is labeled τ_R.[258] In the following, the α-relaxation times as determined from $\varepsilon''(\nu)$ are denoted as τ_ε.

The dielectric modulus spectra of pure glycerol and mixtures with different concentrations of LiCl have been fitted and analysed in detail.[249] For this, a sum of a CD[38,39] and a HN[36] function was used:

$$\begin{aligned} M^* = M_{\infty,CD}\left[1-\frac{1}{(1+2\pi i\nu\tau_\sigma)^{\beta}}\right] \\ + M_{\infty,HN}\left[1-\frac{1}{[(1+2\pi i\nu\tau_R)^{1-\alpha_{HN}}]^{\beta_{HN}}}\right] \end{aligned} \tag{4.4}$$

$M_{\infty,CD}$ and $M_{\infty,HN}$ denote the amplitudes of both contributions while τ_σ and τ_R are the relaxation times. α_{HN} and β_{HN} are the width parameters characterizing symmetrical and asymmetrical peak broadening of the HN function, respectively.[36] Fits of the real and imaginary part were simultaneously performed but real parts are not shown, as they provide no significant additional information. The fits of the imaginary parts are shown a solid lines in figures 4.37 (a) - (c) and provide a reasonable description of the data.

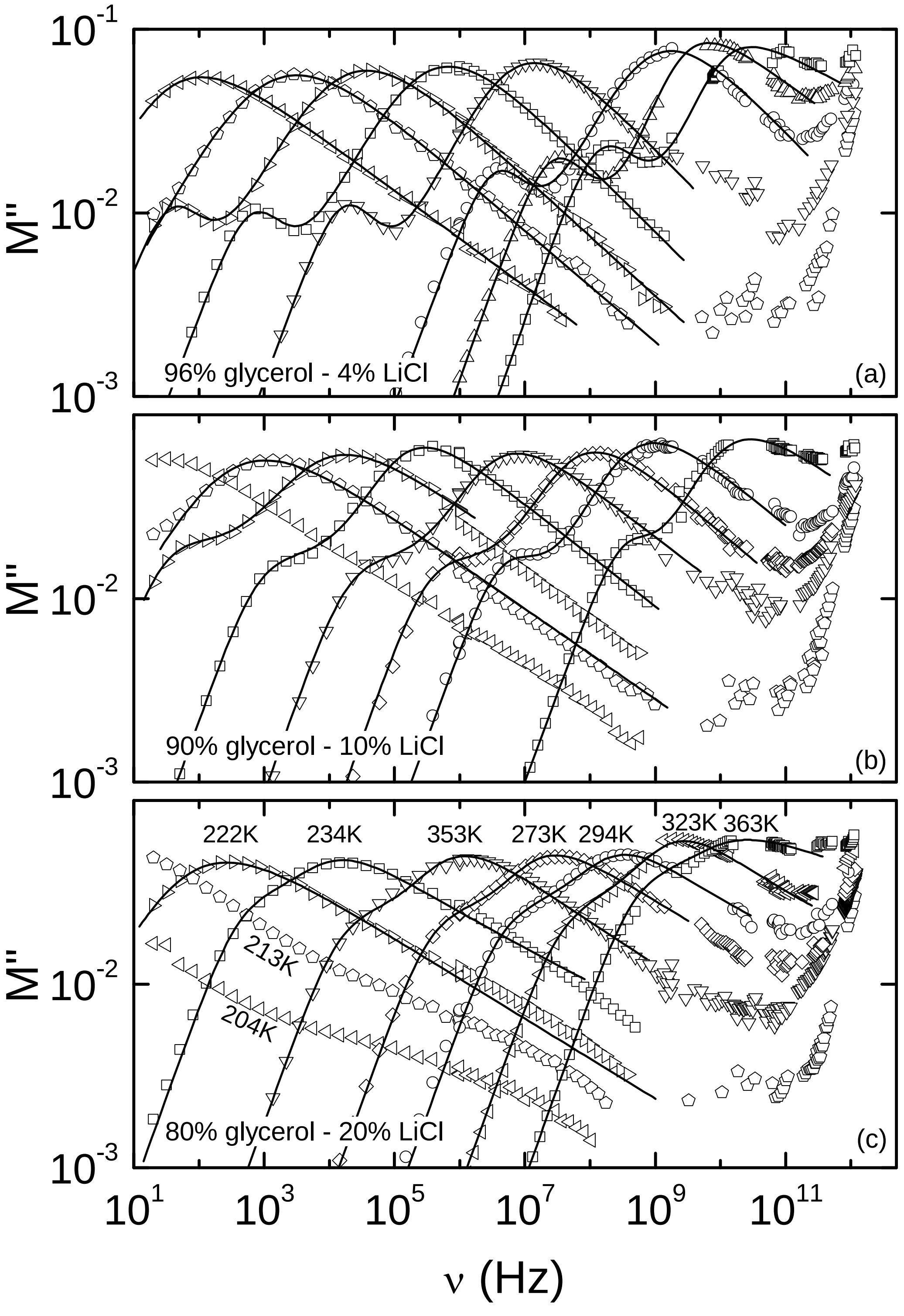

Figure 4.37: Frequency dependent dielectric modulus M'' in glycerol with (a) 4, (b) 10 and (c) 20 mol% LiCl at various temperatures. The temperatures in (a) and (b) are the same as indicated for the corresponding curves in (c). Solid lines are fits with equation (4.4). Low frequency data is partly published in Ref. 249.

A comparison of the imaginary part of the dielectric permittivity $\varepsilon''(\nu)$ and the dielectric modulus $M''(\nu)$ in glycerol for various LiCl concentrations at 234 K is shown in figures 4.38 (a) and (b) at 234 K. Solid lines are fits with the first two terms of equation (4.3) for $\varepsilon''(\nu)$ and equation (4.4) for $M''(\nu)$. The dipolar α-relaxation peak in $\varepsilon''(\nu)$ is clearly seen in figure 4.38 (a) for pure glycerol. The low frequency part shows, due to impurities in the sample, an increase in the conductivity. For higher ion concentrations an increase of the conductivity is observed while the peak position shifts to lower frequencies. However, the 20% LiCl sample deviates from this behaviour. The conductivity strongly decreases and the α-relaxation peak is hidden under the dominating dc-conductivity. In figure 4.38 (b), $M''(\nu)$ is shown for the same concentrations at 234 K. In pure glycerol only one peak is visible in the presented frequency window, while in all mixtures two peaks appear. The high frequency peak is ascribed to the α-relaxation while the low frequency peak is due to the translational motions of the ions. With increasing ion content both peaks approach each other and are nearly merged for the sample with 20% LiCl. The shifting of the high frequency peak with increasing ion content implies that the reorientational relaxation process is strongly influenced by the ions.

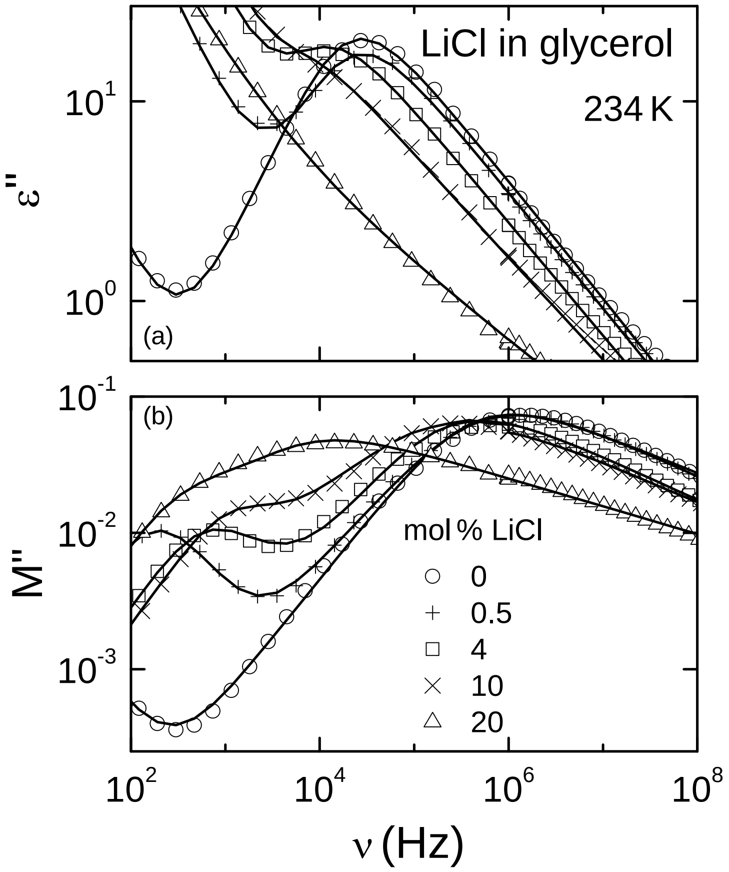

Figure 4.38: Frequency dependent dielectric loss $\varepsilon''(\nu)$ (a) and dielectric modulus $M''(\nu)$ (b) for various LiCl concentrations in glycerol at 234 K. The lines are fits with the first two terms from equation (4.3) for $\varepsilon''(\nu)$ and equation (4.4) for $M''(\nu)$. Taken from Ref. 249.

Figures 4.39 (a) and (b) show the conductivity relaxation times τ_σ and dipolar α-relaxation times τ_ε for different LiCl concentrations in glycerol in Arrhenius representation. Solid lines are fits using the VFT law, equation (2.6).

Figure 4.39 (a) reveals a decrease of τ_σ with increasing ion content. For ion concentrations of $x > 5\%$ saturation is observed. Only at low temperatures this behaviour reverses for $x = 20\%$ and the relaxation times seem to increase again. This is in agreement with Howell *et al.*[264] However, there is no simple argument why the ion dynamics should become faster again with increasing ion density. This may be explained by the modulus formalism as τ_σ (and σ_{dc}, as $\tau_\sigma \sim 1/\sigma_{dc}$) is dependent on the ion mobility and on the ion density.[258,264] The details of this questions are out of the scope of this work and the interested reader is referred to Ref. 249 and to the many papers dealing with the applicability of the modulus formalism.[56,259–263]

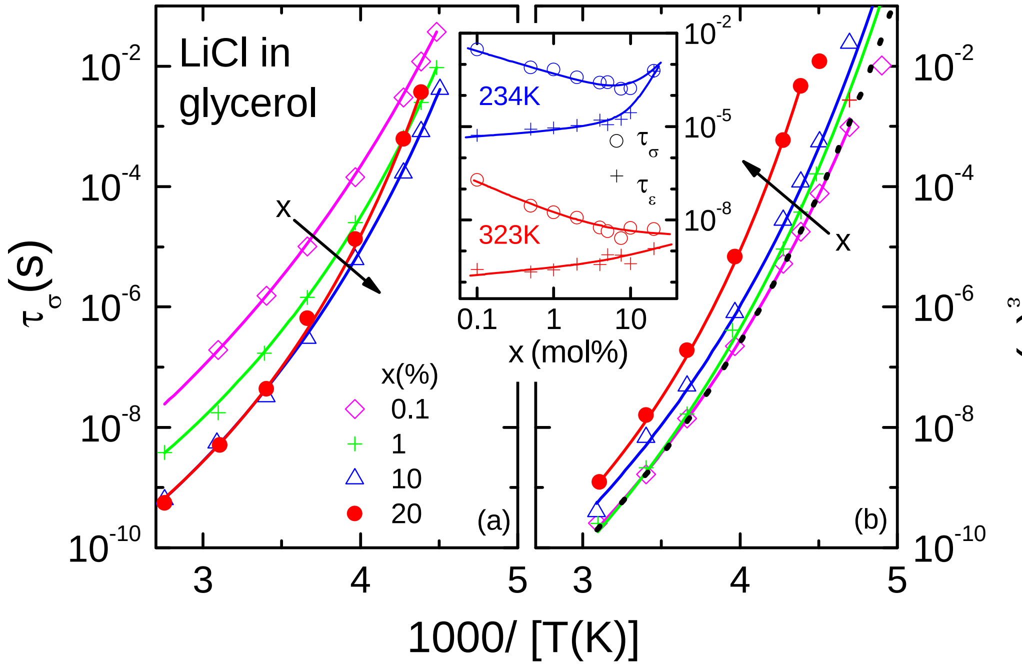

Figure 4.39: Conductivity relaxation times τ_σ (a) and dipolar α-relaxation times τ_ε (b) in Arrhenius representation for selected LiCl concentrations in glycerol. The fits, represented by the solid lines, were performed using a VFT law. The dotted line in (b) corresponds to literature data for pure glycerol.[3] The dependence of both relaxation times on the LiCl concentration for 234 K and 323 K is shown in the inset. The lines are to guide the eyes.[249]

Figure 4.39 (b) shows the α-relaxation times τ_ε.[249] For low LiCl concentrations the relaxation times agree quite well to the relaxation times of pure glycerol[3] (dotted line). Relaxation times for all concentrations are described with the phenomenological VFT law. Up to $x = 10\%$ the relaxation times shift quite parallel to the ones of pure glycerol. Interestingly, it should be noticed that in aqueous solutions of various salts, at relatively low ion concentrations an acceleration of the relaxation for increasing ion content is observed (the opposite behaviour as here).[267–269] At 20 mol% LiCl the relaxation times increase significantly stronger than for the lower concentrations. This again is in agreement with the findings of Howell *et al.*[264] The stronger curvature of the $\tau(T^{-1})$ curve accounts for a higher fragility compared to the other curves representing high ion concentrations. Due to a stronger coupling at high concentrations an increase of cooperativity may play a role.

The behaviour of dipolar and conductivity relaxation times in dependence of the concentration is shown in the inset of figure 4.39 for two selected temperatures. The convergence of time scales of both relaxation times at high ion concentrations implies a strong coupling of translational and reorientational motions. It is important to note at this point, that the dipolar relaxation times of pure glycerol, as determined by dielectric spectroscopy, agree with the results obtained by other measurement techniques.[61,234–236,270] This gives evidence for the direct coupling of the reorientational molecular dynamics to the translational dynamics that determines the glass transition. From the present results, it is possible to conclude, that the ionic motion becomes increasingly coupled to the structural relaxation dynamics for high ion concentrations.

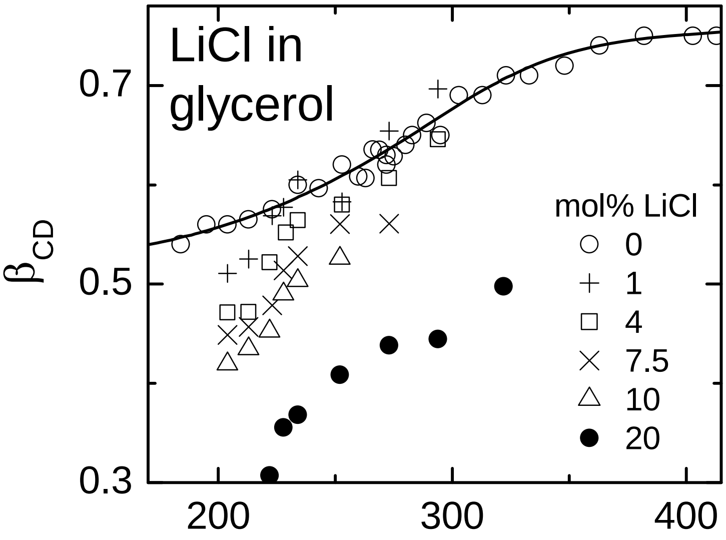

Figure 4.40: Width parameter $\beta_{CD}(T)$ as determined from the CD fits of the dielectric loss spectra for selected concentrations. Points are only shown where sufficient significant information can be provided. Especially at high temperatures this is not the case as the superposition by the conductivity makes a determination of β_{CD} difficult. The values for pure glycerol are taken from Ref. 22. The solid line is just to guide the eye.[249]

The width parameter $\beta_{CD}(T)$, as obtained from the fits, is provided for selected ion concentrations in figure 4.40. It is well known from literature,[3,22] that for pure glycerol β_{CD} increases with increasing temperature and saturates below unity, as shown in figure 4.40 by the circles. At low temperatures it approaches a value of 0.5, consistent with the proposed universal exponent of $\beta = 0.5$ of the high frequency flank of the α-relaxation peak.[271] The line is to guide the eyes.

The width parameters for the binary mixtures are lower then in the pure sample. As before, an increase of β_{CD} with temperature is observed. Approaching T_g, the absolute values are remarkably smaller than in the pure material. The decrease of the width parameter accounts for the broadening of the α-relaxation peak and is commonly ascribed to a disorder-induced distribution of relaxation times in glassy matter.[92,93] In connection with our results one can conclude, that the statistical distribution of the ions which are strongly interacting with the dipoles should lead to a broadening of the α-peak. Indications for such behaviour were also found in earlier works.[264,272]

4.3.2 *Slow β-process and excess wing*

Figure 4.41 shows the frequency dependent dielectric loss in glycerol for various LiCl concentrations. In figure 4.41 (a), the α-peak position for every curve shown, is situated at 48 Hz (a), in frame (b) at 16.5 Hz and in (c) at 450 kHz. This is done to account for the same α-relaxation dynamic in each sample. As the α-peak position strongly shifts to lower frequencies with increasing ion content, this implies that measurements at different temperatures are compared in each frame.

While the spectra for glycerol with small LiCl content closely resemble those for pure glycerol in the region of the excess wing, the spectra change with higher ion content (10 and 20 mol% LiCl). The strength of the excess wing increases with increasing ion content.

By using ultrahigh pressures up to 6 GPa, Pronin *et al.*[273] recently showed for pure glycerol that a significant secondary relaxation peak, identified as JG peak, emerges in the dielectric loss of glycerol at pressures higher than 3 GPa. They explain this by an eventual braking of the hydrogen bonds under high pressure. For this reason, they speculate about a stronger coupling of the molecules, which should lead to an increase of the coupling parameter n in the framework of the coupling model.[55] This explanation may also hold for the addition of LiCl ions to glycerol. Here, the ions are supposed to break the hydrogen bonds. These findings are in accord with the decrease of the width parameter β_{CD} with the increasing ion concentration, shown in figure 4.40. This implies an increase of the coupling parameter $n = 1 - \beta_{KWW}$ as the relation

$$\beta_{KWW} = \beta_{CD}^{1/1.23} \tag{4.5}$$

holds.[274] The behaviour described in Ref. 273, is assumed to be consistent with the observed increase of the fragility, which should be larger for hard-sphere like glass formers. In a forthcoming section a general trend of an increase of the fragility with increasing ion content of the binary glycerol mixtures will be discussed.

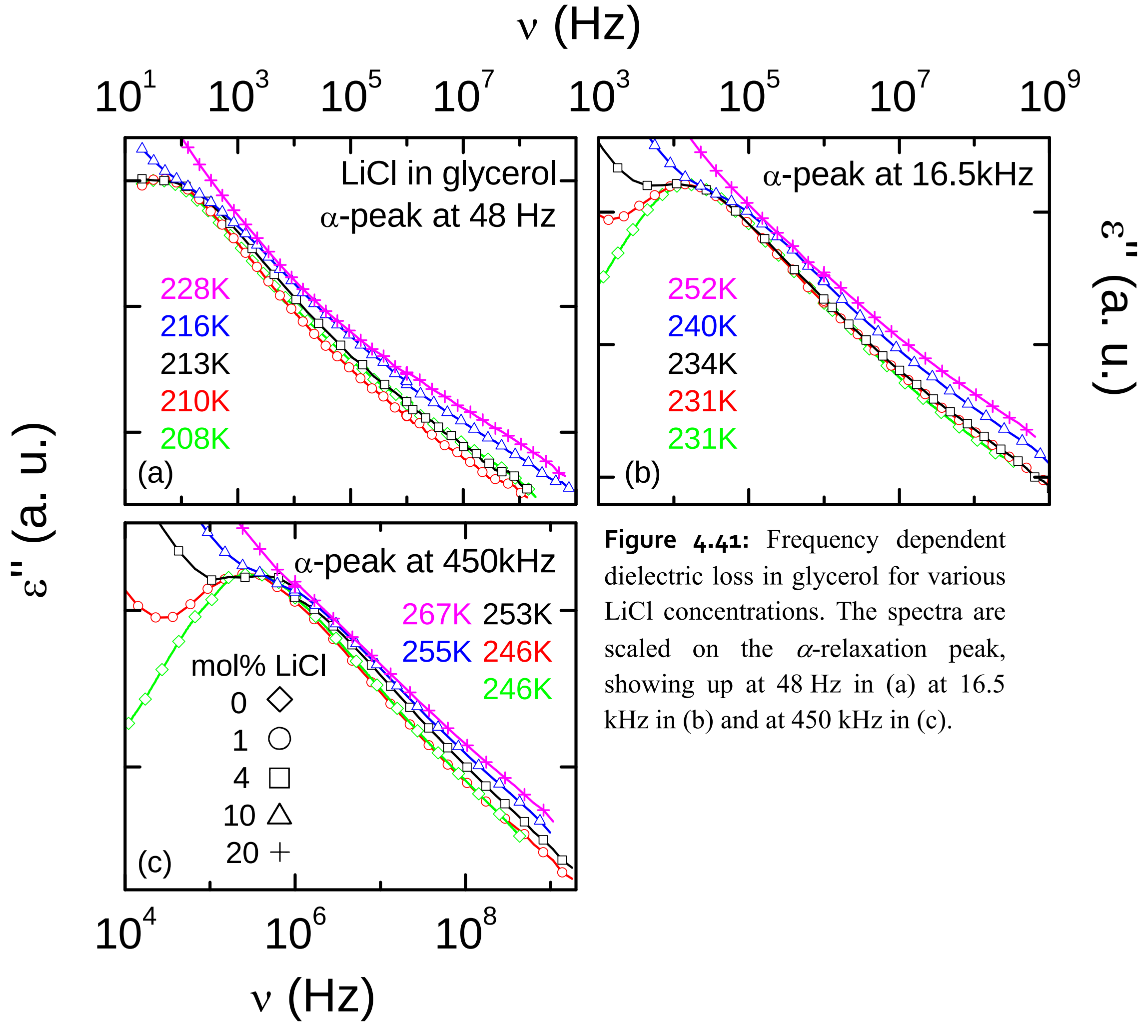

Figure 4.41: Frequency dependent dielectric loss in glycerol for various LiCl concentrations. The spectra are scaled on the *α*-relaxation peak, showing up at 48 Hz in (a) at 16.5 kHz in (b) and at 450 kHz in (c).

4.3.3 High frequency response

4.3.3.1 A mode-coupling analysis

As mentioned before, the main outcome of MCT is the prediction of non-trivial contributions in the minimum region between α-relaxation and boson peak. To check for the existence of intensity, arising in excess to a simple additive superposition of both peaks, a model free check done: Fits with a sum of two simple power laws, accounting for the crossover from the α-relaxation to the boson peak, are performed. For the increase towards the boson peak, the smallest possible exponent $n = 1$[112] is chosen. The fits are shown as dashed lines in the insets of figures 4.42 (a) - (d). One representative temperature (273 K) was exemplarily chosen for glycerol (a) and three mixtures, figures with 4 (b), 10 (c) and 20 mol % (d) LiCl, respectively. They reveal that the $\varepsilon''(\nu)$ minimum in all cases is too shallow to be explained in such simple manner. Larger values of n lead to even worse results. This proves, independently from any model assumptions, the contribution of additional fast processes to the high-frequency dynamics of glass-forming matter.

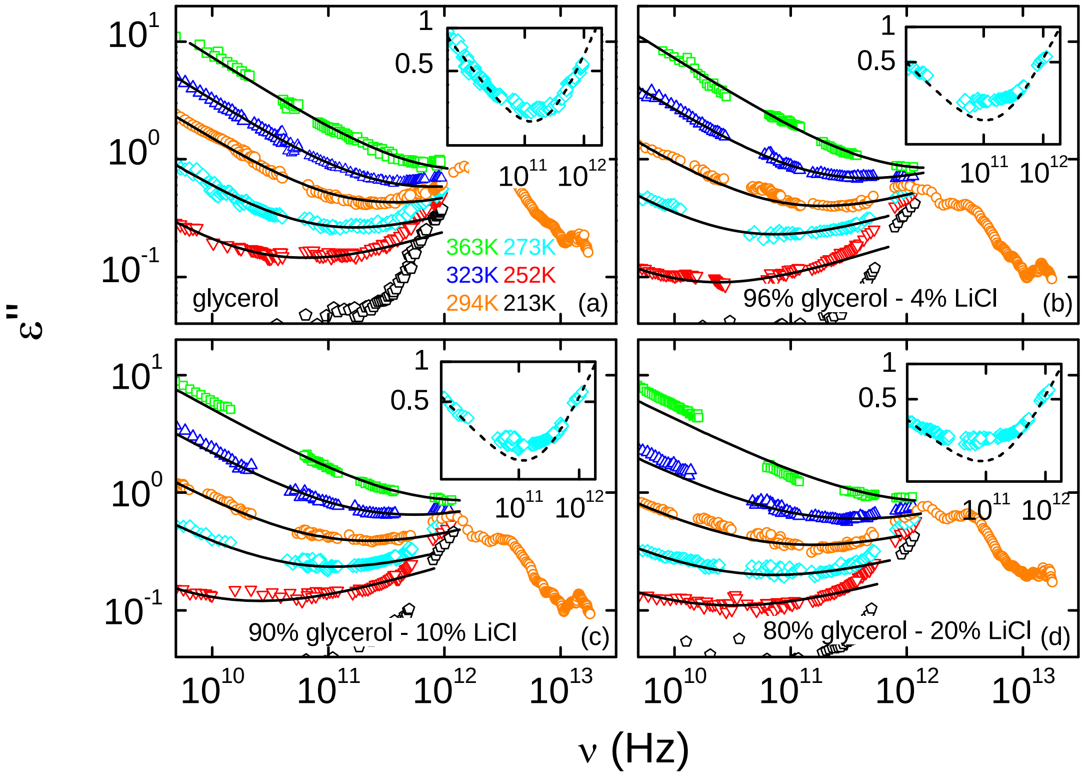

Figure 4.42: Dielectric loss spectra of three different glycerol-LiCl mixtures (b) - (d) and pure glycerol (a) in the high frequency regime. The lines are fits with equation (2.20), using identical parameters a and b for all temperatures of one concentration. The evolution of the exponent parameters with concentration is shown in detail in figure 4.43. The dashed lines in the insets are fits with the sum of two power laws, each one accounting for one flank of the minimum to prove the existence of excess intensity.

Now for a consistent description of the dielectric loss minima in the framework of idealized MCT is checked. Figures 4.42 (a) - (d) in detail show the high-frequency region of the dielectric loss of glycerol (a) and the three representative glycerol - LiCl mixtures with 4, 10 and 20 mol% LiCl, (b) - (d), respectively. The same symbols always correspond to the same temperatures as indicated in frame (a). Solid lines in figures 4.42 (a) - (d) show the fits as obtained by the application of the simple interpolation formula, equation (2.20), of idealized MCT. The fits in figures 4.42 (a) - (c) provide a good description of the data at high temperatures (323 K and 363 K), and overall, the fits describe the data reasonably well from 1-2 decades below the minimum frequency ν_{min}. On the high frequency flank of the minimum the fits clearly deviate from the data as the influence of the boson peak comes into play more strongly. The steep increase towards the boson peak dominates the slope of the minimum, especially at lower temperatures, not allowing for reasonable fits.

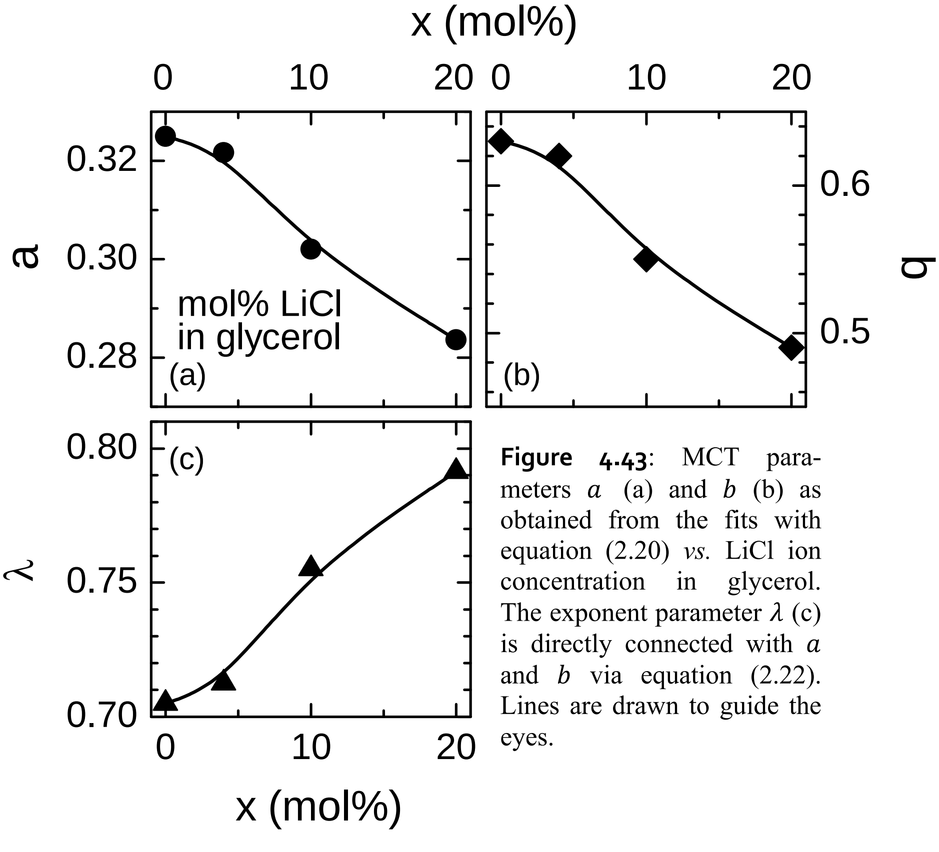

Figure 4.43: MCT parameters a (a) and b (b) as obtained from the fits with equation (2.20) *vs.* LiCl ion concentration in glycerol. The exponent parameter λ (c) is directly connected with a and b via equation (2.22). Lines are drawn to guide the eyes.

However, as seen in figure 4.42 (d) the quality of the fits for the glycerol sample doped with 20 mol% LiCl is worse then in the other three cases. Especially for 363 K and 323 K clear deviations from data and fits can be observed. It should be emphasized again, that the exponent parameters are interrelated via the system parameter λ, equation (2.22), and only depend on the material and not on temperature. This does not allow for a variation of the power law exponents a or b for one sample to obtain better fits at lower temperatures. In addition, deviations are expected in the vicinity of T_c, and the simple interpolation formula, equation (2.20), is only valid in a restricted region around the critical temperature. Thus, especially at low temperatures, deviations of data and fits towards the boson peak are not only observed but expected.

The fits with equation (2.20) lead to values of λ =0.705, 0.713, 0.755 and 0.791 with increasing ion content. The continuous increase of the system parameter with increasing LiCl content in glycerol is shown in figure 4.43 (c). The exponent parameters a and b, as directly connected with the system parameter λ via equation (2.22) are the exponents from the critical and von Schweidler law and shown in figures 4.43 (a) and (b) *vs.* LiCl ion concentration in glycerol. Remarkably, a clear decrease of a and b with increasing ion concentration is observed. This accounts for a broadening of the minimum with increasing ionic character of the sample. The lines are drawn to guide the eyes.

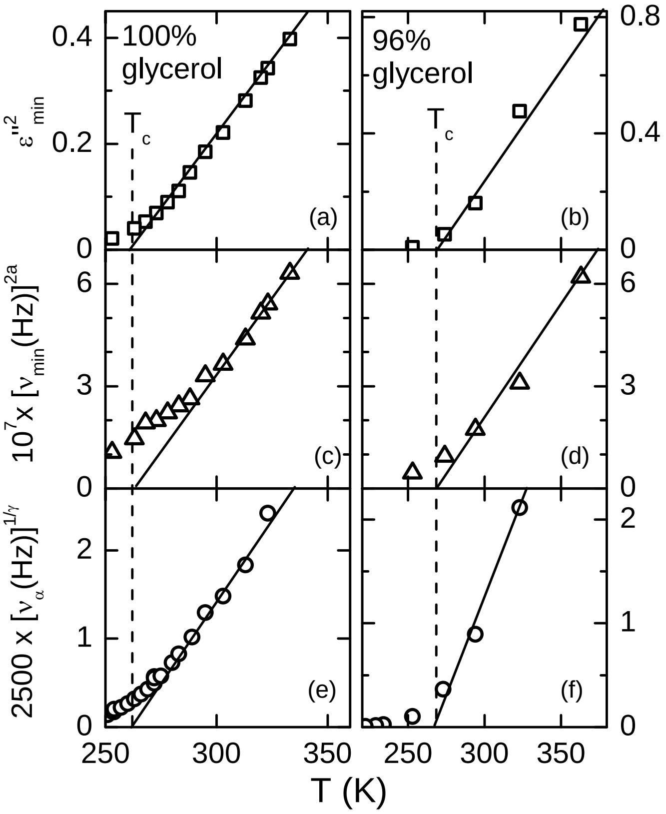

Figure 4.44: Temperature dependence of minimum amplitude ε_{min} (a) and (b), position ν_{min} (c) and (d) and α-relaxation rate ν_{α} (e) and (f) of pure glycerol[1] and glycerol with 4 mol% LiCl ions. Minimum amplitude and position were obtained by fits with equation (2.20). According to the predictions of MCT, representations have been chosen that should result in linear behaviour. The solid lines demonstrate a consistent description of all three quantities with a T_c of 262 K for pure glycerol and 268 K for the LiCl doped glycerol sample. Results of pure glycerol are published in Ref. 1.

According to the critical laws, equations (2.23), (2.25) and (2.26), the critical temperature T_c should manifest itself in the temperature dependence of minimum amplitude and position and in the temperature behaviour of the α-relaxation times. In figures 4.44 and 4.45 the temperature dependence of minimum amplitude ε_{min} (a) - (b), position ν_{min} (c) - (d) and α-relaxation rate ν_{α} (e) - (f) of pure glycerol and glycerol with 4, 10 and 20 mol% LiCl ions are shown as obtained by fits with equation (2.20). The representations have been chosen in such way that the critical laws of equations (2.25), (2.26) and (2.23) are linearised and therefore should lead to linear behaviour, extrapolating to T_c. The solid lines indeed indicate a consistent description of all three quantities with critical temperatures of 262, 268, 252 and 267 K, respectively.

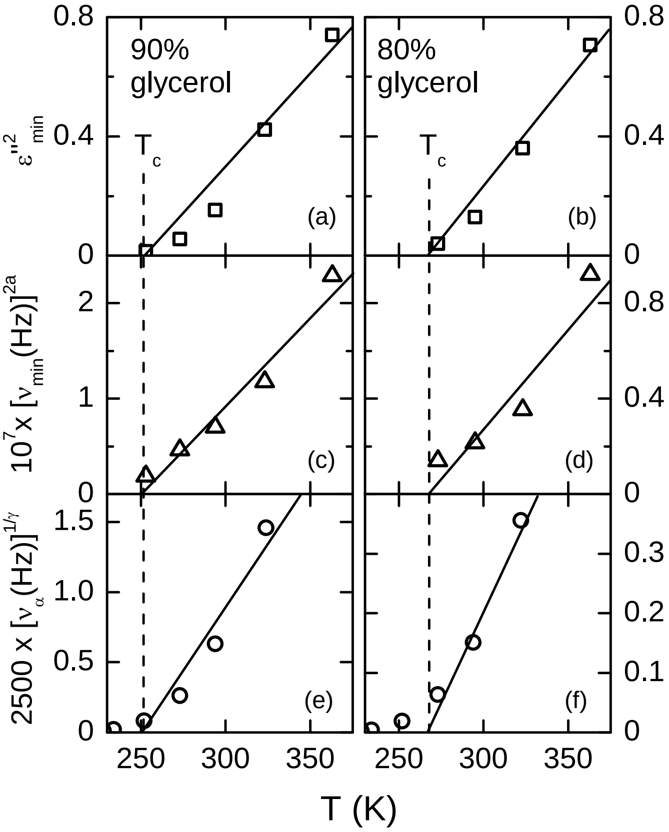

Figure 4.45: Temperature dependence of the minimum amplitude ε_{min} (a) and (b), position ν_{min} (c) and (d) and α-relaxation rate ν_{α} (e) and (f) of glycerol with 10 and 20 mol% LiCl ions. Minimum amplitude and position were obtained by fits with equation (2.20). According to the predictions of MCT, representations have been chosen that should result in linear behaviour. The solid lines demonstrate a consistent description of all three quantities with a T_c of 252 K and 267 K for the glycerol sample doped with 10 and 20 mol% LiCl ions.

The linearization of the relaxation times, $\nu_{\tau}^{1/\gamma}(T)$, is convincing for all shown concentrations, while in $\varepsilon_{min}^{2}(T)$ deviations are seen especially for the glycerol samples doped with 10 and 20 mol% LiCl and in $\nu_{min}^{2a}(T)$ for pure glycerol. The bad quality of the linearised critical laws in figure 4.45 (b) and (d) can be understood easily, because, the quality of the fits in figure 4.42 (d) is especially bad for the 323 K and 363 K curves. The relations (2.25), (2.26) and (2.23) should hold somewhat above T_c, but they are expected to fail too far a above T_c. For this reason, the proper choice of the temperature range in which the critical laws should hold, and that is used for the determination of T_c is difficult to determine. Overall, the significance of the representations of figures 4.44 and 4.45 should not be overemphasized. Results of pure glycerol are taken from Ref. 1.

- **Test for scaling behaviour**

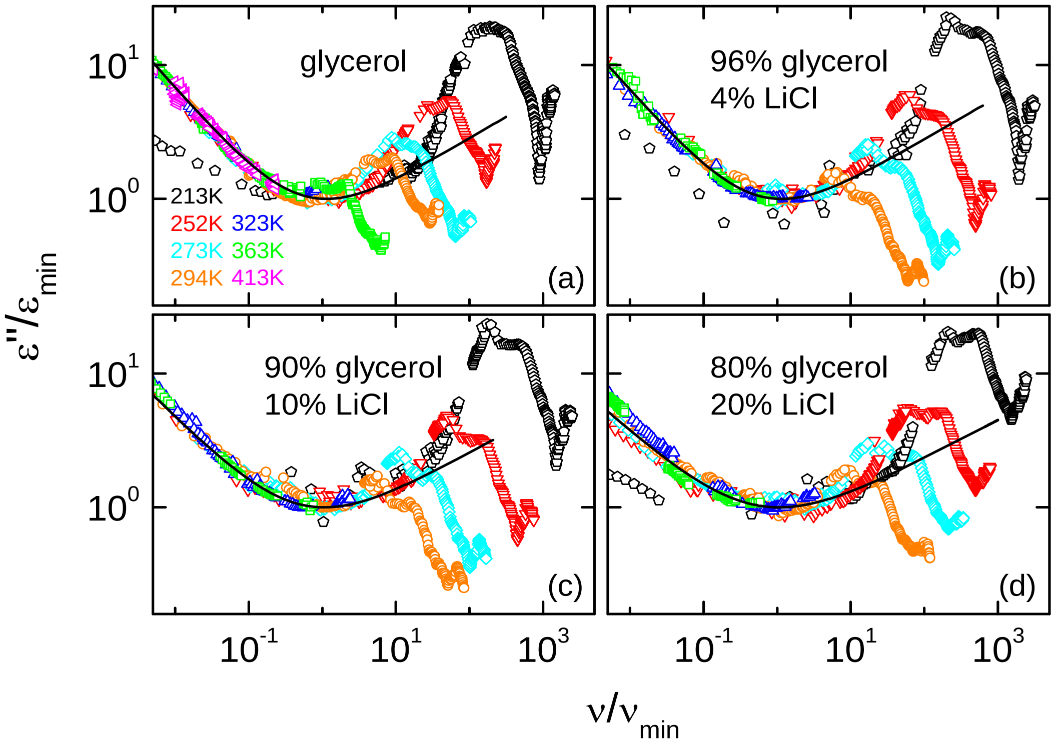

Figure 4.46: Master curves $\varepsilon''/\varepsilon_{min}$ vs. ν/ν_{min} from the dataset from figure 4.42. Except for the 213 K curves always ε_{min} and ν_{min} as obtained from mct fits from equation (2.20) were used for scaling.

In analogy to chapter 4.2.4 the scaling behaviour in the minimum region is tested. As mentioned in the previous paragraph, the decrease of a and b, denotes a broadening of the minimum with increasing ion content of the sample. This behaviour is now studied in more detail. The dielectric loss, $\varepsilon''(\nu)$, is scaled on its minimum position and frequency, $\varepsilon''/\varepsilon_{min}$ vs. ν/ν_{min}, so that the minima coincide. If possible, the parameters as obtained by fits with equation (2.20) were used. For temperatures, too low as to allow for reasonable fits, minimum amplitude and position were estimated by eye. Figure 4.46 (a) - (d) show the master curves as determined from the datasets of figures 4.42 (a) - (d) for pure glycerol, and the glycerol samples doped with 4, 10 and 20 mol% LiCl, respectively. The same symbols and colours in figure 4.46 always correspond to same temperatures, as indicated in frame (a). Apparently, for $T > T_c$, all curves corresponding to one concentration fall on the master curve. The scaling works particularly well on the low frequency side of the minimum. This gives evidence for the von Schweidler law, as the spectra for each temperature depict the same, temperature independent slope for all curves of one concentration, as postulated by MCT. However, scaling should fail at temperatures below the critical temperature. This is seen for the 213 K spectra, shown for each sample in figures 4.46 (a) - (d), as they strongly deviate from the theoretical curve at low and at high frequencies.

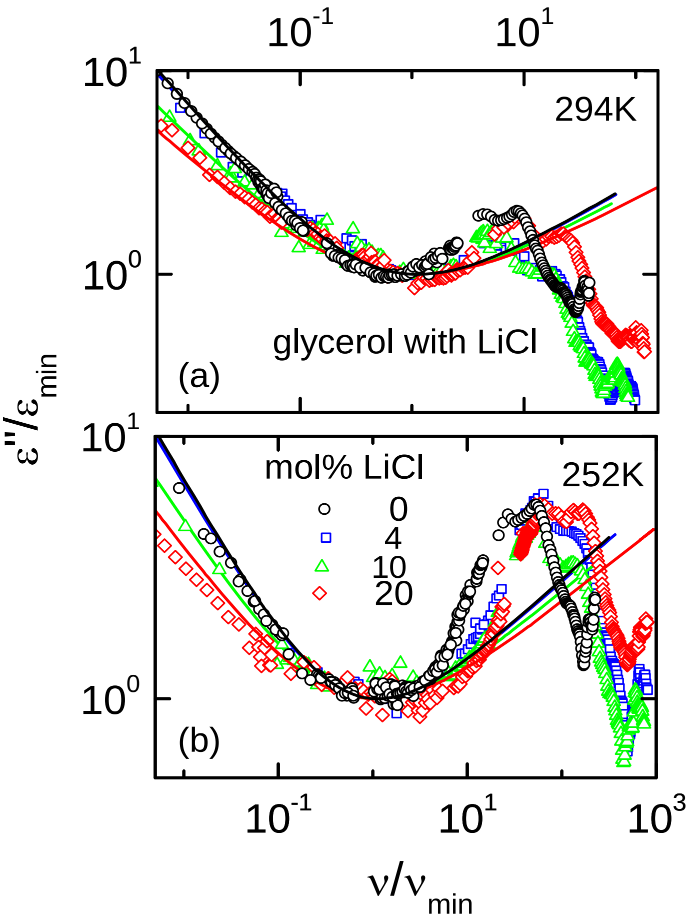

Figure 4.47: Master curves $\varepsilon''/\varepsilon_{min}$ vs. ν/ν_{min} of the datasets from figure 4.42. In (a) curves for the different concentrations at 294 K, in (b) for 252 K are scaled.

The situation at the high frequency flank is not easy to assess, because the dielectric loss is strongly influenced by the onset of the boson peak. The rather steep increase to the BP dominates the high-frequency region of the minimum. Overall, the scaling works very well as shown by the coincidence of the spectra that manifests itself at the low frequency side of the minimum.

After checking successfully for the scaling properties of the high-frequency minimum above T_c, the spectra of the different concentrations are compared amongst each other. Figures 4.47 (a) and (b) show the scaled dielectric loss spectra in the minimum region for 294 K and 252 K. Each kind of symbol corresponds to one distinct LiCl concentration in glycerol, as indicated in frame (b). Solid lines are the corresponding master curves as calculated from the exponent parameters a and b. Figures 4.47 (a) and (b) reveal the successive broadening of the minimum with increasing ion content in the glycerol sample. While the low frequency flank of pure glycerol and the sample doped with 4 mol% LiCl nearly overlap, the decreasing slope of the von Schweidler law becomes apparent in the glycerol samples doped with 10 and 20 mol% LiCl. However, also on the high-frequency flank of the minimum, the decrease of the slope of the critical law with increasing ion content of the sample gets evident. Here, the clearness of this behaviour is rather unexpected, as the influence of the boson peak comes strongly into play. The broadening of the minimum is, via the critical law $\nu_\tau \propto (T - T_c)^\gamma$, directly connected with a strong shift of the α-relaxation to lower frequencies. This shift indeed is observed in the measured spectra, cf. figure 4.35.

4.3.3.2 *Influence on the boson peak*

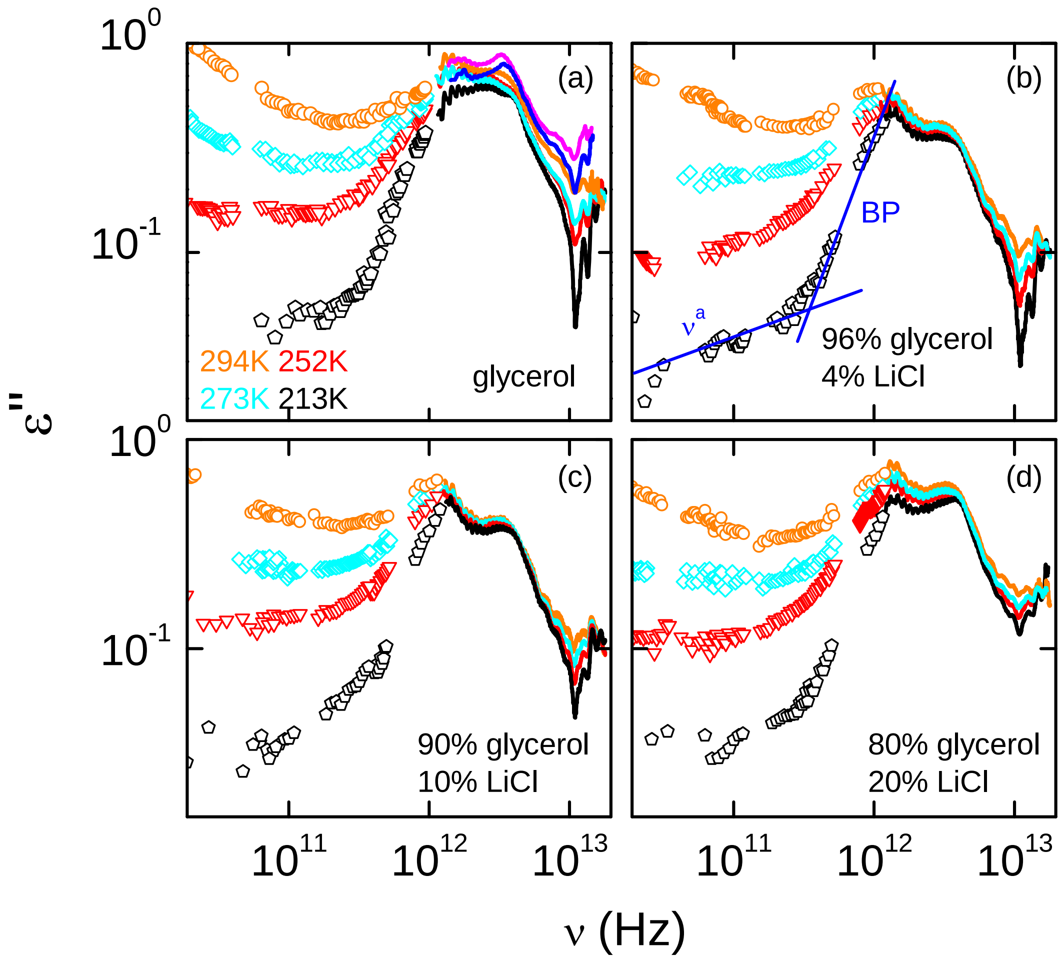

Figure 4.48: Dielectric loss spectra in the THz and IR region of the structural glass former glycerol (a) and binary mixtures of glycerol with 4 mol% (b), 10 mol% (c) and 20 mol% (d) LiCl at various temperatures. Same symbols and colours in each frame ascribe for the same temperatures, as indicated in (a). The solid lines in (b) visualises the influence of the boson peak to the minimum.

Figures 4.48 (a) - (d) display the frequency dependent dielectric loss spectra of pure glycerol and mixtures of glycerol with 4, 10 and 20 mol% LiCl, including measurements in the infrared region. The legend for all frames of figures 4.48 is indicated in (a). At frequencies beyond the minimum, a steep increase to the boson (microscopic) peak is revealed. At low temperatures, especially at 213 K, the strong influence of the boson peak on the high-frequency flank of the minimum clearly becomes apparent. The different contributions of the minimum and the boson peak are exemplarily indicated for the 213 K spectrum in figure 4.48 (b) by the solid lines. In general, the shape of the BP is rather broad, and exhibits some kind of double peak structure for all spectra shown in figure 4.48. At about $\nu \cong 10^{13}$ Hz, much sharper peaks show up. These resonance-like modes account for intramolecular excitations[224,225] and are decoupled from glass formation.

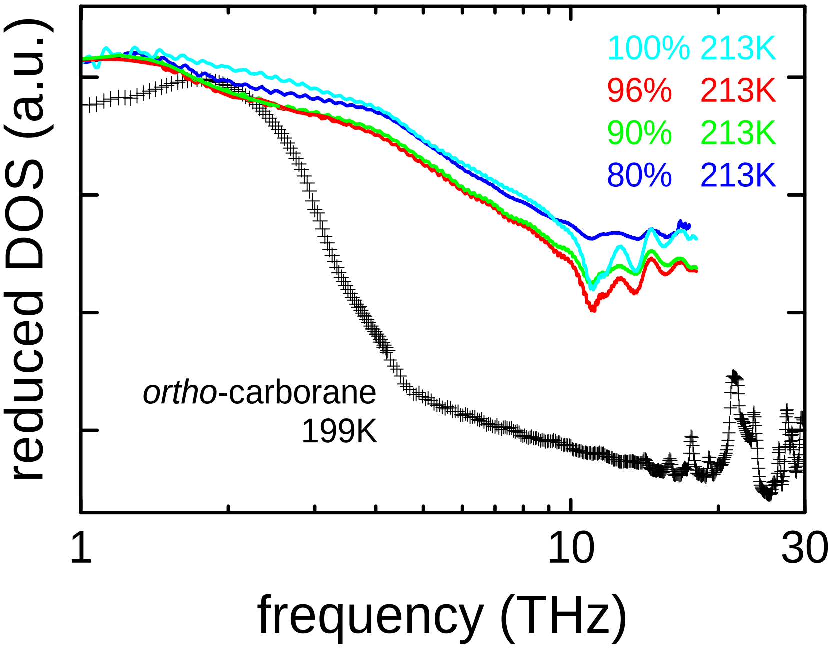

Figure 4.49: Dielectric loss in the IR region of the structural glass former glycerol, three different glycerol-LiCl mixtures and plastic crystalline OCA.[60] The plotted quantity, $\varepsilon'' T/\omega$, is approximately proportional to $g(\omega)/\omega^2$, corresponding to the reduced DOS divided by the squared frequency.

In analogy to the discussion of chapter 4.2.5, figure 4.49 demonstrates for 213 K, the lowest temperature measured in all mixtures that the detected peaks indeed correspond to a peak in the quantity $\varepsilon'' T/\omega$, which is a good approximation of $g(\omega)/\omega^2$. In addition, the THz loss-peak of plastic crystalline ortho-carborane (OCA) is shown for 199 K. While the low-frequency wing of the boson peak looks quite similar for all materials, the high frequency wing for the plastic crystal exhibits a much steeper decrease than in glycerol and its binary mixtures. As mentioned before in chapter 4.2.5, OCA is a prototypical plastic crystal, composed of nearly spherically shaped $B_{10}C_2H_{12}$ molecules, forming a rigid icosahedron. In contrast to canonical glass formers, there are well-defined phonon modes in plastic crystals. However, $B_{10}C_2H_{12}$ molecules can be seen as hard spheres with strong intramolecular bonding, linked to each other by weak van der Waals bonds. For this reason, it seems straightforward, to expect a purely acoustic Debye phonon DOS for OCA, while in glycerol and its mixtures, also optical modes should play a role.[60,62] The observed double peak structure may result from the complete vibrational DOS. One may speculate that the low frequency part of the BP is determined by the acoustic DOS, similar to the plastic crystal, while the high frequency part corresponds to acoustic phonon modes.[60,62]

4.3.4 Neutron scattering vs. dielectric spectroscopy

Figure 4.50 displays the frequency dependence of the imaginary part of the susceptibility $\chi''(\nu)$ of glycerol,[1] as obtained by dielectric spectroscopy, neutron- and light-scattering experiments. The symbols, except the open diamonds, represent dielectric results, those from light scattering are shown as solid lines, while neutron scattering results are displayed as open diamonds. Data shown in black is taken from Ref. 35. In general, scattering results give no information about the absolute values of χ'', and therefore have been vertically scaled to obtain a comparable height of the α-peak. In addition recent neutron scattering data, obtained from experiments at the TOFTOF spectrometer in Garching, are shown as dashed lines. They match reasonably well with the previous measurements. In addition, the new data extend the frequency range to higher frequencies, and resolves the boson peak.

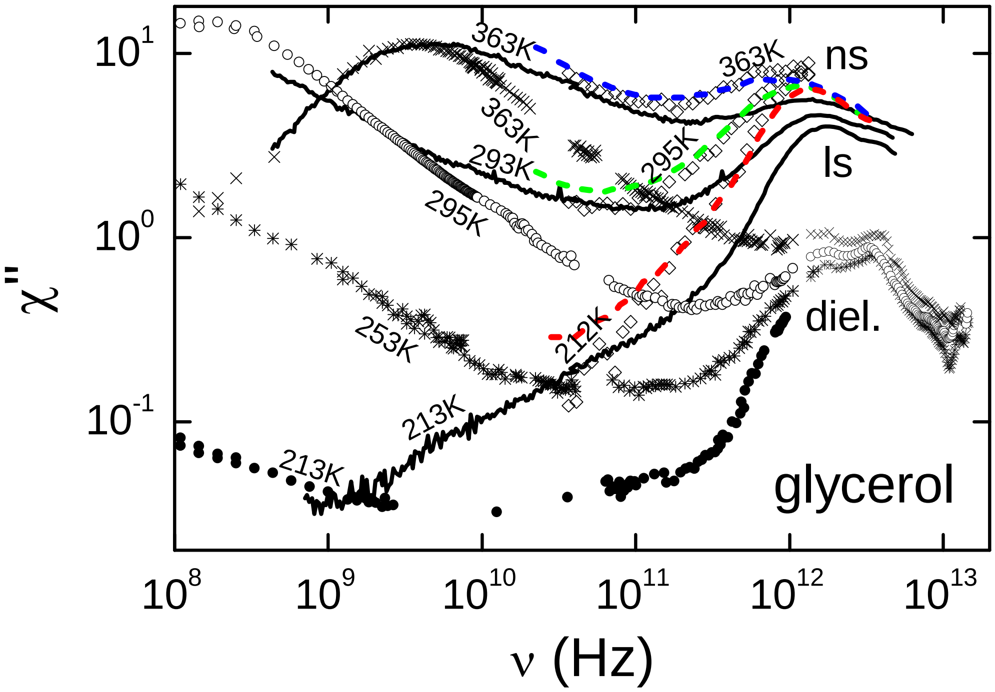

Figure 4.50: Frequency dependence of the imaginary part of the susceptibility of glycerol. The symbols (except for the diamonds) represent dielectric results, those from light scattering[61] are shown as solid lines. Diamonds show neutron scattering results from Ref. 61. The light and neutron scattering data sets have been vertically shifted to give a comparable intensity of the α-peak. Dashed lines show results from recent ns scattering experiments at the TOFTOF spectrometer in Garching. All datasets shown in black are taken from Ref. 35.

Figure 4.50 clearly shows that the increase to the microscopic peak is situated at the same frequency in dielectric, neutron- and light-scattering experiments. However, the amplitude of the boson peak, compared to the height of the α-peak is smaller in dielectric experiments.

Figure 4.51 shows the same data as displayed before in figure 4.48, but additionally the results from neutron scattering measurements are included. They are displayed as dashed lines. Temperatures according to the particular spectra are indicated in frame (a). Due to experimental details, by dielectric spectroscopy no measurements at temperatures above room temperature could be performed in the infrared region. The neutron scattering results have approximately been scaled on the boson peak height as obtained by dielectric measurements.

The increase from the minimum towards the boson peak is almost identical in both methods. This is best seen from the 252 K and the 213 K spectra. However, taking into account the height of the α-relaxation, the amplitude of the microscopic peak is much smaller in dielectric than in scattering experiments.

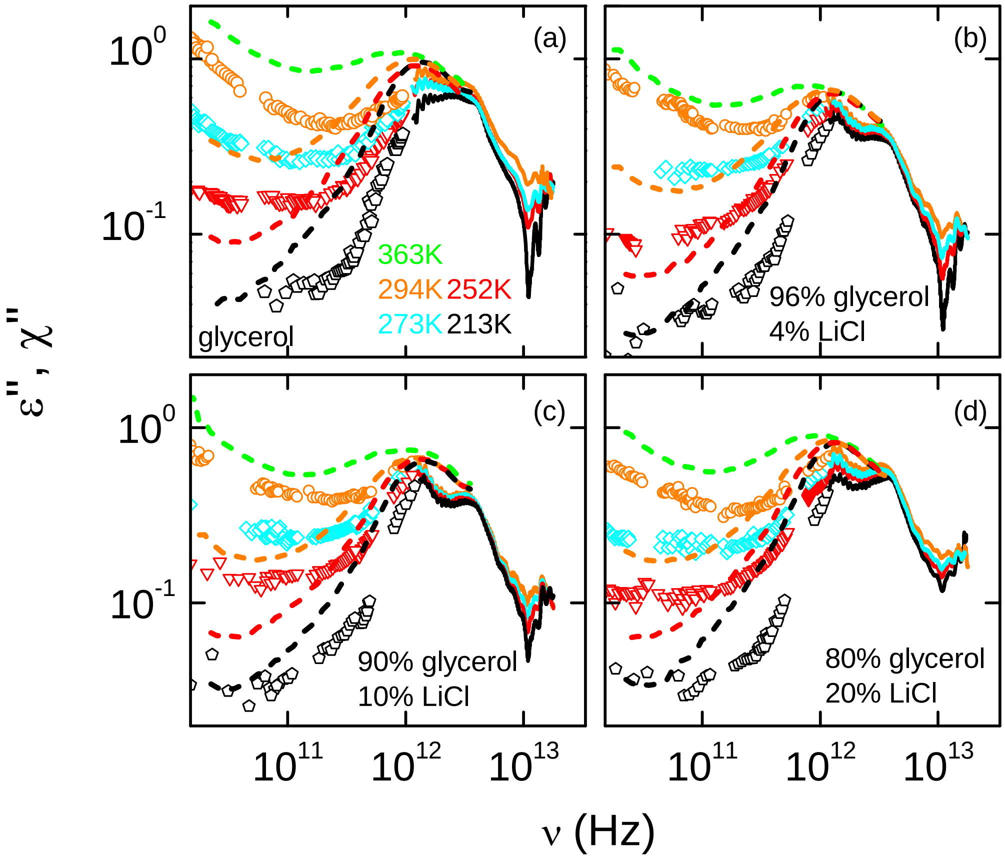

Figure 4.51: Frequency dependence of the imaginary part of the susceptibility of glycerol (a) and three different binary glycerol-LiCl mixtures. The symbols represent the dielectric results, those from neutron scattering are shown as dashed lines. The neutron scattering data sets have been vertically shifted to give a comparable intensity of the boson peak.

In addition, the double peak structure, discussed in the previous section (cf. 4.3.3.2) is not observed in the neutron scattering spectra, possibly due to a better energy resolution in the dielectric measurements. Trying to fit the neutron scattering spectra with the same exponent parameters a and b as obtained in the idealized mode coupling analysis of the dielectric data, was not successful. The neutron scattering data mainly is restricted to a frequency range above the minimum frequency, therefore it was not possible to perform reasonable fits at least at temperatures $T \leq 294$ K. At 363 K, the highest temperature investigated, the high frequency minimum is well pronounced, but the increase to the α-peak is too steep to allow for reasonable fits, at least with the parameters obtained in section 4.3.3.1. For an analysis in the framework of MCT, additional measurements to lower frequencies, using further scattering techniques, are necessary.

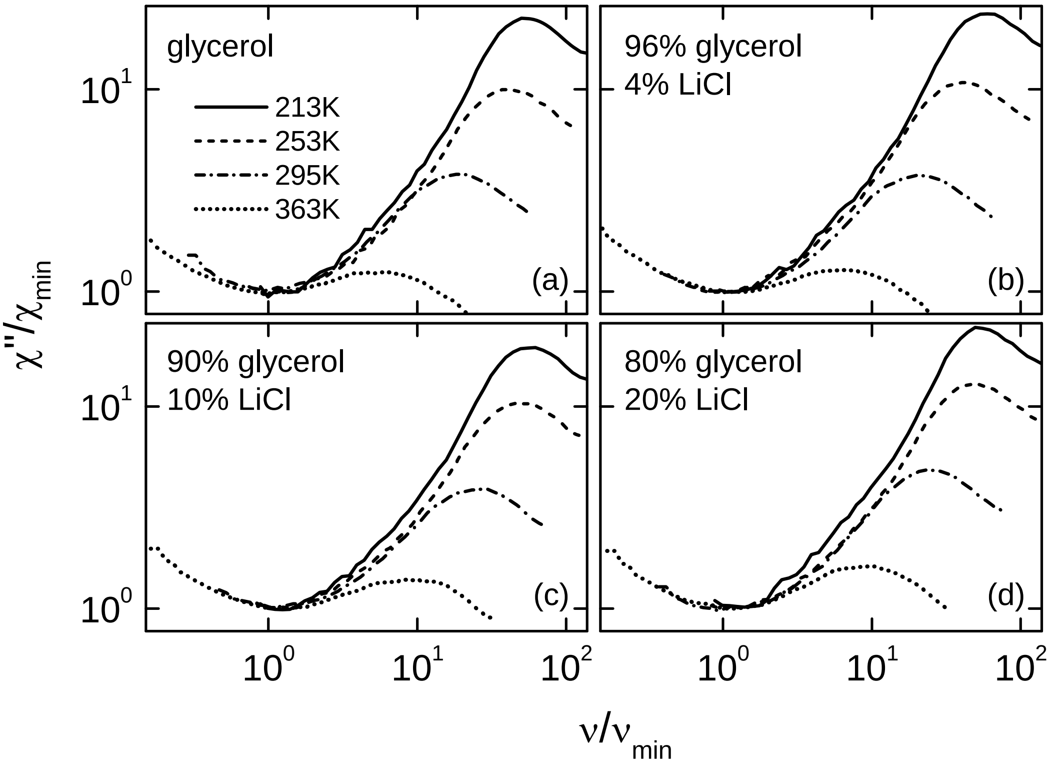

Figure 4.52: Susceptibility χ''/χ_{min} vs. ν/ν_{min} for glycerol and three different binary glycerol-LiCl mixtures as shown in figure 4.51 on a log-log plot. Different curves in one frame correspond to the temperatures as indicated in frame (a).

Figure 4.52 provides the neutron scattering spectra of glycerol and the three binary glycerol-LiCl mixtures, scaled on the minimum. Figures 4.52 (a) - (d) show, that due to the restricted frequency range, no statements on the scaling behaviour of the low frequency flank can be made. It was not possible to perform an analysis in the framework of idealized MCT for the neutron scattering data, and therefore no master function can be shown in figure 4.52. Minimum amplitude and position, as used for the scaling procedure were determined just by eye. Anyhow, looking at the high-frequency flank of the minimum, the spectra seem to scale quite well up to frequencies were the boson peak sets in. The rather steep increase to the BP dominates the high-frequency region of the minimum and the critical law is not developed very well. However, the influence of the boson peak seems weaker than in the dielectric measurements, displayed in figure 4.46.

The main result of the figure 4.46 is a clear broadening of the minimum with decreasing temperature and an increasing influence of the boson peak. In figure 4.52, the situation is clearly different. The spectra do not show any broadening. On the contrary, the minimum makes a smooth transition to the boson peak and the high-frequency flank seems to scale in a broader range than for the dielectric data.

In figure 4.53, the $\chi''(\nu)$ spectra for the same concentrations as in figure 4.52 are scaled on the minimum for 295 K (a) and 252 K (b). All spectra show the same increase towards the boson peak and it gets clear, that the neutron scattering data does not show any broadening of the minimum of the fast β-process. In the framework of MCT, this implies, that the α-peak position should be less influenced than in dielectric measurements. However, due to the restricted frequency range of the neutron scattering data, this cannot be checked for.

An explanation for the different behaviour in the minimum region can presumably be found in the different coupling to the tensorial properties of both methods.[187] Dielectric spectroscopy mirrors the reorientational motions of the glycerol molecules and the translational motions of the ions, coupling to each other. Neutron scattering only considers density fluctuations, meaning translational degrees of freedom of the particles in the sample. The simplest schematic model of MCT deals with a single correlator $\phi(t)$ only. However, the MCT model for the reorientational dynamics of a non-spherical probe molecule suggests to introduce a second correlator. This model[218] was motivated by Sjögren[139] and in collaboration with M. Sperl and J. Wuttke a comparative study is on the way which should be able to explain broadening of the minimum in the dielectric data and also the differences to the neutron scattering data.

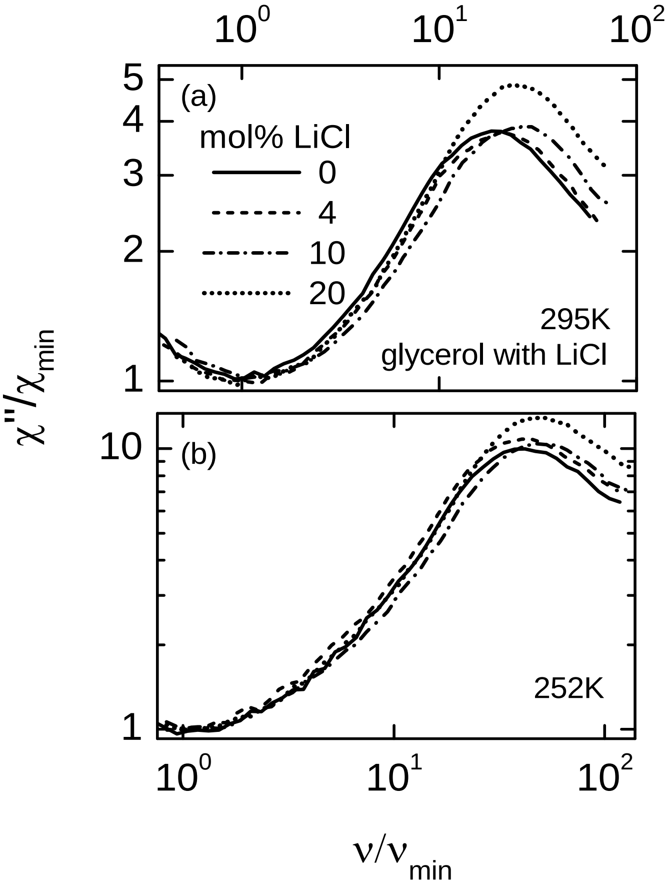

Figure 4.53: Master curves χ''/χ_{min} vs. ν/ν_{min} from the datasets of figure 4.52. In (a) curves for the different concentrations at 295 K are scaled, in (b) for 252 K.

4.4 Relationship between fragility and the boson peak

For the understanding of the complex behaviour of vitrification, fragility is believed to play a central role.[248] The microscopic interpretation of the fragility suggests that it controls a number of properties like structural state dependence, decoupling phenomena and non-exponentiality of the α-relaxation.[275] In literature, a vast collection of publications is found, trying to discover correlations of fragility to other important quantities.[6,276–278]

A quantity that directly measures the fragility is the fragility index m:[84]

$$m = \left.\frac{\mathrm{d}\log\langle\tau\rangle}{\mathrm{d}\left(\mathrm{T_g}/\mathrm{T}\right)}\right|_{T=T_g} \tag{4.6}$$

This corresponds to the slope at T_g in the Angell plot,[79,80] schematically shown as inset in figure 2.6. Glass formers are termed as "strong" if their relaxation-time curves do not or only weakly deviate from linear (thermally activated) behaviour in the Angell plot. Those that exhibit strong deviations from linear behaviour and that show a strong curvature in their relaxation time curve are termed as "fragile".

Figure 4.54 shows the T_g-scaled Arrhenius plot of the α-relaxation times of various structural glass formers.[17] The dashed lines show the behaviour for minimal (m = 16) and very high (m = 200) fragilities. The relaxation times of the series of propylene glycols as displayed in figure 4.54, gives evidence for intermediate fragility, increasing with molecular size from m = 48 to 74. Similar values were reported by León *et al.* (m = 53, 64 and 71 for PG, DPG and TPG respectively).[207] In Ref. 248, an intermediate fragility parameter of m = 53 was reported for glycerol. The fragilities of the binary glycerol - LiCl mixtures, were determined to m = 50, 57 and 62 (for 4, 10 and 20 mol% LiCl in glycerol, respectively).

The fragility shows a tendency to increase with increasing ion content. In the framework of the potential energy landscape, the fragility it is connected with the number of minima and by the mean and variance of the barriers separating the minima.[275] The ions in the binary glycerol - LiCl mixtures may induce breaking of the hydrogen bonds, leading to a higher degree of disorder in the sample. Therefore a higher density of minima in the potential energy landscape may be assumed. For the series of propylene glycols the situation is quite similar. The more complex di- and tripropylene glycol molecules induce a higher degree of disorder, directly connected with the higher density of minima in the potential energy landscape.

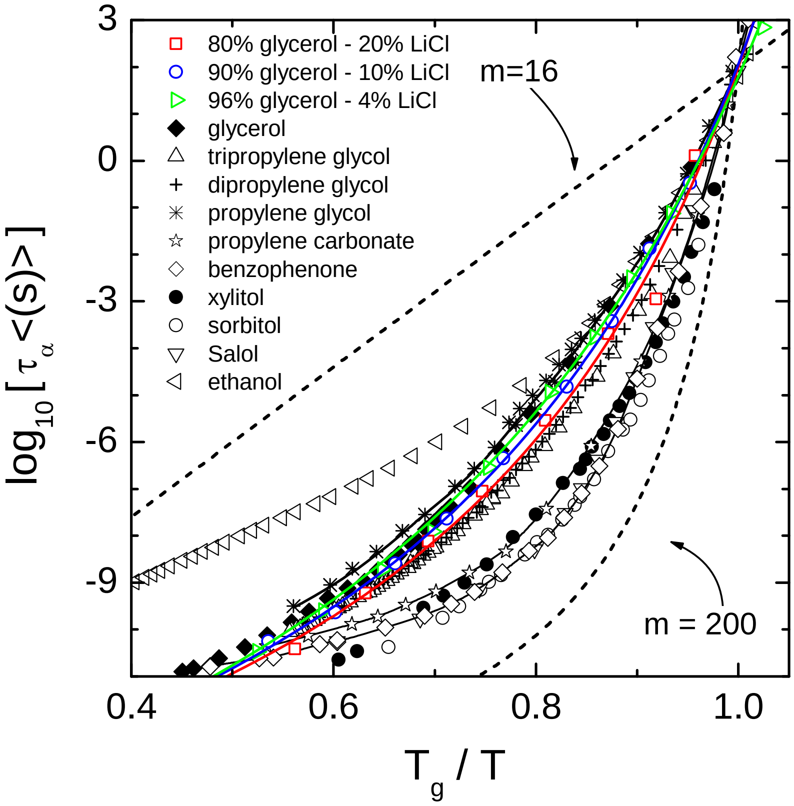

Figure 4.54: Angell plot of the α-relaxation times of several structural glass-formers.[17] The dashed lines indicate the behaviour for minimal and maximum fragility. The glass transition temperatures used to scale the data are: 99 K (ethanol), 186 K (glycerol), 167 K (propylene glycol), 194 K (dipropylene glycol), 189 K (tripropylene glycol), 248 K (xylitol), 156 K (propylene carbonate), 207 K (benzophenone), 218 K (Salol), 268 K (sorbitol), 204 K (80% glycerol - 20% LiCl), 194 K (90% glycerol - 10% LiCl) and 191 K (96% glycerol - 4% LiCl).

A disorder induced increase of the fragility was recently found in the plastic crystal Freon 112,[121] which is assumed to be a mixture of two different conformations, *trans* and *gauche*. In addition, the binary plastic crystalline system of 60% succinonitrile and 40% glutaronitrile (60SN - 40GN)[279,280] shows an unusual high fragility. The mixture of two different molecules and three different molecular conformations (*trans*, *gauche*, and *cis*) of glutaronitrile give rise to a strong substitutional disorder in this mixture, which leads to higher fragility.

Böhmer *et al.*[248] performed an extensive study of a variety of glass formers, and reported about the systematic behaviour of the fragility in different glass-forming systems. They showed that, in contrast to covalent glass formers, polymers appear at the fragile extreme in the classification scheme. Taking into account their study, the fragility of PG, DPG and TPG is expected to increase as the molecules tend to get more "polymer-like".

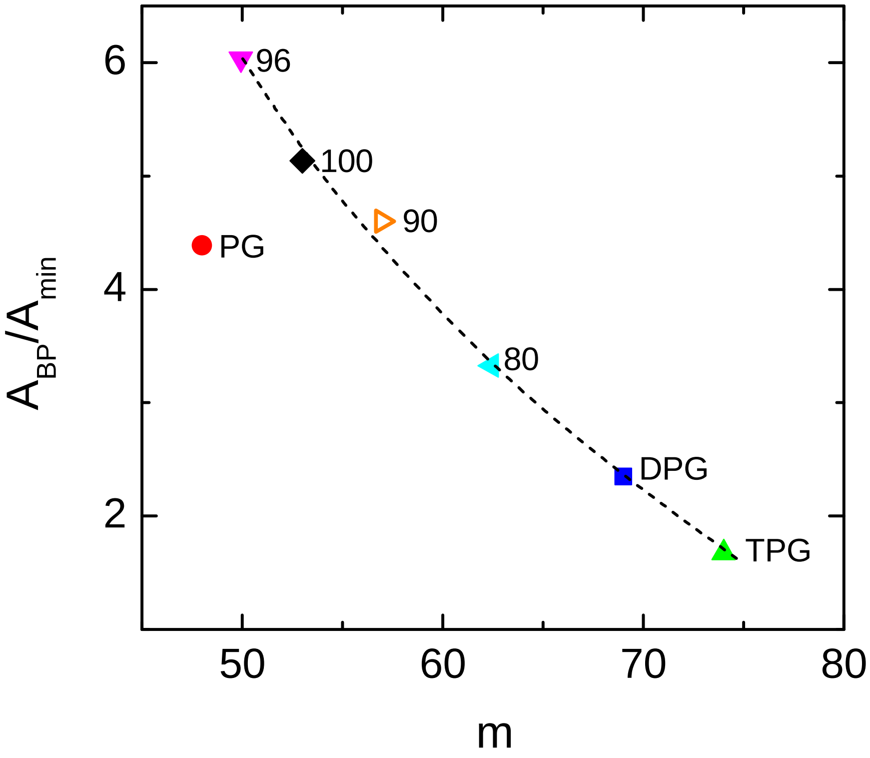

Figure 4.55: Ratios of boson peak and minimum amplitude *vs.* fragility. Numbers at the symbols refer to the glycerol content in the glycerol – LiCl mixtures. As no measurements at T_g were performed, temperatures as close as possible to an approximate ratio of $T/T_g \approx 1.3$ are chosen: 1.34 (80% glycerol – 20% LiCl), 1.30 (90% glycerol – 10% LiCl), 1.32 (96% glycerol – 4% LiCl), 1.35 (glycerol), 1.37 (TPG), 1.34 (DPG), 1.39 (PG). The dashed line is to guide the eyes.

In Ref. 281, Sokolov *et al.* present a systematic investigation of the differences in the dynamics of strong and fragile glass formers. They analysed Raman spectra, neutron data and low temperature heat capacity data of different glass-forming systems with significantly different degrees of fragility, and related the ratio of relaxational and vibrational contributions at T_g to the fragility index. Here, *relaxational* denotes the fast β- and *vibrational* the boson peak contribution. This ratio is found to be higher the stronger the glass-former is. In literature, no comparable analysis of dielectric measurements is found. The ratio of boson peak amplitude to dielectric loss of the minimum position versus the fragility is shown in figure 4.55. The infrared measurements only were performed at $T > T_g$. For this reason an approximate ratio of $T/T_g \approx 1.3$ is chosen for the representation. Except for PG, a strong correlation between both magnitudes is observed as all values fall on one line. However, one should be aware, that the boson peak amplitude in light scattering and dielectric experiments slightly differ, as explained in section 2.2.4. For this reason the results from the dielectric study cannot directly be compared to the results of Sokolov *et al.*[281] Nevertheless, the correlation found here, connects the fast processes with the glass transition.

In addition, a general increase of the system parameter λ, as determined in the analysis of the framework of idealized MCT, with the fragility shows up in figure 4.56. The original MCT only reveals three time scales of dynamic processes: the α-relaxation, the fast β-relaxation and the microscopic process. At high temperatures, the slow β-relaxation or excess wing usually are merged with the α-peak and no longer plays a role in the spectra. At high temperatures, the high-frequency flank of the α-relaxation peak therefore directly crosses over into the low frequency flank of the minimum, the so-called von Schweidler law ν^{-b}. The relation $\beta_{CD} = b$ should hold and, the increase of λ mirrors the α-relaxation dynamics: With increasing λ, b decresaes, meaning a broadening of the α-peak, which usually is connected with the distribution of the relaxation times. A connection between the fragility and β_{KWW} at T_g, with $\beta_{KWW} = \beta_{CD}^{1/1.23}$,[274] is given by the so-called "Böhmer relation". Böhmer *et al.*[248] found a correlation between the fragility and the nonexponentiality $m(\beta_{KWW}(T_g))$ at least for intermediate fragilities. Because of the relation between λ, β_{KWW}, β_{CD} and m, the representation of figure 4.56 seems to be equally suited to check for correlations as the Böhmer relation.

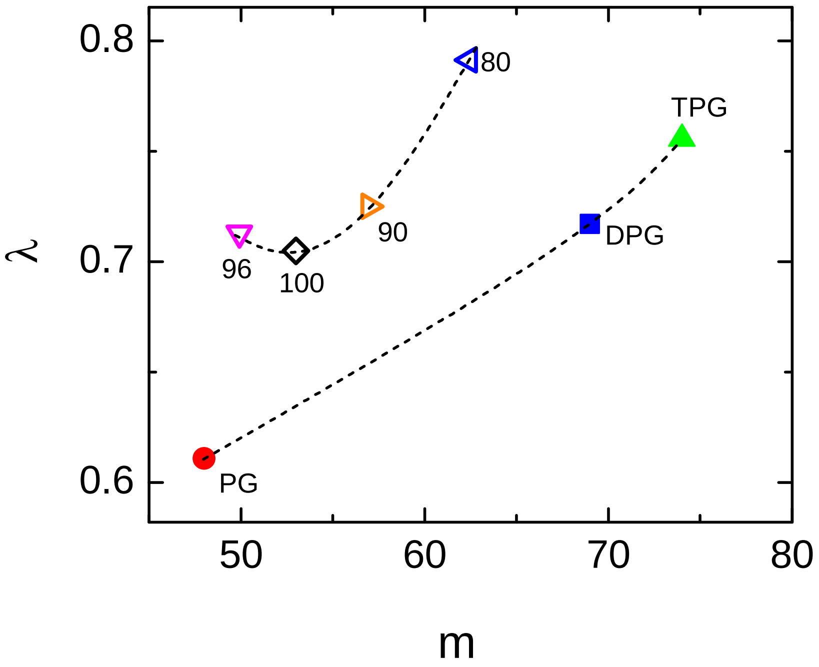

Figure 4.56: System parameter λ as determined from the analysis in the framework of idealized MCT vs. the fragility m. A general trend of an increase of λ with increasing fragility is observed. Numbers at the symbols refer to the glycerol content in the glycerol – LiCl mixtures.

5 Summary and conclusion

The dielectric loss of glass-forming liquids is governed by a whole zoo of dynamic phenomena: the structural α-relaxation, the excess wing and the slow β-relaxation, the minimum regime and the boson peak. The present work provides information on all these processes in a series of different molecular glass-formers. These allow for testing several phenomenological models and theories on the dynamics of supercooled liquids. By the variation of key parameters, for the first time systematic studies on the behaviour of the fast β-process and the boson peak were performed. In contrast to previous measurements, the frequency range was significantly extended.

- The α-process

The structural α-relaxation peak is the dominating feature in the dielectric loss spectra and has the property that its time scale tremendously changes over many decades with temperature. Although it is well established, that this primary relaxation process is directly connected with the viscosity of the glass, many open questions remain, just to mention the concept of fragility and its importance to gain a deeper understanding of the glass transition.

An increase of the fragility is observed in the series of propylene glycols with increasing molecular size and in the binary system glycerol-LiCl with increasing ion content. This can be explained in the picture of the potential energy landscape. Here, the fragility is determined by the number of minima and the barriers between them. A higher density of minima in the potential energy landscape is connected with a higher degree of disorder in the sample and with an elevated fragility. One may speculate, that the more complex di- and tripropylene glycol or the increasing ion content in the binary glycerol-LiCl induce a higher degree of disorder and thus give an explanation for the observed behaviour of the fragility.

Contrary to expectations, the relaxation of tripropylene glycol seems to be faster than for the smaller dimer. This may be explained by weakening of the intermolecular hydrogen bonds due to the extended molecular size of the trimer. However, this puzzling behaviour vanishes when scaling the relaxation times in the Angell-plot.

- Excess wing and slow β-process

At frequencies beyond the α-relaxation often an excess wing or an additional secondary peak, the (slow) β-relaxation process emerges.[23,24,28,42,43]
In the series of propylene glycols, the monomer is a typical Type A glass former, exhibiting an excess wing, while the di- and trimer are classified as Type B glass formers, showing pronounced secondary peaks. Aging experiments[25,44] revealed, that both processes are due to the same microscopic origin. The excess wing just is the high-frequency flank of the β-

process, mainly covered by the dominating α-relaxation. In contrast to the di- and trimer, the β-relaxation in the monomer was classified as genuine Johari-Goldstein relaxation. The β-relaxation times in the di- and tripropylene glycol exhibit a pronounced minimum in their relaxation times $\tau(T^{-1})$ around T_g. The minimal model[82] and a more recent approach considering the hybridization of a slower unresolved JG- with the β-relaxation[180] try to explain the microscopic origin of this minimum.

Recently, pressure experiments[201,204] revealed the existence of a further secondary process, in DPG and TPG, situated in the frequency range between α- and β-peak. In contrast to the peaks at ambient pressure, these were classified as Johari-Goldstein relaxations.

Doping glycerol with LiCl ions has a clear effect on the excess wing: Its strength increases with increasing ion content. Recently, Pronin *et al.*[273] argued, that the evolution from an excess wing into a significant secondary relaxation peak, observed in ultrahigh pressure experiments in glycerol, could be caused by the breaking of the hydrogen bonds. The addition of ions is supposed to have the same effect on the hydrogen bonds, enabling the glycerol molecules to perform small angle reorientations more easily. This leads to a more pronounced excess wing.

- Fast β-process

Today the presence of the minimum and the existence of excess intensity are well established.[1,3,51–53,113] As the access to the high frequency range by dielectric spectroscopy is an experimentally challenging task, only few molecular glass-formers have been investigated in this region. The present work provides a consistent description of the fast β-process in the framework of idealized MCT on several glass forming liquids: Salol, xylitol, the series of propylene glycols and the binary system glycerol-LiCl.

The mode-coupling analysis in the series of propylene glycols[179] reveals that the relative minimum amplitude, and therefore the strength of the fast β-process increases with increasing molecular size. This may be attributed to a better coupling of the dielectric loss to translational modes for the larger molecules. One can speculate, that for the spatially more extended di- and trimer steric hindrance arises and that reorientational and translational motions are stronger coupled. It is well known, that in dielectric spectroscopy the relative amplitude is weaker than of the susceptibilities determined by neutron and light scattering methods. These couple more directly to density fluctuations.[3,51,53,54]

A MCT analysis of binary glycerol - LiCl mixtures reveals that the power law exponents a and b decrease with increasing ion concentration, visualized by a successive broadening of the minimum with increasing ion content. On the α-relaxation timescale, idealized MCT predicts a critical behaviour via $\nu_\tau \propto (T - T_c)^\gamma$, with $\gamma = 1/2a + 1/2b$. For decreasing power law exponents, this implies a shift of the α-peak position to lower frequencies, which indeed is observed in the present system.

The broadening of the minimum with increasing ion content clearly becomes apparent when scaling the dielectric loss data on minimum amplitude and position. Scaling of the neutron scattering data does not reveal any broadening. This implies different coupling to the tensorial properties of both methods and maybe explained in the framework of an extended version of MCT.

- Boson peak

In addition, infrared measurements have been performed for the series of propylene glycols and for the binary glycerol-LiCl mixtures. These provide information on the behaviour of the boson peak and reveal a double peak structure in the dielectric spectra. There is plenty of room for speculations, about this double peak structure,[60,62–69] and if it is inherent to the spectral shape of molecular glass-forming materials.

An interesting property of glass-forming liquids is reflected in the correlation of the fragility and the ratios of boson peak and minimum amplitude. This evidences that the α-relaxation process is not only responsible for the viscosity. There must be a connection between low and high-frequency phenomena, which seems to be crucial for the understanding of the physics of glasses and the glass transition.

6 Appendices

6.1 S-parameter

The complex *S*-parameters $S_{11}(\omega)$ and $S_{21}(\omega)$ measured by the network analyser HP 8510C allow for the calculation of reflection- and transmission coefficients Γ^* and T^*.[160] The reflection coefficient calculates as

$$\Gamma^* = K^* \pm \sqrt{(K^*)^2 - 1} \tag{6.1}$$

with

$$K^* = \frac{[S_{11}^2(\omega) - S_{21}^2(\omega)] + 1}{2S_{11}(\omega)} \tag{6.2}$$

while the transmission coefficient reads as:

$$T^* = \frac{[S_{11}(\omega) + S_{21}(\omega)] - \Gamma^*}{1 - [S_{11}(\omega) + S_{21}(\omega)]\Gamma^*} \tag{6.3}$$

Then the complex permittivity is

$$\varepsilon^* = \frac{\lambda_0}{\Lambda} \cdot \frac{1 - \Gamma^*}{1 + \Gamma^*} \tag{6.4}$$

with

$$\frac{1}{\Lambda^2} = -\left[\frac{1}{2\pi l} \ln\left(\frac{1}{T^*}\right)\right]^2 \tag{6.5}$$

where λ_0 is the free space wavelength and l is the length of the coaxial line. The numerical calculation of the here shown formulae is done with the help of a *MathCAD* program.

6.2 From the correlation function to the structure factor

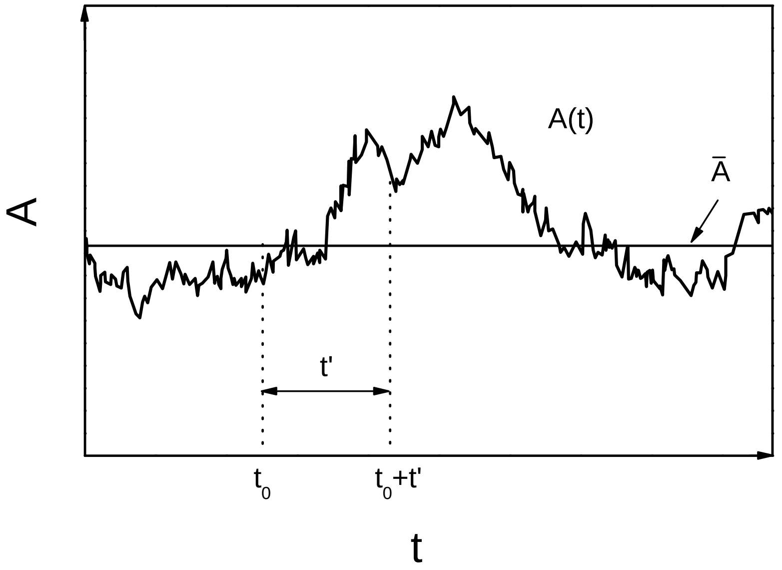

Figure 6.1: Time evolution of the instantaneous fluctuations of quantity A.[282]

Time correlation functions can be expressed as:

$$C(t) = \langle A(t)A(0)\rangle \tag{6.6}$$

Figure 6.1 shows the time evolution of the fluctuations of the quantity A, fluctuating around its average value in equilibrium. The correlation of A at one time t_0 with A at another time $t_0 + t'$ is measured by the correlation function $C(t')$. Now $A(t)$ is assumed to be the particle density. The particle-density operator gives the number density of particles at position $\vec{r}$ and time t:[168]

$$\rho(\vec{r}, t) = \sum_i \delta(\vec{r} - \vec{r_i}(t)) \tag{6.7}$$

A Fourier transform leads to:

$$\rho_{\vec{k}}(t) = \sum_i \int d\vec{r} e^{i\vec{k}\vec{r}} \delta\big(\vec{r} - \vec{r_i}(t)\big) = \sum_i e^{i\vec{k}\vec{r_i}(t)} \tag{6.8}$$

The correlation function in this case is labelled as $F(k,t)$[IV, 283] and can be expressed as follows:

$$F(k,t) = \frac{1}{N}\langle \rho_{-\vec{k}}(0)\rho_{\vec{k}}(t)\rangle = \frac{1}{N}\sum_{ij}\langle e^{-ik\cdot r_i(0)}e^{ik\cdot r_j(t)}\rangle \tag{6.9}$$

Basically $F(k, t = 0)$ is measured by scattering experiments:

$$F(k, t = 0) = \frac{1}{N}\langle \rho_{-\vec{k}}(0)\rho_{\vec{k}}(0)\rangle \equiv S(k) \tag{6.10}$$

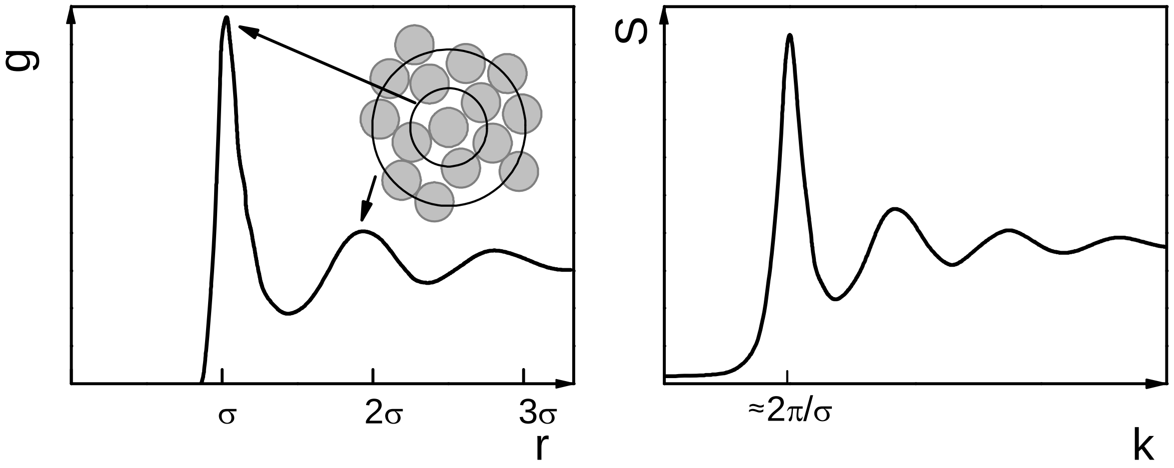

Figure 6.2: Typical shape of the radial distribution function $g(r)$ and the corresponding $S(k)$-curve in reciprocal space. In addition the salvation shells, belonging to the indicated maxima in $g(r)$ are shown.[282]

$S(k)$ is called the static structure factor of the liquid, as it is closely related to the radial distribution function $g(r)$. This function is proportional to the probability that a particle stays in the distance r from another particle at the origin. This relation is clearly shown in figure 6.2. There the correspondence of the peak maxima of $g(r)$ to the first and second salvation shells in the liquid[282] is shown, and the relation between distribution function and the static structure factor gets clear. The relation between both magnitudes can be expressed as:

$$S(k) = 1 + \rho \int d\vec{r} e^{-i\vec{k}\cdot\vec{r}} g(\vec{r}), \tag{6.11}$$

where ρ is the density of the system and σ denotes the size of the 1st solvation shell.

[IV] Please note that $\Phi(t) = \frac{F(k=0,t)}{S(k=0)}$

6.3 Behaviour of the correlation function $F(k,t)$

Figure 6.3 (a) shows the behaviour of the correlation function $F(k,t)$ for high temperatures above the melting point. In this temperature region $F(k,t)$ decays like a single exponential function in time, $e^{-t/\tau}$, for $k > 2\pi/\sigma$. This k-value corresponds to the position of the first peak of the static structure factor, as shown in figure 6.2. In contrast to this scenario, the situation in supercooled liquids is more complex and the characteristic decay pattern shows a multistep behaviour, schematically sketched in figure 6.3 (b). The initial relaxation step ascribes to the so-called 'fast β-relaxation', the second one to the structural α-relaxation. Three different regions can be distinguished. Region I displays free and collisional events at short times, involving local particle motions. Region II ascribes to the fast β-relaxation. In this intermediate time regime, particles appear trapped in the transient cage formed by its neighbours (so-called cage-effect, cf. figure 2.12).[14] The decays IIa and IIb can be fitted by $f + At^{-a}$ and $f - Bt^{b}$, respectively. The exponents a and b correspond to the von Schweidler (ν^{-b}) and the critical law (ν^{a}), are temperature independent and directly connected by the exponent parameter $\lambda = \frac{\Gamma^2(1-a)}{\Gamma(1-2a)} = \frac{\Gamma^2(1+b)}{\Gamma(1+2b)}$ (cf. chapter 2.4.5).

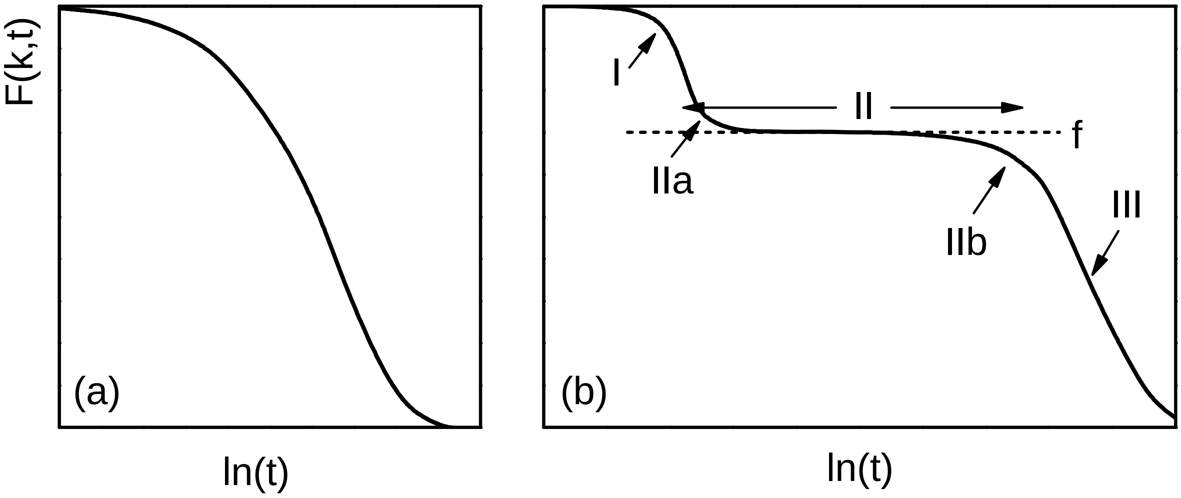

Figure 6.3: (a) In a normal liquid $F(k,t)$ exhibits an exponential decay $e^{-t/\tau}$. The decay of a supercooled liquid, showing various temporal regimes is displayed in (b). Details are described in the text. Taken from Ref. 282.

Region III corresponds to the α-relaxation regime and for instance may be fitted to a stretched exponential law, $F(k,t) \sim e^{-(t/\tau)^{\beta}}$. For more details see, e.g., Refs. 14, 168 and 282.

7 Bibliography

1. P. Lunkenheimer, *Dielectric spectroscopy of glassy dynamics* (Shaker Verlag, Aachen, 1999).
2. C.A. Angell, Science **267**, 1924 (1995).
3. P. Lunkenheimer, U. Schneider, R. Brand and A. Loidl, Contemp. Phys. **41**, 15 (2000).
4. P.G. Debenedetti and F.H. Stillinger, Nature **410**, 259 (2001).
5. P.W. Anderson, Science **267**, 1615 (1995).
6. S. Sastry, Nature **409**, 164 (2001).
7. S.A. Kivelson and G. Tarjus, Nat. Mater. **7**, 831 (2008).
8. R. Brand, P. Lunkenheimer and A. Loidl, J. Chem. Phys. **116**, 10386 (2002).
9. G. Adam and J.H. Gibbs, J. Chem. Phys. **43**, 139 (1965).
10. M.H. Cohen and D. Turnbull, J. Chem. Phys. **31**, 1164 (1959).
11. U. Bengtzelius, W. Götze and A. Sjölander, J. Phys. C **17**, 5915 (1984).
12. E. Leutheusser, Phys. Rev. A **29**, 2765 (1984).
13. W. Götze, Z. Phys. B: Condens. Matter **60**, 195 (1985).
14. W. Götze and L. Sjögren, Rep. Prog. Phys. **55**, 241 (1992).
15. J.C. Dyre, Rev. Mod. Phys. **78**, 953 (2006).
16. J.C. Dyre, J. Phys.: Condens. Matter **19**, 205105 (2007).
17. to be published in: P. Lunkenheimer, M. Köhler, S. Kastner and A. Loidl, in: *Structural Glasses and Supercooled Liquids: Theory, Experiment, and Applications.* edited by P.G. Wolynes and V. Lubchenko (John Wiley and Sons, Inc., New York, 2010).
18. C.J. Böttcher and P. Bordewijk, *Theory of Polarisation, Vol. II, Dielectrics in time-dependent fields* (Elsevier, Amsterdam, 1973).
19. P. Debye, *Polar molecules, Chemical catalog* (reprinted by Dover, 1929).
20. P. Debye, Phys. Z. **3**, 97 (1912).
21. R. Brand, *Breitbandige dielektrische Spektroskopie zur Untersuchung der Glasdynamik plastischer Kristalle* (Pro BUSINESS, Berlin, 2001).

22. P. Lunkenheimer and A. Loidl, Chem. Phys. **284**, 205 (2002).

23. A. Kudlik, S. Benkhof, T. Blochowicz, C. Tschirwitz and E.A. Rössler, J. Mol. Struct. **479**, 201 (1999).

24. P. Lunkenheimer, R. Wehn and A. Loidl, J. Non-Cryst. Solids **352**, 4941 (2006).

25. R. Wehn, P. Lunkenheimer and A. Loidl, J. Non-Cryst. Solids **353**, 3862 (2007).

26. G. Williams, D.C. Watts, S.B. Dev and A.M. North, Trans. Faraday Soc. **67**, 1323 (1971).

27. F.H. Stillinger, Science **267**, 1935 (1995).

28. G.P. Johari and M. Goldstein, J. Chem. Phys. **53**, 2372 (1970).

29. G.P. Johari, Ann. N.Y. Acad. Sci. **279**, 117 (1976).

30. G.P. Johari and M. Goldstein, J. Chem. Phys. **55**, 4245 (1971).

31. H. Wagner and R. Richert, J. Chem. Phys. **110**, 11660 (1999).

32. K.L. Ngai, J. Chem. Phys. **109**, 6982 (1998).

33. K.L. Ngai, Phys. Rev. E **57**, 7346 (1998).

34. P. Lunkenheimer, R. Wehn, T. Riegger and A. Loidl, J. Non-Cryst. Solids **307-310**, 336 (2002).

35. P. Lunkenheimer and A. Loidl, in: *Broadband Dielectric Spectroscopy.* edited by A. Schönhals and F. Kremer (Springer Verlag Berlin, 2002).

36. S. Havriliak and S. Negami, J. Polym. Sci., Part C **14**, 99 (1966).

37. K.S. Cole and R.H. Cole, J. Chem. Phys. **9**, 341 (1941).

38. D.W. Davidson and R.H. Cole, J. Chem. Phys. **18**, 1417 (1950).

39. D.W. Davidson and R.H. Cole, J. Chem. Phys. **19**, 1484 (1951).

40. R. Kohlrausch, Ann. Phys. **167**, 179 (1854).

41. G. Williams and D.C. Watts, Trans. Faraday Soc. **66**, 80 (1970).

42. A. Kudlik, C. Tschirwitz, S. Benkhof, T. Blochowicz and E.A. Rössler, Europhys. Lett. **40**, 649 (1997).

43. A. Döß, M. Paluch, H. Sillescu and G. Hinze, Phys. Rev. Lett. **88**, 95701 (2002).

44. U. Schneider, P. Lunkenheimer, R. Brand and A. Loidl, Phys. Rev. Lett. **84**, 5560 (2000).

45. J. Mattsson, R. Bergman, P. Jacobsson and L. Börjesson, Phys. Rev. Lett. **90**, 75702 (2003).

46. T. Blochowicz and E.A. Rössler, Phys. Rev. Lett. **92**, 225701 (2004).

47. S. Hensel-Bielowka, S. Pawlus, C.M. Roland, J. Ziolo and M. Paluch, Phys. Rev. E **69**, 50501 (2004).

48. K.L. Ngai, P. Lunkenheimer, C. León, U. Schneider, R. Brand and A. Loidl, J. Chem. Phys. **115**, 1405 (2001).

49. S. Hensel-Bielowka and M. Paluch, Phys. Rev. Lett. **89**, 25704 (2002).

50. P. Lunkenheimer, L.C. Pardo, M. Köhler and A. Loidl, Phys. Rev. E **77**, 31506 (2008).

51. P. Lunkenheimer, A. Pimenov, M. Dressel, Y.G. Goncharov, R. Böhmer and A. Loidl, Phys. Rev. Lett. **77**, 318 (1996).

52. P. Lunkenheimer, A. Pimenov and A. Loidl, Phys. Rev. Lett. **78**, 2995 (1997).

53. U. Schneider, P. Lunkenheimer, R. Brand and A. Loidl, J. Non-Cryst. Solids **235-237**, 173 (1998).

54. U. Schneider, P. Lunkenheimer, R. Brand and A. Loidl, Phys. Rev. E **59**, 6924 (1999).

55. K.L. Ngai, J. Phys.: Condens. Matter **15**, S1107 (2003).

56. R.H. Cole and E. Tombari, J. Non-Cryst. Solids **131-133**, 969 (1991).

57. K.L. Ngai, U. Strom and O. Kanert, Phys. Chem. Glasses **33**, 109 (1992).

58. D.L. Sidebottom, P.F. Green and R.K. Brow, J. Non-Cryst. Solids **203**, 300 (1996).

59. V.K. Malinovsky and A.P. Sokolov, Solid State Commun. **57**, 757 (1986).

60. P. Lunkenheimer and A. Loidl, J. Non-Cryst. Solids **352**, 4551 (2006).

61. J. Wuttke, J. Hernandez, G. Li, G. Coddens, H.Z. Cummins, F. Fujara, W. Petry and H. Sillescu, Phys. Rev. Lett. **72**, 3052 (1994).

62. P. Lunkenheimer and A. Loidl, cond-mat/0210067 (2002).

63. V.G. Karpov, M.I. Klinger and F.N. Ignatiev, Zh. Eksp. Teor. Fiz. **84**, 760 (1983).

64. V.G. Karpov, M.I. Klinger and F.N. Ignatiev, Sov. Phys. JETP **57**, 439 (1983).

65. U. Buchenau, V.L. Gurevich, D.A. Parshin, M.A. Ramos, H.R. Schober and Y.M. Galperin, Phys. Rev. B **46**, 2798 (1992).

66. S.R. Elliott, Europhys. Lett. **19**, 201 (1992).

67. V.K. Malinovsky, V.N. Novikov and A.P. Sokolov, J. Non-Cryst. Solids **90**, 485 (1987).

68. W. Schirmacher, G. Diezemann and C. Ganter, Phys. Rev. Lett. **81**, 136 (1998).

69. W. Götze and M.R. Mayr, Phys. Rev. E **61**, 587 (2000).

70. S.N. Taraskin, Phys. Rev. Lett. **86**, 1255 (2001).

71. C. Masciovecchio, A. Mermet, G. Ruocco and F. Sette, Phys. Rev. Lett. **85**, 1266 (2000).

72. O. Pilla, A. Cunsolo, A. Fontana, C. Masciovecchio, G. Monaco, M. Montagna, G. Ruocco, T. Scopigno and F. Sette, Phys. Rev. Lett. **85**, 2136 (2000).

73. U. Buchenau, H.M. Zhou, N. Nucker, K.S. Gilroy and W.A. Phillips, Phys. Rev. Lett. **60**, 1318 (1988).

74. E. Rat, M. Foret, E. Courtens, R. Vacher and M. Arai, Phys. Rev. Lett. **83**, 1355 (1999).

75. B. Hehlen, E. Courtens, R. Vacher, A. Yamanaka, M. Kataoka and K. Inoue, Phys. Rev. Lett. **84**, 5355 (2000).

76. A. Matic, D. Engberg, C. Masciovecchio and L. Börjesson, Phys. Rev. Lett. **86**, 3803 (2001).

77. M. Foret, E. Courtens, R. Vacher and J.B. Suck, Phys. Rev. Lett. **77**, 3831 (1996).

78. A.I. Chumakov, I. Sergueev, U. van Bürck, W. Schirmacher, T. Asthalter, R. Rüffer, O. Leupold and W. Petry, Phys. Rev. Lett. **92**, 245508 (2004).

79. W.T. Laughlin and D.R. Uhlmann, J. Phys. Chem. **76**, 2317 (1972).

80. C.A. Angell and W. Sichina, Ann. N.Y. Acad. Sci. **279**, 53 (1976).

81. M. Paluch, C.M. Roland, S. Pawlus, J. Ziolo and K.L. Ngai, Phys. Rev. Lett. **91**, 115701 (2003).

82. J.C. Dyre and N.B. Olsen, Phys. Rev. Lett. **91**, 155703 (2003).

83. D.J. Plazek and K.L. Ngai, Macromolecules **24**, 1222 (1991).

84. R. Böhmer and C.A. Angell, Phys. Rev. B **45**, 10091 (1992).

85. H. Vogel, Phys. Z. **22**, 645 (1921).

86. G. Tamman and W. Hesse, Z. Anorg. Allg. Chem **156**, 245 (1926).

87. K. L. Ngai, G. B. Wright, Eds., *Relaxations in Complex Systems* (National Technical Information Service, Springfield, 1985).

88. F. Stickel, E.W. Fischer and R. Richert, J. Chem. Phys. **102**, 6251 (1995).

89. F. Stickel, E.W. Fischer and R. Richert, J. Chem. Phys. **104**, 2043 (1996).

90. J.C. Phillips, Rep. Prog. Phys. **59**, 1133 (1996).

91. M.D. Ediger, C.A. Angell and S.R. Nagel, J. Phys. Chem. **100**, 13200 (1996).

92. M.D. Ediger, Annu. Rev. Phys. Chem. **51**, 99 (2000).

93. H. Sillescu, J. Non-Cryst. Solids **243**, 81 (1999).

94. R. Richert, J. Non-Cryst. Solids **172**, 209 (1994).

95. S.-H. Chong and W. Kob, Physical Review Letters **102**, 25702 (2009).

96. F.H. Stillinger and J.A. Hodgdon, Phys. Rev. E **50**, 2064 (1994).

97. J. Jäckle, Rep. Prog. Phys. **49**, 171 (1986).

98. A. Kudlik, C. Tschirwitz, T. Blochowicz, S. Benkhof and E.A. Rössler, J. Non-Cryst. Solids **235**, 406 (1998).

99. M. Vogel and E.A. Rössler, J. Chem. Phys. **114**, 5802 (2001).

100. M. Vogel and E.A. Rössler, J. Phys. Chem. **104**, 4285 (2000).

101. M. Vogel and E.A. Rössler, J. Chem. Phys. **115**, 10883 (2001).

102. J.S. Harmon, M.D. Demetriou, W.L. Johnson and K. Samwer, Phys. Rev. Lett. **99**, 135502 (2007).

103. C. Gainaru, O. Lips, A. Troshagina, R. Kahlau, A. Brodin, F. Fujara and E.A. Rössler, J. Chem. Phys. **128**, 174505 (2008).

104. K. Grzybowska, A. A.Grzybowski, J. Ziolo and M. Paluch, J. Chem. Phys. **125**, 44904 (2006).

105. N.B. Olsen, Phys. Rev. E **62**, 4435 (2000).

106. T. Christensen and N.B. Olsen, J. Non-Cryst. Solids **235**, 296 (1998).

107. K.S. Gilroy and W.A. Phillips, Philos. Mag. B **43**, 735 (1981).

108. A.Q. Tool, J. Am. Ceram. Soc. **29**, 240 (1946).

109. K.L. Ngai, Comments Solid State Phys. **9**, 127 (1979).

110. K.L. Ngai, in: *Disorder Effects on Relaxational Processes.* edited by R. Richert and A. Blumen (Springer, Berlin, 1994).

111. K.L. Ngai and R.W. Rendell, in: *Supercooled liquids.* edited by J.T. Fourkas *et al.* (American Chemical Soc., Washington, DC, 1997) *ACS Symposium Series*.

112. H.Z. Cummins, G. Li, Y.H. Hwang, G.Q. Shen, J. Hernandez and N.J. Tao, Z. Phys. B: Condens. Matter **103**, 501 (1997).

113. P. Lunkenheimer, A. Pimenov, M. Dressel, B. Gorshunov, U. Schneider, B. Schiener and A. Loidl, in: *Supercooled liquids.* edited by J.T. Fourkas *et al.* (American Chemical Soc., Washington, DC, 1997) *ACS Symposium Series*.

114. L. Boehm, D.L. Smith and C.A. Angell, J. Mol. Liq. **36**, 153 (1987).

115. C.A. Angell, L. Boehm, M. Oguni and D.L. Smith, J. Mol. Liq. **56**, 275 (1993).

116. J. Wong and C.A. Angell, *Glass: Structure by Spectroscopy* (M. Dekker, New York, 1976).

117. S.R. Elliott, Solid State Ionics **70**, 27 (1994).

118. C. Cramer, K. Funke and T. Saatkamp, Philos. Mag. B **71**, 701 (1995).

119. K.L. Ngai, H. Jain and O. Kanert, J. Non-Cryst. Solids **222**, 383 (1997).

120. M. Le Stanguennec and S.R. Elliott, Solid State Ionics **73**, 199 (1994).

121. L.C. Pardo, P. Lunkenheimer and A. Loidl, J. Chem. Phys. **124 (**2006).

122. J. Colmenero, A. Arbe and A. Alegria, Phys. Rev. Lett. **71**, 2603 (1993).

123. F. Alvarez, A. Hoffman, A. Alegria and J. Colmenero, J. Chem. Phys. **105**, 432 (1996).

124. A. Arbe, D. Richter, J. Colmenero and B. Farago, Phys. Rev. E **54**, 3853 (1996).

125. W. Götze, *Complex dynamics of glass-forming liquids, A mode-coupling theory* (Oxford Univ. Press, Oxford, 2009).

126. W. Götze and M. Sperl, Phys. Rev. Lett. **93**, 105701 (2004).

127. M. Sperl, Phys. Rev. E **74**, 11503 (2006).

128. H. Cang, V.N. Novikov and M.D. Fayer, Phys. Rev. Lett. **90**, 197401 (2003).

129. H. Cang, V.N. Novikov and M.D. Fayer, J. Chem. Phys. **118**, 2800 (2003).

130. W. Götze and A. Latz, J. Phys.: Condens. Matter **1**, 4169 (1989).

131. L.C. Pardo, P. Lunkenheimer and A. Loidl, Phys. Rev. E **76**, 030502(R) (2007).

132. C. Liu and C.A. Angell, J. Chem. Phys. **93**, 7378 (1990).

133. R. Schilling, in: *Disorder Effects on Relaxational Processes.* edited by R. Richert and A. Blumen (Springer, Berlin, 1994).

134. H.Z. Cummins, J. Phys.: Condens. Matter **11**, A95 (1999).

135. W. Götze, Physik Journal **5**, 35 (2006).

136. T. Franosch, M. Fuchs, W. Götze and M.R. Mayr, Phys. Rev. E **55**, 7153 (1997).

137. R. Schilling and T. Scheidsteger, Phys. Rev. E **56**, 2932 (1997).

138. W. Götze, Z. Phys. B: Condens. Matter **56**, 139 (1984).

139. L. Sjögren, Phys. Rev. A **33**, 1254 (1986).

140. W. Götze, J. Phys.: Condens. Matter **2**, 8485 (1990).

141. J. Wuttke, M. Ohl, M. Goldammer, S. Roth, U. Schneider, P. Lunkenheimer, R. Kahn, B. Ruffle, R. Lechner and M.A. Berg, Phys. Rev. E **61**, 2730 (2000).

142. J.C. Dyre, P. Maass, B. Roling and D.L. Sidebottom, Rep. Prog. Phys. **72**, 46501 (2009).

143. A.K. Jonscher, Nature **267**, 673 (1977).

144. A.K. Jonscher, *Dielectric relaxation in solids* (Chelsea Dielectrics Pr., London, 1983).

145. A.R. Long, Adv. Phys **31**, 553 (1982).

146. S.R. Elliott, Adv. Phys **36**, 135 (1987).

147. P. Lunkenheimer and A. Loidl, Phys. Rev. Lett. **91**, 207601 (2003).

148. U. Schneider, P. Lunkenheimer, A. Pimenov, R. Brand and A. Loidl, Ferroelectrics **249**, 89 (2001).

149. R. Böhmer, M. Maglione, P. Lunkenheimer and A. Loidl, J. Appl. Phys. **65**, 901 (1989).

150. A.M. Nicolson and G.F. Ross, IEEE Trans. Instrum. Meas. **IM19**, 377 (1970).

151. A.A. Volkov, Y.G. Goncharov, G.V. Kozlov, S.P. Lebedev and A.M. Prokhorov, Infrared Phys. **25**, 369 (1985).

152. A.A. Volkov, G.V. Kozlov, S.P. Lebedev and A.M. Prokhorov, Infrared Phys. **29**, 747 (1889).

153. G.V. Kozlov and A.A. Volkov, in: *Millimeter and Submillimeter Wave Spectroscopy of Solids.* edited by G. Grüner *et al.* (Springer, Berlin, 1998), vol. 74 *Topics in Applied Physics*.

154. R. Wehn, *Dielektrische Spektroskopie zur Untersuchung der Glasdynamik im Nichtgleichgewicht, Dissertation, Universität Augsburg* (2008).

155. Novocontrol, *Alpha High Resolution Dielectric Analyzer User's Manual* (1998).

156. Hewlett-Packard, *Operation Manual HP 4284A Precision LCR-Meter* (1991).

157. Hewlett-Packard, *Operation Manual HP 4191A RF Impedance Analyzer* (1990).

158. Hewlett-Packard, *HP 4291A RF Impedance/Material Analyzer Service Manual* (1995).

159. Agilent Technologies, *Agilent E4991A RF Impedance/Material Analyzer Operation Manual* (2002).

160. Hewlett-Packard, *Operation and Programming Manual HP 8510C Network Analyzer* (1991).

161. Agilent Technologies, *Agilent AN1287-1 Understanding the Fundamental Principles of Vector Network Analysis* (1997).

162. E. Pehl, *Mikrowellentechnik Band 1: Wellenleitung und Leitungsbausteine* (Dr. Alfred Hüthig Verlag, Heidelberg, 1988).

163. G. Käs and P. Pauli, *Mikrowellentechnik: Grundlagen, Anwendung und Meßtechnik* (Franzis-Verlag GmbH, München, 1991).

164. S.F. Adam, *Microwave theory and applications* (Adam Microwave Consulting, inc., Los Altos, 1992).

165. Y.G. Goncharov, *private communication* .

166. M. Born and E. Wolf, *Principles of Optics* (Pergamon Press, Oxford, 1980).

167. F. Mayer, *Breitbandige Spektroskopie an Manganaten mit Perowskit-Struktur* (Shaker Verlag, Aachen, 2003).

168. G.L. Squires, *Introduction to the theory of thermal neutron scattering* (Dover Publications, Mineola N.Y., 1996).

169. M. Bée, *Quasielastic neutron scattering, Principles and applications in solid state chemistry, biology and materials science* (Hilger, Bristol, 1988).

170. T. Unruh, E. Neuhaus and W. Petry, Nucl. Instrum. Methods Phys. Res., Sect. A **585**, 201 (2008).

171. S. Thraenert, E.M. Hassan and R. Krause-Rehberg, Nucl. Instrum. Methods Phys. Res., Sect. B **248**, 336 (2006).

172. J. Bartos, in: *Encyclopedia of analytical chemistry.* edited by R.A. Meyers (John Wiley & Sons Ltd; Wiley, Chichester, 2000).

173. *inspired by a talk from R. Krause-Rehberg, see: http://positron.physik.uni-halle.de/* .

174. T. Brückel, in: *Laboratory Course Neutron Scattering.* edited by T. Brückel *et al.* (Forschungszentrum Jülich, Jülich, 2007) *Materie und Material.*

175. A. Ioffe, in: *Laboratory Course Neutron Scattering.* edited by T. Brückel *et al.* (Forschungszentrum Jülich, Jülich, 2007) *Materie und Material.*

176. J. Bartos, O. Sausa, J. Kristiak, T. Blochowicz and E.A. Rössler, J. Phys. Condens. Matter **13**, 11473 (2001).

177. R. Krause-Rehberg and H.S. Leipner, *Positron annihilation in semiconductors* (Springer, Berlin, 2003).

178. P. Lunkenheimer, R. Wehn, U. Schneider and A. Loidl, Phys. Rev. Lett. **95**, 55702 (2005).

179. M. Köhler, P. Lunkenheimer, Y.G. Goncharov, R. Wehn and A. Loidl, J. Non-Cryst. Solids **356**, 529 (2010).

180. K.L. Ngai, K. Grzybowska, A. Grzybowski, E. Kaminska, K. Kaminski, M. Paluch and S. Capaccioli, J. Non-Cryst. Solids **354**, 5085 (2008).

181. W. Götze and L. Sjögren, Z. Phys. B: Condens. Matter **65**, 415 (1987).

182. A. Brodin and E.A. Rössler, J. Chem. Phys. **125**, 114502 (2006).

183. T. Fujima, H. Frusawa and K. Ito, Phys. Rev. E **66**, 31503 (2002).

184. R. Nozaki, H. Zenitani, A. Minoguchi and K. Kitai, J. Non-Cryst. Solids **307**, 349 (2002).

185. G. Williams, Adv. Polym. Sci. **33**, 60 (1979).

186. G. Diezemann, U. Mohanty and I. Oppenheim, Phys. Rev. E **59**, 2067 (1999).

187. M.J. Lebon, C. Dreyfus, Y. Guissani, R.M. Pick and H.Z. Cummins, Z. Phys. B: Condens. Matter **103**, 433 (1997).

188. A. Brodin and E.A. Rössler, Eur. Phys. J. B **44**, 3 (2005).

189. P. Lunkenheimer, A. Pimenov, M. Dressel, B. Gorshunov, U. Schneider, B. Schiener, R. Böhmer and A. Loidl, in: *Structure and Dynamics of Glasses and Glass Formers.* edited by C.A. Angell (Material Research Society, Pittsburgh, 1997), vol. 455.

190. W.M. Du, G. Li, H.Z. Cummins, M. Fuchs, J. Toulouse and L.A. Knauss, Phys. Rev. E **49**, 2192 (1994).

191. U. Buchenau, M. Ohl and A. Wischnewski, J. Chem. Phys. **124**, 94505 (2006).

192. J. Swenson, I. Koper and M.T. Telling, J. Chem. Phys. **116**, 5073 (2002).

193. R. Bergman, L. Börjesson, L.M. Torell and A. Fontana, Phys. Rev. B **56**, 11619 (1997).

194. R. Bergman, C. Svanberg, D. Andersson, A. Brodin and L.M. Torell, J. Non-Cryst. Solids **235**, 225 (1998).

195. S. Kojima, H. Sato and A. Yosihara, J. Phys. Condens. Matter **9**, 10079 (1997).

196. A. Yoshihara, H. Sato and S. Kojima, Prog. Theor. Suppl. **126**, 423 (1997).

197. A. Yoshihara, H. Sato and S. Kojima, Jpn. J. Appl. Phys., Part 1 **35**, 2925 (1996).

198. M.S. Beevers, S.R. Elliot and G. Williams, Polymer **21**, 13 (1980).

199. E.H. Bentefour, J. Chem. Phys. **120**, 3726 (2004).

200. K. Grzybowska, A. Grzybowski, S. Pawlus, S. Hensel-Bielowka and M. Paluch, J. Chem. Phys. **123**, 204506 (2005).

201. K. Grzybowska, S. Pawlus, M. Mierzwa, M. Paluch and K.L. Ngai, J. Chem. Phys. **125**, 144507 (2006).

202. C.M. Roland, R. Casalini and M. Paluch, Chem. Phys. Lett. **367**, 259 (2003).

203. S. Pawlus, S. Hensel-Bielowka, K. Grzybowska, J. Ziolo and M. Paluch, Phys. Rev. B **71**, 174107 (2005).

204. S. Pawlus, S. Hensel-Bielowka, M. Paluch, R. Casalini and C.M. Roland, Phys. Rev. B **72**, 64201 (2005).

205. K. Grzybowska, A. Grzybowski, J. Ziolo, S.J. Rzoska and M. Paluch, J. Phys. Condens. Matter **19**, 376105 (2007).

206. R. Casalini and C.M. Roland, Phys. Rev. B **69**, 94202 (2004).

207. C. León, K.L. Ngai and C.M. Roland, J. Chem. Phys **110**, 11585 (1999).

208. R. Casalini and C.M. Roland, Phys. Rev. Lett. **91**, 15702 (2003).

209. M. Köhler, *Relaxation phenomena in glassforming liquids, Master Thesis, Universität Augsburg* (Universität Augsburg, 2007).

210. C.A. Angell, Solid State Ionics **9-10**, 3 (1983).

211. C.A. Angell, J. Phys. Chem. Solids **49**, 863 (1988).

212. K. Grzybowska, A. Grzybowski and M. Paluch, J. Chem. Phys. **128**, 134904 (2008).

213. Y. Ryabov, A. Gutina, V. Arkhipov and Y. Feldman, J. Phys. Chem. B **105**, 1845 (2001).

214. Y.E. Ryabov, Y. Hayashi, A. Gutina and Y. Feldman, Phys. Rev. B **67**, 132202 (2003).

215. A. Schönhals, F. Kremer, A. Hofmann, E.W. Fischer and E. Schlosser, Phys. Rev. Lett. **70**, 3459 (1993).

216. S. Adichtchev, T. Blochowicz, C. Tschirwitz, V.N. Novikov and E.A. Rössler, Phys. Rev. E **68**, 11504 (2003).

217. S. Wiebel and J. Wuttke, New J. Phys. **4**, 56.1 (2002).

218. W. Götze and T. Voigtmann, Phys. Rev. E **61**, 4133 (2000).

219. P. Lunkenheimer and A. Loidl, Advances in Sol. Stat. Phys. **41**, 405 (2001).

220. U. Strom, J.R. Hendrickson, R.J. Wagner and P.C. Taylor, Solid State Commun. **15**, 1871 (1974).

221. U. Strom and P.C. Taylor, Phys. Rev. B **16**, 5512 (1977).

222. C.A. Angell, J. Wong and W.F. Edgell, J. Chem. Phys. **51**, 4519 (1969).

223. W. Bagdad and R. Stolen, J. Phys. Chem. Solids **29**, 2001 (1968).

224. L.A. Leites, Chem. Rev. **92**, 279 (1992).

225. J.L. Sauvajol, M. Bée and J.P. Amoureux, Mol. Phys. **46**, 811 (1982).

226. P. Lunkenheimer and A. Loidl, J. Chem. Phys. **104**, 4324 (1996).

227. E.F. Westrum and S. Henriquez, Mol. Cryst. Liq. Cryst. **32**, 31 (1976).

228. P. Beckmann and A.J. Leffler, J. Chem. Phys. **72**, 4600 (1980).

229. P. Lunkenheimer and A. Loidl, Adv. Solid State Phys., 405 (2001).

230. N.G. McCrum, B.E. Read and G. Williams, *Anelastic and dielectric effects in polymeric solids* (John Wiley & Sons Ltd, New York, 1991).

231. W.H. Stockmayer and J.J. Burke, Macromolecules **2**, 647 (1969).

232. G.A. Schwartz, R. Bergman and J. Swenson, J. Chem. Phys. **120**, 5736 (2004).

233. C. Gainaru and R. Böhmer, Macromolecules **42**, 7616 (2007).

234. N.O. Birge, Phys. Rev. B **34**, 1631 (1986).

235. Y.H. Jeong, S.R. Nagel and S. Bhattacharya, Phys. Rev. A **34**, 602 (1986).

236. K.L. Ngai, Phys. Rev. B **41**, 754 (1990).

237. L. Wu, P.K. Dixon, S.R. Nagel and B.D. Williams, J. Non-Cryst. Solids **131**, 32 (1991).

238. G. Wahnström and L.J. Lewis, Prog. Theor. Suppl. **126**, 261 (1997).

239. S. Kämmerer, W. Kob and R. Schilling, Phys. Rev. E **58**, 2131 (1998).

240. H.Z. Cummins, Phys. Rev. E **53**, 896 (1996).

241. H.Z. Cummins, G. Li, W. Du, Y.H. Hwang and G.Q. Shen, Prog. Theor. Suppl. **126**, 21 (1997).

242. S.W. Lovesey, *Theory of neutron scattering from condensed matter* (Clarendon Press, Oxford, 1984).

243. Y.C. Jean, P.E. Mallon and D.M. Schrader, *Principles and applications of positron & positronium chemistry* (World Scientific, River Edge, NJ, 2003).

244. J. Bartos, L. Andreozzi, M. Faetti, O. Sausa, D. Racko and J. Kristiak, J. Non-Cryst. Solids **352**, 4785 (2006).

245. J. Bartos, O. Sausa, D. Racko, J. Kristiak and J.J. Fontanella, J. Non-Cryst. Solids **351**, 2599 (2005).

246. J. Bartos, V. Majernik, M. Iskrova, O. Sausa, J. Kristiak, P. Lunkenheimer and A. Loidl, J. Non-Cryst. Solids **356**, 794 (2010).

247. C.A. Angell, in: *Relaxations in Complex Systems.* edited by K.L. Ngai and G.B. Wright (National Technical Information Service, Springfield, 1985).

248. R. Böhmer, K.L. Ngai, C.A. Angell and D.J. Plazek, J. Chem. Phys. **99**, 4201 (1993).

249. M. Köhler, P. Lunkenheimer and A. Loidl, Eur. Phys. J. E **27**, 115 (2008).

250. M. Köhler, *Ionenleitfähigkeit in unterkühlten Flüssigkeiten, Bachelor Thesis, Universität Augsburg* (2005).

251. A. Hofmann, F. Kremer, E.W. Fischer and A. Schönhals, in: *Disorder Effects on Relaxational Processes.* edited by R. Richert and A. Blumen (Springer, Berlin, 1994).

252. N. Menon, K.P. O'Brien, P.K. Dixon, L. Wu, S.R. Nagel, B.D. Williams and J.P. Carini, J. Non-Cryst. Solids **141**, 61 (1992).

253. P.K. Dixon, Phys. Rev. B **42**, 8179 (1990).

254. A. Kudlik, S. Benkhof, R. Lenk and E.A. Rössler, Europhys. Lett. **32**, 511 (1995).

255. R. Casalini, K.L. Ngai and C.M. Roland, J. Chem. Phys. **112**, 5181 (2000).

256. P. Lunkenheimer, U. Schneider, R. Brand and A. Loidl, in: *Slow dynamics in complex systems.* edited by M. Tokuyama and I. Oppenheim (AIP, New York, 1999).

257. J.R. Macdonald, *Impedance Spectroscopy* (John Wiley and Sons, NewYork, Chichester, Brisbane, Toronto, 1987).

258. P.B. Macedo, C.T. Moynihan and R. Bose, Phys. Chem. Glasses **13**, 171 (1972).

259. B. Roling, A. Happe, K. Funke and M.D. Ingram, Phys. Rev. Lett. **78**, 2160 (1997).

260. I.M. Hodge, K.L. Ngai and C.T. Moynihan, J. Non-Cryst. Solids **351**, 104 (2005).

261. J.R. Macdonald, J. Phys. Chem. B **111**, 7064 (2007).

262. S.R. Elliott, J. Non-Cryst. Solids **170**, 97 (1994).

263. D.L. Sidebottom, B. Roling and K. Funke, Phys. Rev. B **63**, 24301 (2000).

264. F.S. Howell, C.T. Moynihan and P.B. Macedo, Bull. Chem. Soc. Jpn. **57**, 652 (1984).

265. G.P. Johari and K. Pathmanathan, Phys. Chem. Glasses **29**, 219 (1988).

266. R. Richert and H. Wagner, J. Phys. Chem. **99**, 10948 (1995).

267. F.E. Harris and C.T. O´Konski, J. Phys. Chem. **61**, 310 (1957).

268. K. Nörtemann, J. Hilland and U. Kaatze, J. Phys. Chem. A **101**, 6864 (1997).

269. R. Gulich, M. Köhler, P. Lunkenheimer and A. Loidl, Radiat. Environ. Biophys. **48**, 107 (2009).

270. U. Schneider, *Breitbandige dielektrische Studien der Dynamik struktureller Glasbildner* (Libri Books on Demand, Norderstedt, 2000).

271. N.B. Olsen, Phys. Rev. Lett. **86**, 1271 (2001).

272. F.J. Bartoli, J.N. Birch, N.H. Toan and G.E. McDuffie, J. Chem. Phys. **49**, 1916 (1968).

273. A.A. Pronin, M.V. Kondrin, A.G. Lyapin, V.V. Brazhkin, A.A. Volkov, P. Lunkenheimer and A. Loidl, arXiv:0911.3496.

274. F. Alvarez, A. Alegria and J. Colmenero, Phys. Rev. B **44**, 7306 (1991).

275. R. Böhmer and C.A. Angell, in: *Disorder Effects on Relaxational Processes.* edited by R. Richert and A. Blumen (Springer, Berlin, 1994).

276. T. Scopigno, G. Ruocco, F. Sette and G. Monaco, Science **849**, 849 (2003).

277. V.N. Novikov and A.P. Sokolov, Nature **431**, 961 (2004).

278. L.M. Martinez and C.A. Angell, Nature **410**, 663 (2001).

279. T. Bauer, M. Köhler, P. Lunkenheimer, A. Loidl and C.A. Angell, to be published.

280. F. Mizuno, J.P. Belieres, N. Kuwata, A. Pradel, M. Ribes and C.A. Angell, J. Non-Cryst. Solids **352**, 5147 (2006).

281. A.P. Sokolov, E.A. Rössler, A. Kisliuk and D. Quitmann, Phys. Rev. Lett. **71**, 2062 (1993).

282. D.R. Reichman and P. Charbonneau, J. Stat. Mech: Theory Exp. **2005**, P05013 (2005).

283. W. Kob, in: *Supercooled liquids.* edited by J.T. Fourkas *et al.* (American Chemical Soc., Washington, DC, 1997) *ACS Symposium Series*.

Dank an…

Hiermit möchte ich mich bei allen bedanken, die - direkt oder indirekt - zum Gelingen dieser Arbeit beigetragen und mich unterstützt haben. Mein besonderer Dank gilt…

Prof. Dr. Alois Loidl für die Möglichkeit zur Mitarbeit an seinem Lehrstuhl und die Freiräume die ein kreatives Arbeiten ermöglichten, die angenehme Arbeitsatmosphäre und die oftmals unkonventionellen Gedankenanstöße.

Priv. Doz. Dr. Peter Lunkenheimer für seine äußerst engagierte, kompetente und geduldige Betreuung; für die Einführung in die dielektrische Spektroskopie und für das kritische Auge bei Layoutangelegenheiten. Ohne seine stete Hilfsbereitschaft und die vielen fachlichen Diskussionen wäre diese Arbeit in der vorliegenden Form nicht möglich gewesen.

Prof. Dr. Armin Reller für die freundliche Übernahme des Zweitgutachtens.

Prof. Dr. Gert-Ludwig Ingold für seine sofortige Bereitschaft sich an der Prüfungskomission zu beteiligen und die meiner Meinung nach sowohl fachlich als auch didaktisch besten Vorlesungen.

Dr. Yurii Goncharov for all the things I have learned from him during numerous days in the lab and the pleasant time and conversations.

Dr. Franz Mayr für die Einführung in die Infrarotspektroskopie und seine Bemühungen Küvetten und Zubehör für die Flüssigkeitsmessungen zu optimieren.

Dipl. Phys. Thomas Bauer den ich während seiner Diplomarbeit mitbetreut habe und der immer mit Begeisterung bei der Sache war.

M. Sc. Stephan Krohns und **M.Sc. Florian Schrettle** für die gemeinsame Zeit während Studium und Promotion und für viele Gespräche über Gott und die Welt und die Bereitschaft diese Arbeit Korrektur zu lesen.

Dipl.-Ing. Dana Vieweg für die Hilfe bei der Probenpräparation und den DSC Messungen.

Dr. Joachim Wuttke für die zahlreichen und interessanten Diskussionen.

Dr. Luis Carlos Pardo für die ganzen Diskussionen und Gespräche.

Dipl. Phys. Sebastian Busch für die nette Gesellschaft in Rom, die interessanten Gespräche und die ganze Hilfe bei "FRIDA-Fragen".

Dr. Tobias Unruh für die Unterstützung bei den Neutronenstreuexperimenten.

Dr. Rudi Herrmann für die Unterstützung in chemischen Fragen.

Dr. Helena Svajdlenkova für die lustige Zeit im Labor und **Dr. Josef Bartos** für die lang anhaltende Zusammenarbeit.

M. Sc. Dieter Himsl für die Übernahme von einigen NMR Messungen.

allen Kolleginnen und Kollegen, Andreas, Anna, Anny, Axel, Birgitta, Christian, Elisabeth, Hans-Albrecht, Joachim, Mammoun, Michael, Martin, Nikola, Norbert, Robert F. und Robert W., Rudi, Sebastian, Thomas, Torsten, Vladimir, Wolfgang, Xin, den Nanochor und den Mitarbeitern der Feinmechanischen Werkstatt, für das angenehme Arbeitsklima, die vielen Gespräche und die donnerstäglichen Kuchenrunden.

allen Freunden und Mitsportlern, Anna, Anne, Bobby, Christian, Clemens, Florian L. und Florian S., Peter, Regina, Sepp, Shirin, Simon, Tina und alle die ich sonst noch so vergessen habe, für unzählige Stunden an der Wand, am Fels und im Eis sowie für alle anderen unzähligen Unternehmungen, den Erfahrungsaustausch und die Freundschaft.

Meinen Eltern **Manfred und Ursula Köhler**, die immer hinter mir standen und mich unterstützten.

Simon, für die langjährige Freundschaft und daß doch alles anders kommt als man denkt.

Curriculum vitae

Melanie Köhler
*21.06.1980 in Bobingen

1986-1990	Grundschule Kissing
1990-1999	Rudolf-Diesel Gymnasium, Augsburg
Juni 1999	Abitur
1999-2002	Berufsausbildung und Beschäftigung bei der Bayerischen Bereitschaftspolizei
2002-2007	Studium der Materialwissenschaften an der Universität Augsburg
September 2005	Bachelor of Science
September 2007	Master of Science
seit Oktober 2007	Wissenschaftliche Angestellte am Institut für Physik, Lehrstuhl für Experimentalphysik V, Universität Augsburg